Neutrino Nonstandard Interactions and Atmospheric Neutrinos

Shinya Fukasawa

Department of Physics,
Graduate School of Science and Engineering,
Tokyo Metropolitan University

A dissertation submitted to
Graduate School of Science and Engineering,
Tokyo Metropolitan University

2017

Acknowledgements

Firstly, I would like to thank my supervisor Professor Osamu Yasuda for the continuous support of my Ph.D study. I am grateful to Assistant Professor Noriaki Kitazawa and Project Assistant Professor Monojit Ghosh for their fruitful advices. I would like to thank my parents for their supporting my life and my wife for her spiritual support.

Abstract

We study the sensitivity of the atmospheric neutrino measurements at the future Hyper-Kamiokande (HK) facility to the flavor-dependent neutrino nonstandard interactions (NSI) in propagation. After we review the standard model with three massive neutrinos, the various experiments of neutrino oscillations, and the constraint on NSI, we study the potential of the atmospheric neutrino experiment at HK to search for NSI. NSI in neutrino propagation is described by the dimensionless parameter $\epsilon_{\alpha\beta}$ ($\alpha, \beta = e, \mu, \tau$) in the flavor basis. Under the phenomenologically reasonable assumptions that all the NSI parameters related to μ-sector $\epsilon_{\mu\alpha}$ ($\alpha = e, \mu\tau$) vanish and that $\epsilon_{\tau\tau}$ and $\epsilon_{e\tau}$ satisfy a parabolic relation $\epsilon_{\tau\tau} = |\epsilon_{e\tau}|^2/(1 + \epsilon_{ee})$, we show that the energy rate analysis of Hyper-Kamiokande (HK) data for 4438 days gives the constraint $|\tan\beta| \lesssim 0.3$ at 2.5 σ, and that the energy spectrum analysis gives stronger constraints on NSI. It has been suggested that a tension between the mass-squared differences obtained from the solar neutrino and KamLAND experiments can be solved by introducing NSI. We investigate how much the atmospheric neutrino experiment at HK can exclude NSI for the best-fit values obtained by such analysis on the solar neutrino and KamLAND experiments. The HK energy spectrum analysis for 4438 days data can exclude the best-fit value of NSI from the global analysis at 5.0 σ (1.4 σ) in the case of normal (inverted) hierarchy. We also study the octant degeneracy in the atmospheric neutrino experiments in the standard three flavor mixing scenario.

Contents

Chapter 1

Introduction

Neutrino oscillations are phenomena which are caused by massive neutrinos and are well established by solar, atmospheric, reactor and accelerator neutrino experiments. They are therefore the phenomena beyond the Standard Model (SM) which explains most of the particle physics experimental results. In the standard three flavor neutrino oscillation framework which is embedded in the SM with massive neutrinos, there are three mixing angles θ_{12}, θ_{13}, θ_{23} and two mass-squared differences Δm^2_{21}, Δm^2_{31}. Their approximate values are determined as $(\Delta m^2_{21}, \sin^2 2\theta_{12}) \simeq (7.5 \times 10^{-5}\mathrm{eV}^2, 0.86)$, $(|\Delta m^2_{31}|, \sin^2 2\theta_{23}) \simeq (2.5 \times 10^{-3}\mathrm{eV}^2, 1.0)$, $\sin^2 2\theta_{13} \simeq 0.09$. Atmospheric, solar and reactor neutrino experiments are relevant to the determination of $(|\Delta m^2_{31}|, \theta_{23})$, $(\Delta m^2_{21}, \theta_{12})$ and θ_{13}, respectively. However we do not know the value of Dirac CP phase δ, the sign of Δm^2_{31} (the mass hierarchy) and the octant of θ_{23} (the sign of $\pi/4 - \theta_{23}$). To measure the undetermined neutrino oscillation parameters mentioned above, neutrino oscillation experiments with high statistics are planned and we may be able to observe a deviation from the standard three flavor neutrino oscillation framework by using these high precision measurements. Therefore it is important to study new physics in the future neutrino experiments.

In this thesis we regard flavor-dependent neutrino NonStandard Interactions (NSI) as new physics candidate and investigate the potential sensitivity of future experiment Hyper-Kamiokande (HK) to NSI. There are two types of NSI. One is a neutral current nonstandard interaction [1, 2, 3] and the other is a charged current nonstandard interaction [4]. The neutral current NSI affects the neutrino propagation through the matter effect and hence experiments with a long baseline such as atmospheric neutrino and Long BaseLine (LBL) experiments are expected to have the sensitivity to the neutral current NSI. On the other hand, the charged current NSI causes zero distance effects in neutrino oscillation. Constraints on the charged

current NSI is very strong compared with those on the neutral current NSI and hence the effects of charged current NSI are negligible. We concentrate on the effects of neutral current NSI in neutrino propagation

There are mainly two motivations of investigating the neutral current NSI. Firstly, constraints on NSI from current neutrino oscillation experiments are weak. Strength of NSI coupling comparable with SM interaction is allowed. There are rooms for improvement of NSI constraint by future experiment HK. Secondly, NSI have a potential to resolve a tension between the mass-squared difference deduced from the solar neutrino observations and the one from the KamLAND experiment. The mass-squared difference Δm^2_{21} ($= 4.7 \times 10^{-5}\mathrm{eV}^2$) extracted from the solar neutrino data is 2σ smaller than that from the KamLAND data Δm^2_{21} ($= 7.5 \times 10^{-5}\mathrm{eV}^2$). The difference may be explained by assuming the NSI effects. Such a hint for NSI gives us a strong motivation to study NSI in propagation in details.

In the standard three flavor case, NSI are parameterized as $\epsilon_{\alpha\beta}$ ($\alpha, \beta = e, \mu, \tau$) where α and β stand for neutrino flavors. Physical meaning of $\epsilon_{\alpha\beta}$ is the coupling constant of $\nu_\alpha + f \to \nu_\beta + f$ reaction where f stands for fermions in matter. The oscillation probabilities in atmospheric and accelerator neutrinos can be expressed in terms of $\epsilon_{\alpha\beta}$. However nonzero NSI indicated by the tension between the solar neutrino and KamLAND experiment are parameterized as $\epsilon_{D,N}$ which is linear combination of $\epsilon_{\alpha\beta}$. This is because the oscillations in the solar neutrino and KamLAND experiments involve mostly two mass eigenstates, and the analysis of these experiments uses the Hamiltonian in which the basis is reduced to the two mass eigenstates to a good approximation. Therefore a non-trivial mapping between $\epsilon_{\alpha\beta}$ and $\epsilon_{D,N}$ is required to investigate the potential sensitivity of future atmospheric neutrino experiment such as HK to NSI.

Firstly, we discuss the sensitivity of HK to NSI parameterized as $\epsilon_{\alpha\beta}$ assuming $\epsilon_{\alpha\mu} = 0$ and $\epsilon_{\tau\tau} = |\epsilon_{e\tau}|^2/(1+\epsilon_{ee})$ which are suggested by the high energy atmospheric neutrino data. Secondly, we discuss the possibility to observe NSI parameterized as $\epsilon_{D,N}$ indicated by the tension between the solar neutrino and KamLAND experiment by using HK data without the assumptions mentioned above.

This thesis is organized as follows. In Chapter 2, we describe the foundation of SM and formulate neutrino oscillations. A brief discussion on so called parameter degeneracy is also given. In Chapter 3, we give a brief review of the major experiments. In Chapter 4, we describe the neutrino oscillations with NSI and constraints on NSI. In Chapter 5, we investigate the sensitivity of HK to NSI. In Chapter 6, we describe the sign(Δm^2_{31}) degeneracy in HK. In Chapter 7, we draw our conclusions.

Chapter 2

The Standard Model with Massive Neutrinos and Neutrino Oscillations

In this chapter we review the foundation of neutrino oscillations. First, we overview the Standard Model (SM) of particle physics which describes the gauge interactions of elementary particles. SM contains the strong and electroweak interactions and they are orthogonal to each other. This fact allows us to concentrate on the electroweak sector as far as neutrino oscillations are concerned. Second, we discuss the neutrino masses. Neutrino oscillations are caused by their masses but SM treats neutrinos as massless particles. We need to modify SM so that the theory contains neutrino masses. Finally, we formulate neutrino oscillations in SM with massive neutrinos framework and discuss so called *parameter degeneracy* which arise when one tries to determine the neutrino oscillation parameters by experiments.

2.1 The Standard Model

The Standard Model (SM) is the most success particle physics theory [5, 6] based on the gauge theory consist of the strong interactions $\mathrm{SU(3)_C}$ and the electroweak interactions $\mathrm{SU(2)_L} \times \mathrm{U(1)_Y}$. All the fields in SM belong to the representation of the gauge groups and hence are transformed by the gauge groups. The left-handed and right-handed fermions are introduced as the doublet of $\mathrm{SU(2)_L}$ and the singlet

of $\mathrm{SU(2)_L}$, respectively:

$$Q_{iL} = \begin{pmatrix} u_{iL} \\ d_{iL} \end{pmatrix}, \;\; L_{\alpha L} = \begin{pmatrix} \nu_{\alpha L} \\ \ell_{\alpha L} \end{pmatrix}, \;\; u_{iR}, \;\; d_{iR}, \;\; \ell_{\alpha R}. \tag{2.1}$$

u_{iL} and d_{iL} $(i = 1, 2, 3)$ stand for the left-handed up-type and down-type quarks, respectively, and α and i stand for the generation indices. $\ell_{\alpha L}$ and $\nu_{\alpha L}$ $(\alpha = e, \mu, \tau)$ stand for the left-handed charged leptons and neutrinos, respectively. u_{iR}, d_{iR} and $\ell_{\alpha R}$ stand for the right-handed up-type quarks, down-type quarks and charged leptons, respectively. Notice that SM dose not contain the right-handed neutrinos and thus neutrinos are treated as massless particles in the SM. This is because that the right-handed neutrinos have not been observed. The left-handed and right-handed fermions can be obtained by the projection operators $P_{L,R}$:

$$P_L = \frac{1 - \gamma^5}{2}, \qquad P_R = \frac{1 + \gamma^5}{2}, \tag{2.2}$$

$$\gamma^5 = \gamma_5 = i\gamma^0\gamma^1\gamma^2\gamma^3. \tag{2.3}$$

γ^μ stands for Dirac matrix.

For simplicity, we concentrate on the first generation of quarks and leptons (we omit the generation indices α and i for the moment). The generalization of the properties presented here to the case of three generation is straightforward. The electroweak Lagrangian is determined by renormalizability and the gauge symmetry:

$$\begin{aligned} \mathcal{L} &= i\overline{L_L}\not{D}L_L + i\overline{Q_L}\not{D}Q_L + \sum_{f=u,d,e} i\overline{f_R}\not{D}f_R - \frac{1}{4}\sum_{a=1}^{3} A^a_{\mu\nu}A^{\mu\nu}_a - \frac{1}{4}B_{\mu\nu}B^{\mu\nu} \\ &+ (D_\mu\Phi)^\dagger(D^\mu\Phi) - \mu^2\Phi^\dagger\Phi - \lambda(\Phi^\dagger\Phi)^2 \\ &- y^e(\overline{L_L}\Phi e_R + \overline{e_R}\Phi^\dagger L_L) - y^d(\overline{Q_L}\Phi d_R + \overline{d_R}\Phi^\dagger Q_L) - y^u(\overline{Q_L}\tilde{\Phi}u_R + \overline{u_R}\tilde{\Phi}^\dagger Q_L). \end{aligned} \tag{2.4}$$

Here $\not{D} = \gamma_\mu D^\mu$ is the Feynman slash notation, D_μ stands for the covariant derivative

$$D_\mu = \partial_\mu + ig\sum_{a=1}^{3} A^a_\mu I_a + ig'B_\mu\frac{Y}{2}, \tag{2.5}$$

g and g' in Eq. (2.5) are the gauge coupling constants for $\mathrm{SU(2)_L}$ and $\mathrm{U(1)_Y}$, respectively, I_a $(a = 1, 2, 3)$ is the generator of $\mathrm{SU(2)_L}$, Y is the hypercharge operator and

A^a_μ and B_μ are the gauge fields for $\mathrm{SU(2)_L}$ and $\mathrm{U(1)_Y}$, respectively. $A^a_{\mu\nu}$ and $B_{\mu\nu}$ in Eq. (2.4) are the field strength for $\mathrm{SU(2)_L}$ and $\mathrm{U(1)_Y}$, respectively:

$$A^a_{\mu\nu} = \partial_\mu A^a_\nu - \partial_\nu A^a_\mu - g\sum_{b,c=1}^{3} f_{abc} A^b_\mu A^c_\nu, \tag{2.6}$$

$$B_{\mu\nu} = \partial_\mu B_\nu - \partial_\nu B_\mu. \tag{2.7}$$

Φ is the Higgs fields and $\tilde{\Phi}$ is given by

$$\tilde{\Phi} = i\tau_2 \Phi^*.$$

Here τ_2 is Pauli matrix. μ^2 and λ in the second line of Eq. (2.4) are the parameters for the Higgs potential and $y^{e,u,d}$ in the third line of Eq. (2.4) is the Yukawa coupling constant. We cannot find the mass terms in Eq. (2.4) because they are forbidden by the symmetry groups. However we obtain them via the Brout-Englert-Higgs mechanism discussed later.

First of all, we consider only the the lepton sector. The interaction term between the leptons and the gauge bosons is

$$\mathcal{L}_{I,L} = -\frac{1}{2}\begin{pmatrix} \overline{\nu_{eL}} & \overline{e_L} \end{pmatrix}\begin{pmatrix} g\not{A}_3 - g'\not{B} & g(\not{A}_1 - i\not{A}_2) \\ g(\not{A}_1 + i\not{A}_2) & -g\not{A}_3 - g'\not{B} \end{pmatrix}\begin{pmatrix} \nu_{eL} \\ e_L \end{pmatrix} + g'\overline{e_R}\not{B}e_R. \tag{2.8}$$

This can be divided into the charged-current (CC) interaction and the neutral-current (NC) interaction

$$\mathcal{L}^{CC}_{I,L} = -\frac{g}{2}\{\overline{\nu_{eL}}(\not{A}_1 - i\not{A}_2)e_L + \overline{e_L}(\not{A}_1 + i\not{A}_2)\nu_{eL}\}, \tag{2.9}$$

$$\mathcal{L}^{NC}_{I,L} = -\frac{1}{2}\{\overline{\nu_{eL}}(g\not{A}_3 - g'\not{B})\nu_{eL} + \overline{e_L}(g\not{A}_3 + g'\not{B})e_L - 2g'\overline{e_R}\not{B}e_R\}. \tag{2.10}$$

We define the gauge fields

$$W^\mu \equiv \frac{A^\mu_1 - iA^\mu_2}{\sqrt{2}}, \tag{2.11}$$

and then the CC interaction can be written as

$$\begin{aligned} \mathcal{L}^{CC}_{I,L} &= -\frac{g}{\sqrt{2}}\overline{\nu_e}\not{W}\frac{1-\gamma^5}{2}e + h.c. \\ &= -\frac{g}{2\sqrt{2}} j^\mu_{W,L} W_\mu + h.c.\ . \end{aligned} \tag{2.12}$$

Here $j^{\mu}_{W,L}$ is the leptonic charged current

$$j^{\mu}_{W,L} = \overline{\nu_e}\gamma^{\mu}(1-\gamma^5)e = 2\overline{\nu_{eL}}\gamma^{\mu}e_L. \tag{2.13}$$

We rotate the gauge fields A^{μ}_3 and B^{μ} in order to obtain the electromagnetic interaction from Eq. (2.10)

$$A^{\mu} = \sin\theta_W A^{\mu}_3 + \cos\theta_W B^{\mu}, \tag{2.14}$$

$$Z^{\mu} = \cos\theta_W A^{\mu}_3 - \sin\theta_W B^{\mu}. \tag{2.15}$$

The angle θ_W is called the Weinberg angle or weak mixing angle and chosen so that the electrically neutral neutrinos do not couple to the electromagnetic fields. This can be done by interpreting the gauge field A^{μ} as the electromagnetic field and choosing the Weinberg angle as follows

$$\tan\theta_W = \frac{g'}{g}. \tag{2.16}$$

Then we rewrite $\mathcal{L}^{NC}_{I,L}$ in terms of A^{μ} and Z^{μ}

$$\begin{aligned}\mathcal{L}^{NC}_{I,L} &= -\frac{g}{2\cos\theta_W}\{\overline{\nu_{eL}}\not{Z}\nu_{eL} - (1-2\sin^2\theta_W)\overline{e_L}\not{Z}e_L + 2\sin^2\theta_W\overline{e_R}\not{Z}e_R\} \\ &+ g\sin\theta_W\bar{e}\not{A}e. \end{aligned}\tag{2.17}$$

The first line in Eq. (2.17) is the weak NC interaction and can be written as follows

$$\mathcal{L}^{Z}_{I,L} = -\frac{g}{2\cos\theta_W}j^{\mu}_{Z,L}Z_{\mu}, \tag{2.18}$$

$$\begin{aligned} j^{\mu}_{Z,L} &= 2g^{\nu}_L\overline{\nu_{eL}}\gamma^{\mu}\nu_{eL} + 2g^{l}_L\overline{e_L}\gamma^{\mu}e_L + 2g^{l}_R\overline{e_R}\gamma^{\mu}e_R \\ &= \overline{\nu_e}\gamma^{\mu}(g^{\nu}_V - g^{\nu}_A\gamma^5)\nu_e + \bar{e}\gamma^{l}(g^{\nu}_V - g^{l}_A\gamma^5)e. \end{aligned}\tag{2.19}$$

Here we define, respectively, the coefficient for the fermions $g^f_{L,R}$ and $g^f_{V,A}$ as follows

$$g^f_L = I^f_3 - q^f\sin^2\theta_W, \tag{2.20}$$

$$g^f_R = -q^f\sin^2\theta_W, \tag{2.21}$$

$$g^f_V = g^f_L + g^f_R = I^f_3 - 2\sin^2\theta_W, \tag{2.22}$$

$$g^f_A = g^f_L - g^f_R = I^f_3. \tag{2.23}$$

I^f_3 stands for the eigenvalue of the third generator of $\mathrm{SU(2)_L}$ and q^f stands for the electric charge of fermions. The second line in Eq. (2.17) corresponds to the electromagnetic interaction and we find that the electric charge is given by

$$g\sin\theta_W = e. \tag{2.24}$$

The interactions of the quark sector can be obtained in the same way as the lepton sector. The CC interaction is

$$\mathcal{L}_{I,Q}^{CC} = -\frac{g}{2\sqrt{2}} j_{W,Q}^{\mu} W_{\mu} + h.c. \ , \tag{2.25}$$

$$j_{W,Q}^{\mu} = \overline{u}\gamma^{\mu}(1-\gamma^5)d = 2\overline{u_L}\gamma^{\mu}d_L, \tag{2.26}$$

and NC interaction is

$$\mathcal{L}_{I,Q}^{NC} = \mathcal{L}_{I,Q}^{Z} + \mathcal{L}_{I,Q}^{\gamma}, \tag{2.27}$$

$$\mathcal{L}_{I,Q}^{\gamma} = -e j_{\gamma,Q}^{\mu} A_{\mu}, \tag{2.28}$$

$$\mathcal{L}_{I,Q}^{Z} = -\frac{g}{2\cos\theta_W} j_{Z,Q}^{\mu} Z_{\mu}, \tag{2.29}$$

$$j_{\gamma,Q}^{\mu} = \frac{2}{3}\overline{u}\gamma^{\mu}u - \frac{1}{3}\overline{d}\gamma^{\mu}d, \tag{2.30}$$

$$\begin{aligned} j_{Z,Q}^{\mu} &= 2g_L^U \overline{u_L}\gamma^{\mu}u_L + 2g_R^U \overline{u_R}\gamma^{\mu}u_R + 2g_L^D \overline{d_L}\gamma^{\mu}d_L + 2g_R^D \overline{d_R}\gamma^{\mu}d_R \\ &= \overline{u}\gamma^{\mu}(g_V^U - g_A^U\gamma^5)u + \overline{d}\gamma^{\mu}(g_V^D - g_A^D\gamma^5)d. \end{aligned} \tag{2.31}$$

Let us discuss the Brout-Englert-Higgs mechanism by which all the masses of field are generated. The Higgs fields are expressed as the $\mathrm{SU(2)_L}$ doublet

$$\Phi(x) = \begin{pmatrix} \phi^+(x) \\ \phi^0(x) \end{pmatrix}. \tag{2.32}$$

Here $\phi^+(x)$ is a charged complex scalar field and $\phi^0(x)$ is a neutral complex scalar field. These fields are not the physical Higgs fields because the physical Higgs field is observed by excitations from the vacuum. We can choose the electric neutral vacuum by getting the most out of the gauge symmetry and the specific choice of the vacuum causes spontaneous symmetry breaking. We have the vacuum expectation value (VEV) of the Higgs doublet

$$\langle\Phi\rangle = \frac{1}{\sqrt{2}} \begin{pmatrix} 0 \\ v \end{pmatrix}, \tag{2.33}$$

where

$$v = \sqrt{-\frac{\mu^2}{\lambda}}, \tag{2.34}$$

and we can write the Higgs doublet as

$$\Phi(x) = \frac{1}{\sqrt{2}} \begin{pmatrix} 0 \\ v + H(x) \end{pmatrix}, \tag{2.35}$$

where $H(x)$ is the physical Higgs field. Substituting the above expression for the Higgs field for the Higgs part of SM Lagrangian, we have

$$\begin{aligned} \mathcal{L}_{Higss} &= (D_\mu \Phi)^\dagger (D^\mu \Phi) - \mu^2 \Phi^\dagger \Phi - \lambda (\Phi^\dagger \Phi)^2 \\ &= \frac{1}{2}(\partial H)^2 - \lambda v^2 H^2 - \lambda v H^3 - \frac{\lambda}{4} H^4 + \frac{g^2 v^2}{4} W_\mu^\dagger W^\mu + \frac{g^2 v^2}{8 \cos^2 \theta_W} Z_\mu Z^\mu \\ &+ \frac{g^2 v}{2} W_\mu^\dagger W^\mu H + \frac{g^2 v}{4 \cos^2 \theta_W} Z_\mu H \\ &+ \frac{g^2}{4} W_\mu^\dagger W^\mu H^2 + \frac{g^2}{8 \cos^2 \theta_W} Z_\mu H^2. \end{aligned} \tag{2.36}$$

We find that the gauge bosons get their masses

$$m_W = \frac{gv}{2}, \qquad m_Z = \frac{gv}{2 \cos \theta_W}. \tag{2.37}$$

The fermion masses are also obtain by the Brout-Englert-Higgs mechanism. We discuss the neutrino masses in the next section. Obtaining the masses, neutrinos are mixed with each others.

2.2 Neutrino Masses and the Lepton Mixing Matrix

In preceding section we discussed the gauge interactions and the Brout-Englert-Higgs mechanism. In this section we discuss the simplest neutrino mass generation mechanism. We consider three generation framework from now on. We add three right-handed neutrinos which are singlets under the gauge symmetry $\mathrm{SU(3)_C} \times \mathrm{SU(2)_L} \times \mathrm{U(1)_Y}$ to SM so that the masses of neutrinos are generated. In the case of SM with the three right-handed neutrinos, the Yukawa Lagrangian for the leptons is extended as follows

$$\mathcal{L}_{H,L} = - \sum_{\alpha,\beta=e,\mu,\tau} Y'^{\ell}_{\alpha\beta} \overline{L'_{\alpha L}} \Phi \ell'_{\beta R} - \sum_{\alpha,\beta=e,\mu,\tau} Y'^{\nu}_{\alpha\beta} \overline{L'_{\alpha L}} \tilde{\Phi} \nu'_{\beta R} + h.c. \ , \tag{2.38}$$

where $L'_{\alpha L}$ are the lepton doublets

$$L'_{\alpha L} = \begin{pmatrix} \nu_{\alpha L} \\ \ell'_{\alpha L} \end{pmatrix}, \qquad (\alpha = e, \mu, \tau) \tag{2.39}$$

$\ell'_{\alpha L}$ ($\ell'_{\alpha R}$) are the left-handed (the right-handed) charged leptons

$$\ell'_{eL} = e'_L, \quad \ell'_{\mu L} = \mu'_L, \quad \ell'_{\tau L} = \tau'_L, \tag{2.40}$$

$$\ell'_{eR} = e'_R, \quad \ell'_{\mu R} = \mu'_R, \quad \ell'_{\tau R} = \tau'_R, \tag{2.41}$$

and $\nu'_{\alpha L}$ ($\nu'_{\alpha R}$) are the left-handed (the right-handed) neutrinos. $Y'^{\ell}_{\alpha\beta}$ and $Y'^{\nu}_{\alpha\beta}$ are complex matrixes of Yukawa couplings for the charged leptons and neutrinos, respectively. The matrixes $Y'^{\ell}_{\alpha\beta}$ and $Y'^{\nu}_{\alpha\beta}$ are not diagonal but can be diagonalized by the redefinition of the fields. Substituting Eq. (2.35) to Eq. (2.38), we have

$$\mathcal{L}_{H,L} = -\frac{v+H}{\sqrt{2}}[\overline{\boldsymbol{\ell}'_L} Y'^{\ell} \boldsymbol{\ell}'_R + \overline{\boldsymbol{\nu}'_L} Y'^{\nu} \boldsymbol{\nu}'_R] + h.c. \ , \tag{2.42}$$

where we define the fields arrays

$$\boldsymbol{\ell}'_{L,R} \equiv \begin{pmatrix} \ell'_{eL,R} \\ \ell'_{\mu L,R} \\ \ell'_{\tau L,R} \end{pmatrix}, \qquad \boldsymbol{\nu}'_{L,R} \equiv \begin{pmatrix} \nu'_{eL,R} \\ \nu'_{\mu L,R} \\ \nu'_{\tau L,R} \end{pmatrix}. \tag{2.43}$$

The Yukawa couplings matrixes $Y'^{\ell}_{\alpha\beta}$ and $Y'^{\nu}_{\alpha\beta}$ can be diagonalized by bi-unitary transformations

$$V_L^{\ell\dagger} Y'^{\ell} V_R^{\ell} = Y^{\ell} = \mathrm{diag}(y_e^{\ell}, y_\mu^{\ell}, y_\tau^{\ell}), \tag{2.44}$$

$$V_L^{\nu\dagger} Y'^{\nu} V_R^{\nu} = Y^{\nu} = \mathrm{diag}(y_1^{\nu}, y_2^{\nu}, y_3^{\nu}), \tag{2.45}$$

and then we have the masses of the charged leptons and neutrinos

$$m_\alpha = \frac{y_\alpha^{\ell} v}{\sqrt{2}} \qquad (\alpha = e, \mu, \tau), \tag{2.46}$$

$$m_k = \frac{y_k^{\nu} v}{\sqrt{2}} \qquad (k = 1, 2, 3). \tag{2.47}$$

The fields arrays are affected by the diagonalization

$$\boldsymbol{n}_L = V_L^{\nu\dagger} \boldsymbol{\nu}'_L \equiv \begin{pmatrix} \nu_{1L} \\ \nu_{2L} \\ \nu_{3L} \end{pmatrix}, \qquad \boldsymbol{\ell}_L = V_L^{\ell\dagger} \boldsymbol{\ell}'_L \equiv \begin{pmatrix} e_L \\ \mu_L \\ \tau_L \end{pmatrix}. \tag{2.48}$$

In the basis of Eq. (2.48), the leptonic CC interaction $j^{\mu}_{W,L}$ can be written as

$$j^{\mu}_{W,L} = 2\overline{\boldsymbol{\nu}'_L}\gamma^{\mu}\boldsymbol{\ell}'_L = 2\overline{\boldsymbol{n}_L}U^{\dagger}\gamma^{\mu}\boldsymbol{\ell}_L, \tag{2.49}$$

where a matrix U is defined as

$$U \equiv V^{\ell\dagger}_L V^{\nu}_L. \tag{2.50}$$

The matrix U is called the *Pontecorvo-Maki-Nakagawa-Sakata (PMNS) matrix* or *Maki-Nakagawa-Sakata (MNS) matrix*. The neutrino oscillations are parameterized by the MNS matrix and squared-mass differences of the neutrinos.

2.3 Neutrino Masses

We discuss what is called the see-saw mechanism that naturally generates small neutrino masses. In the see-saw mechanism, neutrinos are treated as Majorana particles and hence they can have Majorana mass term.

2.3.1 Majorana Mass Term

It is known that massive neutrinos obey the Dirac eq.

$$(i\partial\!\!\!/ - m)\psi = 0, \tag{2.51}$$

where ψ stands for neutrino field and m stands for the neutrino mass. This equation is equivalent to

$$i\partial\!\!\!/\psi_L = m\psi_R, \tag{2.52}$$

$$i\partial\!\!\!/\psi_R = m\psi_L, \tag{2.53}$$

where ψ_R and ψ_L stand for right-handed and left-handed component of ψ. If we require the relationship between ψ_R and ψ_L

$$\psi_R = \xi\mathcal{C}\overline{\psi_L}^T, \tag{2.54}$$

we get the Majorana eq.[1]

$$i\partial\!\!\!/\psi_L = m\mathcal{C}\overline{\psi_L}^T. \tag{2.55}$$

Where ξ is a phase factor and $\mathcal{C}$ is a charge conjugate operator. $\mathcal{C}$ has the following nature:

$$\mathcal{C}\gamma^T_{\mu}\mathcal{C}^{-1} = -\gamma_{\mu}, \tag{2.56}$$

[1]We redefine the fields as $\psi_L \to \xi^{1/2}\psi_L$ so that the phase factor is eliminated.

$$\mathcal{C}^\dagger = \mathcal{C}^{-1}, \tag{2.57}$$

$$\mathcal{C}^T = -\mathcal{C}. \tag{2.58}$$

If we suppose Eq. (2.54), the fermion field can be written as

$$\psi = \mathcal{C}\overline{\psi}^T. \tag{2.59}$$

This relationship implies that the particle and anti-particle are identical. From that statement, Eq. (2.54) can be realized only if the particles have no electric charge. The fields which satisfy Eq. (2.54) are called Majorana fields.

We consider one generation for simplicity. If neutrinos are Majorana fermions, they can have Majorana mass term

$$\mathcal{L}^M_{mass} = -\frac{1}{2} m \overline{\nu^C_L} \nu_L, \tag{2.60}$$

where

$$\nu^C_L = \mathcal{C}\overline{\nu_L}^T. \tag{2.61}$$

It is worth noting that Majorana mass term is not invariant under $U(1)$ transformation and hence that violates lepton number.

In general neutrinos can have not only Dirac mass term but also Majorana mass term. The most general neutrino mass term can be written as

$$\mathcal{L}^{D+M}_{mass} = \mathcal{L}^D_{mass} + \mathcal{L}^L_{mass} + \mathcal{L}^R_{mass} \tag{2.62}$$

$$\mathcal{L}^D_{mass} = -m_D \overline{\nu_R} \nu_L + h.c. \tag{2.63}$$

$$\mathcal{L}^L_{mass} = \frac{1}{2} m_L \nu^T_L \mathcal{C}^\dagger \nu_L + h.c. \tag{2.64}$$

$$\mathcal{L}^R_{mass} = \frac{1}{2} m_R \nu^T_R \mathcal{C}^\dagger \nu_R + h.c. \tag{2.65}$$

Defining the fields array

$$N_L = \begin{pmatrix} \nu_L \\ \nu^C_R \end{pmatrix} = \begin{pmatrix} \nu_L \\ \mathcal{C}\overline{\nu_R}^T \end{pmatrix}, \tag{2.66}$$

we can write neutrino mass term as

$$\mathcal{L}^{D+M}_{mass} = \frac{1}{2} N^T_L \mathcal{C}^\dagger M N_L + h.c. \tag{2.67}$$

$$M = \begin{pmatrix} m_L & m_D \\ m_D & m_R \end{pmatrix}. \tag{2.68}$$

The neutrino mass matrix (2.68) can be diagonalized by unitary transformation

$$U_L^T M U_L = \mathrm{diag}(m_1, m_2). \tag{2.69}$$

If we restrict m_D and $m_{R,L}$ to real, the eigenvalues of the neutrino mass matrix (2.68) are

$$m_1 = \rho_1^2 \frac{m_L + m_R - \sqrt{(m_L - m_R)^2 + 4m_D^2}}{2}, \tag{2.70}$$

$$m_2 = \rho_2^2 \frac{m_L + m_R + \sqrt{(m_L - m_R)^2 + 4m_D^2}}{2}, \tag{2.71}$$

where $\rho_{1,2}$ is a phase of the unitary matrix. In transformed basis neutrino fields array is turned into

$$n_L = U_L^{-1} N_L = \begin{pmatrix} \nu_{1L} \\ \nu_{2L} \end{pmatrix}, \tag{2.72}$$

and their mass term can be written as

$$\mathcal{L}_{mass}^{D+M} = \frac{1}{2} \sum_{k=1,2} m_k \nu_{kL}^T \mathcal{C}^\dagger \nu_{kL} + h.c. = -\frac{1}{2} \sum_{k=1,2} m_k \overline{\nu_k} \nu_k, \tag{2.73}$$

where

$$\nu_k = \nu_{kL} + \nu_{kL}^C = \nu_{kL} + \mathcal{C}\overline{\nu_{kL}}^T. \tag{2.74}$$

2.3.2 See-saw Mechanism

Let us consider a interesting case

$$m_D \ll m_R, \qquad m_L = 0. \tag{2.75}$$

From Eqs. (2.70) and (2.71), we obtain

$$m_1 \simeq -\rho_1^2 \frac{m_D^2}{m_R}, \qquad m_2 \simeq \rho_2^2 m_R. \tag{2.76}$$

Choosing the phase of the unitary matrix so that we eliminate the negative sign of m_1, we have

$$m_1 \simeq \frac{m_D^2}{m_R}, \qquad m_2 \simeq m_R. \tag{2.77}$$

Therefore the mass of ν_1 is very light and that of ν_1 is the same order of magnitude of m_R. This light neutrino mass generation mechanism without an unnatural assumption is called see-saw mechanism.

2.4 Neutrino Oscillation Formalism

In this section we formalize the neutrino oscillations in SM with the massive neutrinos framework. The MNS matrix introduced in the preceding section plays a central role in the neutrino oscillations. This section is organized as follows. In subsection 2.4.1 and 2.4.2, we discuss the neutrino oscillation when the neutrinos propagate in the vacuum and matter, respectively. In subsection 2.4.3, we discuss a problem called parameter degeneracy which prevents us from determining the oscillation parameters uniquely in the long baseline experiments.

2.4.1 Neutrino Oscillations in Vacuum

In this subsection, we derive the neutrino oscillation probability in the vacuum. The neutrino mass eigenstate $|\nu_j\rangle$ $(j = 1, 2, 3)$ and flavor eigenstate $|\nu_\alpha\rangle$ $(\alpha = e, \mu, \tau)$ are connected by the MNS matrix which is parameterized by three mixing angles $\theta_{12}, \theta_{13}, \theta_{23}$ and the Dirac CP phase δ[2]

$$|\nu_\alpha\rangle = \sum_{j=1}^{3} U^*_{\alpha j}|\nu_j\rangle, \tag{2.78}$$

where the MNS matrix U is

$$\begin{aligned} U &= \begin{pmatrix} 1 & 0 & 0 \\ 0 & c_{23} & s_{23} \\ 0 & -s_{23} & c_{23} \end{pmatrix} \begin{pmatrix} c_{13} & 0 & s_{13}e^{i\delta} \\ 0 & 1 & 0 \\ -s_{13}e^{-i\delta} & 0 & c_{13} \end{pmatrix} \begin{pmatrix} c_{12} & s_{12} & 0 \\ -s_{12} & c_{12} & 0 \\ 0 & 0 & 1 \end{pmatrix} \\ &= \begin{pmatrix} c_{12}c_{13} & s_{12}c_{13} & s_{13}e^{-i\delta} \\ -s_{12}c_{23} - c_{12}s_{23}s_{13}e^{i\delta} & c_{12}c_{23} - s_{12}s_{23}s_{13}e^{i\delta} & s_{23}c_{13} \\ s_{12}s_{23} - c_{12}c_{23}s_{13}e^{i\delta} & -c_{12}s_{23} - s_{12}c_{23}s_{13}e^{i\delta} & c_{23}c_{13} \end{pmatrix}, \end{aligned} \tag{2.79}$$

and

$$s_{ij} = \sin\theta_{ij}, \qquad c_{ij} = \cos\theta_{ij}. \tag{2.80}$$

The neutrino states are chosen to be orthonormal

$$\langle\nu_j|\nu_k\rangle = \delta_{jk}, \tag{2.81}$$

[2]Eq (2.78) can be obtained from the requirement that neutrino wave functions are related through $\nu_\alpha = \sum_{j=1}^{3} U_{\alpha\j}\nu_j$ where $\nu_\alpha(\alpha = e, \mu, \tau)$ and $\nu_j(j = 1, 2, 3)$ stand for the neutrino wave functions in the flavor and mass basis, respectively. The wave functions are defined as $\nu_\alpha \equiv \langle\nu_\alpha|\nu\rangle$ and $\nu_j \equiv \langle\nu_j|\nu\rangle$. Using the completeness relation $I = \sum_j |\nu_j\rangle\langle\nu_j|$, the neutrino wave function in the flavor basis can be expressed as $\nu_\alpha = \langle\nu_\alpha|\nu\rangle = \sum_j \langle\nu_\alpha|\nu_j\rangle\langle\nu_j|\nu\rangle = \sum_j U_{\alpha j}\nu_j = \sum_j U_{\alpha j}\langle\nu_j|\nu\rangle$ and we can get $U_{\alpha j} = \langle\nu_\alpha|\nu_j\rangle$. Using the expression of $U_{\alpha j}$, we can get $|\nu_\alpha\rangle = \sum_j |\nu_j\rangle\langle\nu_j|\nu_\alpha\rangle = \sum_j U^*_{\alpha j}|\nu_j\rangle$.

$$\langle \nu_\alpha | \nu_\beta \rangle = \delta_{\alpha\beta}. \tag{2.82}$$

The time evolution of the neutrino mass eigenstates is governed by the Dirac equation

$$i\frac{d}{dt}|\nu_j\rangle = E_j|\nu_j\rangle, \tag{2.83}$$

where $E_j = \sqrt{\mathbf{p}^2 + m_j^2}$ are eigenvalues of the neutrino mass eigenstates. Eq. (2.83) can be easily solved and then we have

$$|\nu_j(t)\rangle = e^{-iE_j t}|\nu_j(t=0)\rangle. \tag{2.84}$$

By definition, the neutrinos are created and detected as the flavor eigenstates and propagate as the mass eigenstates. The transition amplitude of $\nu_\alpha \to \nu_\beta$ is given by

$$\begin{aligned}
\mathcal{A}_{\alpha\to\beta}(t) &= \langle \nu_\beta | \nu_\alpha(t) \rangle \\
&= \langle \nu_\beta | \sum_{j=1}^{3} U_{\alpha j}^* |\nu_j(t)\rangle \\
&= \langle \nu_\beta | \sum_{j=1}^{3} U_{\alpha j}^* e^{-iE_j t} \sum_\gamma U_{\gamma j} |\nu_\gamma\rangle \\
&= \sum_j U_{\alpha j}^* U_{\beta j} e^{-iE_j t}.
\end{aligned} \tag{2.85}$$

Then we have the transition probability is given by

$$P_{\alpha\to\beta}(t) = |\mathcal{A}_{\alpha\to\beta}(t)|^2 = \sum_{j,k} U_{\alpha j}^* U_{\beta j} U_{\alpha k} U_{\beta k}^* e^{-i(E_j - E_k)t}. \tag{2.86}$$

The neutrinos can be treated as ultrarelativistic and hence the energy eigenvalues can be approximated by

$$E_j \simeq E + \frac{m_k^2}{2E}, \tag{2.87}$$

where $E = |\mathbf{p}|$. In this approximation, the energy difference in Eq. (2.86) can be written as

$$E_j - E_k \simeq \frac{\Delta m_{jk}^2}{2E}, \tag{2.88}$$

where Δm_{jk}^2 is the squared-mass difference

$$\Delta m_{jk}^2 \equiv m_j^2 - m_k^2. \tag{2.89}$$

Because the neutrino propagate at the speed of light, we can approximate the propagation time t as the flight length L which is the distance between the neutrino source and detector. Finally, we obtain the neutrino oscillation probability in the vacuum

$$P_{\alpha\to\beta}(L,E) = \sum_{j,k} U^*_{\alpha j} U_{\beta j} U_{\alpha k} U^*_{\beta k} \exp(-i\frac{\Delta m^2_{jk} L}{2E}). \tag{2.90}$$

Using unitarity of the MNS matrix, we can write the oscillation probability as

$$\begin{aligned} P_{\alpha\to\beta}(L,E) = \delta_{\alpha\beta} &- 4\sum_{j<k} \mathrm{Re}[U^*_{\alpha j} U_{\beta j} U_{\alpha k} U^*_{\beta k}] \sin^2\left(\frac{\Delta E_{jk} L}{2}\right) \\ &+ 2\sum_{j<k} \mathrm{Im}[U^*_{\alpha j} U_{\beta j} U_{\alpha k} U^*_{\beta k}] \sin\left(\Delta E_{jk} L\right), \end{aligned} \tag{2.91}$$

where $\Delta E_{jk} \equiv E_j - E_k$. In the case of the anti-neutrinos, changing $U_{\alpha j} \to U^*_{\alpha j}$ in Eq. (2.91) gives the oscillation probability.

2.4.2 Neutrino Oscillations in Matter

The neutrino cross section is very small and hence the neutrinos hardly interact with matter. However, L. Wolfenstein [1] found that the neutrinos which propagate in matter feel potentials caused by the coherent forward scattering of the neutrinos and matter. This potential changes the time evolution of the neutrinos. After the discovery of L. Wolfenstein, S.P. Mikheev and A.Yu. Smirnov [7] found that the transition probability is enhanced when the neutrinos propagate in matter. The effect of neutrino interactions with matter is called the MSW effect or the matter effect. The potential caused by the NC interactions dose not affect the neutrino oscillation probability because it is proportional to an identity matrix in the flavor basis, and it only affects the overall phase of the transition amplitude. Hence we investigate the matter effect caused by the CC interactions.

Charged leptons in ordinarily matter are only the electrons and hence only the electron neutrinos interact with matter through the CC interactions. The effective interaction Hamiltonian is given as

$$H^{\mathrm{CC}}_{\mathrm{eff}}(x) = \frac{G_F}{\sqrt{2}}[\overline{\nu_e}(x)\gamma_\mu(1-\gamma^5)\nu_e(x)][\overline{e}(x)\gamma^\mu(1-\gamma^5)e(x)]. \tag{2.92}$$

In the rest frame of matter, this Hamiltonian can be understood as

$$H^{\mathrm{CC}}_{\mathrm{eff}}(x) \to \sqrt{2} G_F N_e \overline{\nu_{eL}}(x)\gamma^0\nu_{eL}(x), \tag{2.93}$$

where G_F is the Fermi coupling constant and N_e is the number density of electrons in matter. Therefore the electron neutrinos feel the potential $A \equiv \sqrt{2} G_F N_e$ in matter. The Dirac equation in matter is as follows

$$i\frac{d}{dt}\begin{pmatrix}\nu_e\\ \nu_\mu\\ \nu_\tau\end{pmatrix} = \left(U\mathcal{E}U^\dagger + \mathcal{A}\right)\begin{pmatrix}\nu_e\\ \nu_\mu\\ \nu_\tau\end{pmatrix}, \tag{2.94}$$

where $\mathcal{E}$ stands for the neutrino energy

$$\mathcal{E} = \mathrm{diag}\left(E_1, E_2, E_3\right)$$

and $\mathcal{A}$ stands for the matter potential

$$\mathcal{A} = \mathrm{diag}\left(A, 0, 0\right).$$

Assuming constant density, Eq. (2.94) can be solved by diagonalizing the Hamiltonian in propagation. Then we have the following equation

$$i\frac{d}{dt}\begin{pmatrix}\nu_e\\ \nu_\mu\\ \nu_\tau\end{pmatrix} = \tilde{U}\tilde{\mathcal{E}}\tilde{U}^\dagger\begin{pmatrix}\nu_e\\ \nu_\mu\\ \nu_\tau\end{pmatrix}, \tag{2.95}$$

where $\tilde{\mathcal{E}}$ is a diagonal matrix whose components are the eigenvalues of the Hamiltonian in propagation and $\tilde{U}$ is a unitary matrix which diagonalizes the Hamiltonian in propagation

$$\tilde{\mathcal{E}} \equiv \tilde{U}^\dagger\left(U\mathcal{E}U^\dagger + \mathcal{A}\right)\tilde{U} = \mathrm{diag}(\tilde{E}_1, \tilde{E}_2, \tilde{E}_3). \tag{2.96}$$

Because Eq. (2.96) has the same form as that of vacuum oscillation, the oscillation probabilities in matter can be obtained by changing $U \to \tilde{U}$ and $E_j \to \tilde{E}_j$ in Eq. (2.91)

$$\begin{aligned} P_{\alpha\to\beta}(L,E) = \delta_{\alpha\beta} \quad &- \quad 4\sum_{j<k}\mathrm{Re}[\tilde{U}^*_{\alpha j}\tilde{U}_{\beta j}\tilde{U}_{\alpha k}\tilde{U}^*_{\beta k}]\sin^2\left(\frac{\Delta\tilde{E}_{jk}L}{2}\right) \\ &+ \quad 2\sum_{j<k}\mathrm{Im}[\tilde{U}^*_{\alpha j}\tilde{U}_{\beta j}\tilde{U}_{\alpha k}\tilde{U}^*_{\beta k}]\sin\left(\Delta\tilde{E}_{jk}L\right), \end{aligned} \tag{2.97}$$

where $\Delta\tilde{E}_{ij} \equiv \tilde{E}_i - \tilde{E}_j$. If we look at the energy range of $|\Delta E_{ij}| \simeq A$, the dominant $\Delta\tilde{E}_{ij}$ which appears in Eq. (2.97) has the same order of magnitude as A. Then the phase of the sine function in Eq. (2.97) should be 1 so that we observe the significant effect of the matter effect

$$AL = \frac{A[\mathrm{eV}]L[\mathrm{km}]}{197\mathrm{MeV}\cdot\mathrm{fm}} \sim L/[2000\mathrm{km}] \sim \mathcal{O}(1), \tag{2.98}$$

where $A = [\rho/(2.6\mathrm{g/cm}^3)] \times 10^{-13}[\mathrm{eV}] \sim \mathcal{O}(10^{-13})[\mathrm{eV}]$. This means that a longer baseline $L \gtrsim 1000\mathrm{km}$ is required.

2.4.3 Parameter Degeneracy in Neutrino Oscillations

The ultimate goal of neutrino oscillation phenomenology in the standard three flavor framework is to measure all the parameters of the MNS matrix and two squared-mass differences. The parameters except the Dirac CP phase δ, the octant sign$(\theta_{23} - \pi/4)$ and the mass hierarchy sign(Δm^2_{31}) have been measured in the neutrino oscillation experiments so far. The effort of determining the unknown parameters mentioned above was made by measuring the appearance oscillation probability $P_{\mu e} \equiv P(\nu_\mu \to \nu_e)$ in the Long BaseLine (LBL) experiments because that probabiliy is sensitive to θ_{13}, δ and the octant and mass hierarchy. Unfortunately, even if we obtain the probability $P_{\mu e}$ and that for the anti-neutrinos $\bar{P}_{\mu e} \equiv P(\bar{\nu}_\mu \to \bar{\nu}_e)$ for the fixed baseline length L and neutrino energy E exactly, these measurements give degenerate solutions for θ_{13}, δ, the octant and mass hierarchy. It is known as the eight-fold degeneracy discussed in Ref. [8] and the degeneracy is consist of three independent two-fold degeneracies which are the intrinsic degeneracy (θ_{13}, δ) [9], the hierarchy degeneracy [10] and the octant degeneracy [11]. We give a brief discussion on the eight-fold degeneracy and visualize it in the $(\sin^2 2\theta_{13}, 1/s^2_{23})$ plane as in Ref. [12]. Visualization in the $(\sin^2 2\theta_{13}, s^2_{23})$ plane is discussed in [13]. The reason why we adopt the visualization in the $(\sin^2 2\theta_{13}, 1/s^2_{23})$ plane is that this is the simplest way to understand the degeneracy.

Constant density matter is a good approximation in the LBL experiments. In this approximation, we can obtain the expression of the $\nu_\mu \to \nu_e$ $(\bar{\nu}_\mu \to \bar{\nu}_e)$ transition probabilities in the limit of $|\Delta m^2_{21}| \ll |\Delta m^2_{31}|, A$ and small θ_{13} [14, 8]. As in Ref. [8], we introduce the notation

$$\Delta \equiv \frac{|\Delta m^2_{31}| L}{4E} \tag{2.99}$$

$$\hat{A} \equiv \frac{A}{|\Delta m^2_{31}|} \tag{2.100}$$

$$\alpha \equiv \frac{|\Delta m^2_{21}|}{|\Delta m^2_{31}|}. \tag{2.101}$$

The oscillation probabilities $P_{\mu e}$ and $\bar{P}_{\mu e}$ for positive Δm^2_{21} and Δm^2_{31} can be expressed in terms of second order in θ_{13} and α

$$P_{\mu e} = x^2 f^2 + 2xyfg\,(\cos\delta\cos\Delta - \sin\delta\sin\Delta) + y^2 g^2 \tag{2.102}$$

$$\bar{P}_{\mu e} = x^2 \bar{f}^2 + 2xy\bar{f}g\,(\cos\delta\cos\Delta + \sin\delta\sin\Delta) + y^2 g^2 \tag{2.103}$$

where

$$x \equiv \sin\theta_{23}\sin 2\theta_{13} \tag{2.104}$$

$$y \equiv \alpha\cos\theta_{23}\sin 2\theta_{12} \tag{2.105}$$

$$f \equiv \frac{\sin\left(1-\hat{A}\right)\Delta}{\left(1-\hat{A}\right)} \tag{2.106}$$

$$\bar{f} \equiv \frac{\sin\left(1+\hat{A}\right)\Delta}{\left(1+\hat{A}\right)} \tag{2.107}$$

$$g \equiv \frac{\sin\left(\hat{A}\Delta\right)}{\hat{A}}. \tag{2.108}$$

On the other hand, the oscillation probabilities for the positive Δm^2_{21} and negative Δm^2_{31} are given by

$$P_{\mu e} = x^2\bar{f}^2 - 2xy\bar{f}g\left(\cos\delta\cos\Delta + \sin\delta\sin\Delta\right) + y^2g^2 \tag{2.109}$$

$$\bar{P}_{\mu e} = x^2 f^2 - 2xyfg\left(\cos\delta\cos\Delta - \sin\delta\sin\Delta\right) + y^2g^2. \tag{2.110}$$

To understand the three two-fold degeneracies which construct the eight-fold degeneracy separately, we discuss them step by step. First we set $\theta_{23} = \pi/4$, $\Delta m^2_{21} = 0$ and $A = 0$. This gives a completely degenerate solution to the octant, intrinsic and mass hierarchy. Second we set $\Delta m^2_{21} = 0$ and $A = 0$. This gives two solutions with the double two-fold degeneracies. The solutions are corresponding to the octant degeneracy. Thirdly we set $A = 0$. This gives four solutions with the two-fold degeneracy. Finally we discuss the most general case using the probabilities Eqs. (2.102), (2.103) (2.109) and (2.110).

In the case with ($\theta_{23} = \pi/4$, $\Delta m^2_{21} = 0$, $A = 0$), the oscillation probabilities are given by

$$P_{\mu e} = \bar{P}_{\mu e} = s^2_{23}\sin^2 2\theta_{13}\sin^2\Delta. \tag{2.111}$$

To visualize the degeneracy we introduce the variables

$$X \equiv \sin^2 2\theta_{13} \tag{2.112}$$

$$Y \equiv \frac{1}{s^2_{23}}. \tag{2.113}$$

When we measure the value of the oscillation probability for the fixed baseline length L and neutrino energy E in the LBL experiments, Eq. (2.111) can be expressed in terms of X and Y

$$Y = \frac{\sin^2 \Delta}{P} X. \tag{2.114}$$

This is a straight line in the $(\sin^2 2\theta_{13}, 1/s^2_{23})$ plane. From the assumption $\theta_{23} = \pi/4$, a solution to the oscillation parameters is given by the intersection of a straight line (2.114) and $Y = 2$. The intersection is depicted in Fig. 2.1 (the left panel).

In the case with ($\theta_{23} \neq \pi/4$, $\Delta m^2_{21} = 0$, $A = 0$), the oscillation probabilities are the same as Eq. (2.111). A difference between the first and this case is the value of Y. The atmospheric neutrino and LBL experiments measure the probability $P(\nu_\mu \to \nu_\mu)$ and we can extract the information on $\sin^2 2\theta_{23}$ from the data. We evaluate the value of Y by using that of $\sin^2 2\theta_{23}$. When θ_{23} is away from $\pi/4$, there are two possible values of Y

$$Y_+ = \frac{2}{1 + \sqrt{1 - \sin^2 2\theta_{23}}} \tag{2.115}$$

$$Y_- = \frac{2}{1 - \sqrt{1 - \sin^2 2\theta_{23}}}. \tag{2.116}$$

Then we obtain two solutions. One is a intersection of a straight line (2.114) and $Y = Y_+$ and the other is a intersection of a straight line (2.114) and $Y = Y_-$. These two solutions correspond to the octant degeneracy. The intersections are depicted in Fig. 2.1 (the right panel).

In the case with ($\theta_{23} \neq \pi/4$, $\Delta m^2_{21} \neq 0$, $A = 0$), the oscillation probabilities can be obtained by setting $\hat{A} = 0$ in Eqs. (2.102), (2.103), (2.109) and (2.110). Because the constant probability trajectories for the normal and inverted hierarchy are almost degenerate (the difference between them is order of α), we focus on the normal hierarchy. For the normal hierarchy ($\Delta m^2_{31} > 0$), the oscillation probabilities $P_{\mu e}$ and $\bar{P}_{\mu e}$ are expressed as follows

$$P_{\mu e} = x^2 \sin^2 \Delta + 2xy\Delta \sin \Delta (\cos\delta \cos\Delta - \sin\delta \sin\Delta) + y^2\Delta^2 \tag{2.117}$$

$$\bar{P}_{\mu e} = x^2 \sin^2 \Delta + 2xy\Delta \sin \Delta (\cos\delta \cos\Delta + \sin\delta \sin\Delta) + y^2\Delta^2. \tag{2.118}$$

As in the case discussed above, when we measure the oscillation probabilities $P_{\mu e} = P$ and $\bar{P}_{\mu e} = \bar{P}$ for the fixed baseline length L and neutrino energy E, Eqs. (2.117) and

(2.118) give a trajectory in the $(\sin^2 2\theta_{13}, 1/s^2_{23})$ plane

$$\begin{aligned} 16C_0X(Y-1)\sin^2\Delta &= \frac{1}{\sin^2\Delta}(P-\bar{P})^2Y^2 \\ &+\frac{1}{\cos^2\Delta}[(P+\bar{P}-2C_0)(Y-1)+P+\bar{P}-2X\sin^2\Delta]^2 \end{aligned} \tag{2.119}$$

where

$$C_0 \equiv \left(\frac{\Delta m^2_{21}}{\Delta m^2_{31}}\right)^2 \Delta^2 \sin^2 2\theta_{12}. \tag{2.120}$$

Eq. (2.119) draws a hyperbola unless Δ becomes π. Generally speaking, there are two intersections between the hyperbola (2.119) and constant value of Y. Because there are two possible values of Y in the case of $\theta_{23} \neq \pi/4$, the number of the intersection points is four. Then we have the four solutions with two-fold degeneracy. The intersections are depicted in Fig. 2.2.

In the case with ($\theta_{23} \neq \pi/4$, $\Delta m^2_{21} \neq 0$, $A \neq 0$), the oscillation probabilities were given in Eqs. (2.102), (2.103) (2.109) and (2.110). For the normal hierarchy (the inverted hierarchy), Eqs. (2.102) and (2.103), ((2.109) and (2.110)) give a trajectory in the $(\sin^2 2\theta_{13}, 1/s^2_{23})$ plane for the given oscillation probabilities $P_{\mu e} = P$ and $\bar{P}_{\mu e} = \bar{P}$ with the fixed baseline length L and the neutrino energy E. A trajectory for the normal hierarchy is

$$\begin{aligned} 16CX(Y-1) &= \frac{1}{\sin^2\Delta}\left[\left(\frac{P-C}{f}-\frac{\bar{P}-C}{\bar{f}}\right)(Y-1)-(f-\bar{f})X+\frac{P}{f}-\frac{\bar{P}}{\bar{f}}\right]^2 \\ &+\frac{1}{\cos^2\Delta}\left[\left(\frac{P-C}{f}+\frac{\bar{P}-C}{\bar{f}}\right)(Y-1)-(f+\bar{f})X+\frac{P}{f}+\frac{\bar{P}}{\bar{f}}\right]^2 \end{aligned} \tag{2.121}$$

and that for the inverted hierarchy is

$$\begin{aligned} 16CX(Y-1) &= \frac{1}{\sin^2\Delta}\left[\left(\frac{P-C}{\bar{f}}-\frac{\bar{P}-C}{f}\right)(Y-1)-(f-\bar{f})X+\frac{P}{\bar{f}}-\frac{\bar{P}}{f}\right]^2 \\ &+\frac{1}{\cos^2\Delta}\left[\left(\frac{P-C}{\bar{f}}+\frac{\bar{P}-C}{f}\right)(Y-1)-(f+\bar{f})X+\frac{P}{\bar{f}}+\frac{\bar{P}}{f}\right]^2 \end{aligned} \tag{2.122}$$

where

$$C \equiv \left(\frac{\Delta m^2_{21}}{\Delta m^2_{31}}\right)^2 \left[\frac{\sin\left(\hat{A}\Delta\right)}{\Delta}\right]^2 \sin^2 2\theta_{12}. \tag{2.123}$$

As in the previous case, the trajectories (2.121) and (2.122) give hyperbolas unless Δ becomes π. Then we have the eight solutions to $\sin^2 2\theta_{13}$and $1/s^2_{23}$ which give the same probabilities $P_{\mu e} = P$ and $\bar{P}_{\mu e} = \bar{P}$. The intersections are depicted in Fig. 2.3 (the left panel). One of the degenerated solutions is correct and the others are wrong. This is what we call the eight-fold degeneracy. We need additional measurements to resolve the degeneracy. In chapter 6, we discuss the octant degeneracy in the future atmospheric neutrino experiment Hyper-Kamiokande in detail.

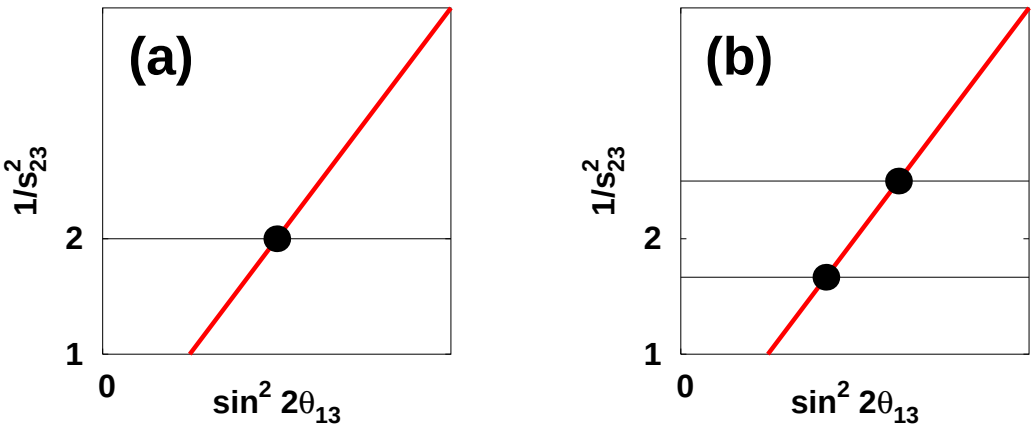

Figure 2.1: The constant probability trajectory for the case with ($\theta_{23} = \pi/4$, $\Delta m^2_{21} = 0$, $A = 0$) (the left panel) and ($\theta_{23} \neq \pi/4$, $\Delta m^2_{21} = 0$, $A = 0$) (the right panel) [12].

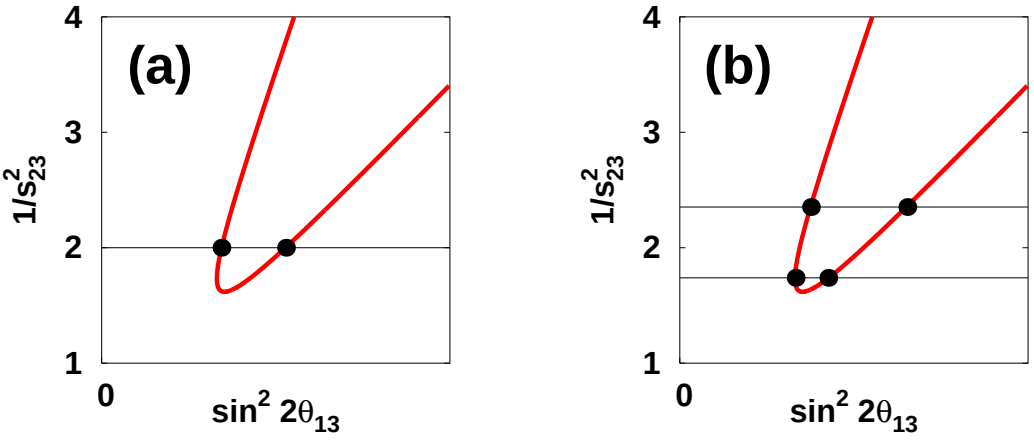

Figure 2.2: The constant probability trajectory for the case with ($\theta_{23} = \pi/4$, $\Delta m^2_{21} \neq 0$, $A = 0$) (the left panel) and ($\theta_{23} \neq \pi/4$, $\Delta m^2_{21} \neq 0$, $A = 0$) (the right panel) [12].

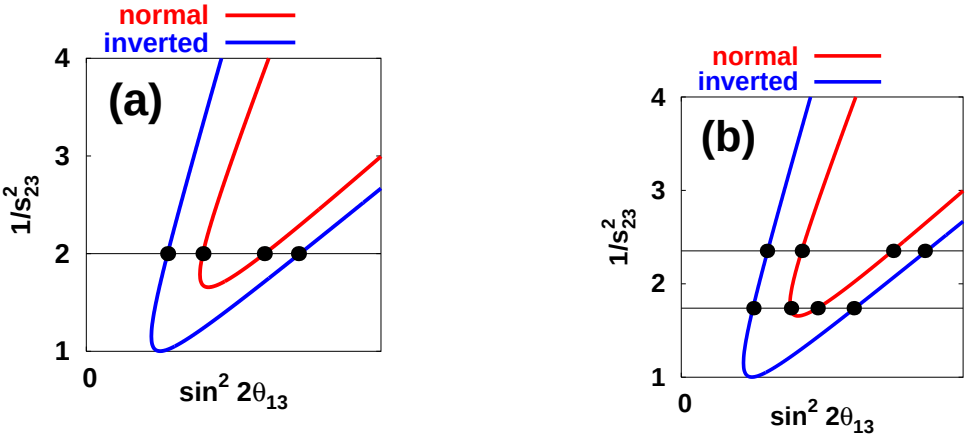

Figure 2.3: The constant probability trajectory for the case with ($\theta_{23} = \pi/4$, $\Delta m^2_{21} \neq 0$, $A = 0$) (the left panel) and ($\theta_{23} \neq \pi/4$, $\Delta m^2_{21} \neq 0$, $A = 0$) (the right panel) [12].

Chapter 3

Neutrino Oscillation Experiments

It is well established by solar, atmospheric, accelerator and reactor neutrino experiments that neutrinos have masses and mixings. In the standard three flavor neutrino oscillation framework, there are three mixing angles θ_{12}, θ_{13}, θ_{23}, the Dirac CP phase δ and two mass-squared differences Δm^2_{31}, Δm^2_{21}. These parameters can be determined by the neutrino oscillation experiments. In this chapter we give a brief review of the major experiments.

3.1 Solar Neutrinos

Almost all of solar neutrinos are produced by *pp* cycle which is a dominant reaction of thermonuclear at a temperature of the Sun. The *pp* cycle starts from the reactions

$$p + p \rightarrow {}^2H + e^+ + \nu_e, \tag{3.1}$$

$$p + e^- + p \rightarrow {}^2H + \nu_e. \tag{3.2}$$

Thereafter various nucleus are produced where neutrinos are emitted. Neutrino fluxes are categorized by the initial state of the reactions and spectra of solar neutrinos are predicted by the Standard Solar Model (SSM) [15]. The spectra are shown in Fig. 3.1.

3.1.1 Homestake

The Homestake experiment was the first experiment which detected solar neutrinos [17]. The Homestake experiment is located in the Homestake Gold Mine at Lead, in South Dakota, USA. The data was taken from 1968 to 1994 and the detector is a

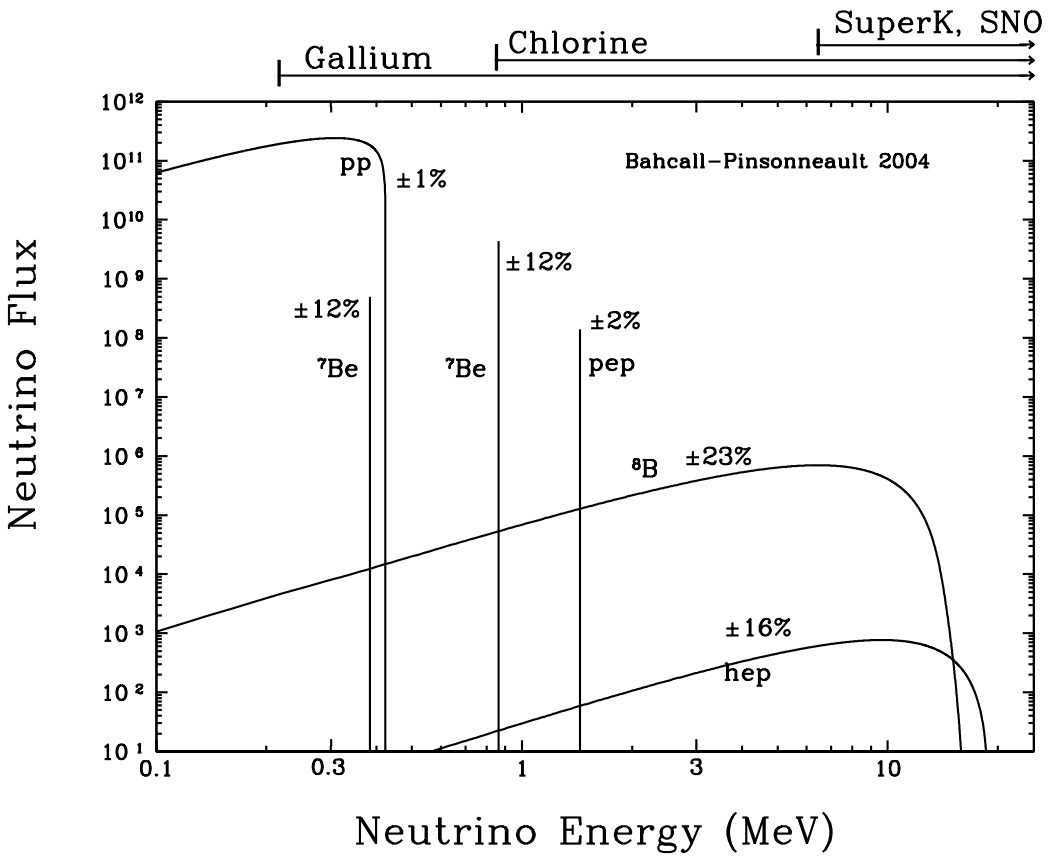

Figure 3.1: Spectra of solar neutrinos predicted by SSM [16]. The lines above the figure show the threshold energy for the experiments.

tank which is filled with 615 ton of tetrachloroethylene (C_2Cl_4). Solar neutrinos are detected via the reaction

$$\nu_e + {}^{37}\mathrm{Cl} \rightarrow {}^{37}\mathrm{Ar} + e^- \tag{3.3}$$

where the threshold energy for neutrinos is 0.814 MeV and hence only the high-energy solar neutrinos can be detected. ^{37}Ar in the tank is extracted with the chemical method about every two months because the lifetime of ^{37}Ar is about 35 days. The measured solar neutrino flux is less than the one predicted by SSM. This is what we called the solar neutrino problem. Disadvantages of this method are that we cannot detect solar neutrinos on an event by event basis and that the neutrino energy and direction cannot be measured. From these ambiguities, we cannot declare that the neutrinos detected by the Homestake experiment are coming from the Sun. However this problem is resolved by the Kamiokande solar neutrino experiments discussed later.

3.1.2 GALLEX/GNO and SAGE

Solar neutrinos can be also detected through the reaction

$$\nu_e + {}^{71}\mathrm{Ga} \rightarrow {}^{71}\mathrm{Ge} + e^- \tag{3.4}$$

with the low neutrino energy threshold which is 0.233 MeV. According to Fig. 3.1, all spectra of solar neutrinos can be detected through the above reaction. Experiments which detect solar neutrinos with the gallium reaction are called gallium solar neutrino experiments. Three gallium solar neutrino experiments were operated in the past.

One of the experiments is called GALLEX [18] located in Laboratori Nazionali del Gran Sasso, Italy. The data was taken from 1991 to 1997 with the detector of 101 ton liquid gallium chloride solution ($GaCl_3 - HCl$). GNO [19] is the experiments which took over the GALLEX detector with the improved method of extracting ^{71}Ge. GNO data was taken from 1998 to 2003. The observed solar neutrino flux is less than that of the SSM prediction.

The other gallium solar neutrino experiment is SAGE [20] located in the Baksan Neutrino Observatory, Russia. The target used in SAGE is about 50 ton gallium in the form of liquid metal. The data was taken from 1990 to 2001. The data in SAGE and that in GALLEX/GNO are consistent.

3.1.3 Kamiokande and Super-Kamiokande Solar Neutrino Experiment

Kamiokande and Super-Kamiokande (SK) are experiments with water Cherenkov detectors. In these experiments, neutrinos are detected on an event by event basis and the neutrino energy and direction can be measured.

Kamiokande and SK are multi purpose detectors. Originally, Kamiokande was planed to search the nucleon decay. After the improvement of detectors, Kamiokande was able to measure solar and atmospheric neutrinos. In this subsection we concentrate on the solar neutrino measurements in Kamiokande and SK. Kamiokande [21] was located in the Kamioka mine, Japan. The Kamiokande detector was filled with water of 3 kton. In Kamiokande, solar neutrinos were measured through the elastic scattering process

$$\nu_\alpha + e^- \to \nu_\alpha + e^- \qquad (\alpha = e, \mu, \tau). \tag{3.5}$$

The Cherenkov light emitted by the electrons scattered with neutrinos were measured by using photomultiplier tube (PTM). The dominant channel is the electron neutrino channel because the cross-section for the electron neutrinos is approximately six times larger than that for mu and tau neutrinos. The directions of neutrinos and electrons are strongly correlated and hence we can distinguish the neutrinos coming from the Sun from the isotropic background. There were three phases in the Kamiokande. The first phase called Kamiokande-I was designed to search the nucleon decay with the order of 1 GeV energy threshold. The second phase called Kamiokande-Ⅱ in which the energy threshold was lowered and Kamiokande observed ^{8}B solar neutrinos. The final phase called Kamiokande-Ⅲ was started with the replacement of about 100 dead PMTs. The ^{8}B solar neutrino flux measured in Kamiokande is about half of that of the SSM prediction.

SK [22] which was started in 1996 is a successor experiment of Kamiokande and is located in Kamioka mine as in the case with Kamiokande. The SK has two detectors. Main detector is called the inner detector and filled with water of 50 kton and the fiducial volume is 22.5 kton and the other is called the outer detector. The detection principle is the same as Kamiokande. There are four phases in the currently running experiment SK. There was an accident in 2001. More than half of PMT were broken. A phase before the accident is called SK-I. Then repair works were carried out along with measuring the neutrinos. The repair works were completed in 2006. A phase during repairing process is called SK-Ⅱ. In 2008, electronics were upgraded in order to measure the neutrinos with stability for a long time. A phase before the upgrade is called SK-Ⅲ and that after the upgrade currently being operated is called SK-Ⅳ.

What SK measures in SK are the ^{8}B solar neutrino flux and the day/night effect. The day/night effect is due to a difference between the day and night solar neutrino fluxes because only neutrinos measured at night go through the Earth. The measured ^{8}B solar neutrino flux is also smaller than that of SSM prediction.

3.1.4 SNO

SNO [23] is a water Cherenkov detector filled with pure heavy water D_2O located in Creighton Mine, Canada. Data was taken from 1999 to 2006. Solar neutrinos were measured in SNO through the three reactions

$$\nu_e + D \rightarrow p + p + e^- \tag{3.6}$$
$$\nu_\alpha + D \rightarrow p + n + \nu_\alpha \tag{3.7}$$
$$\nu_\alpha + e^- \rightarrow \nu_\alpha + e^- \tag{3.8}$$

where $\alpha = e, \mu, \tau$. The third reaction is the same reaction as SK. The differences between SNO and SK are the first and second reactions due to heavy water. The most important reaction is the second NC reaction because the cross sections for NC reaction are the same for all the neutrino flavors. Hence we can check not only the electron neutrino flux but also the total sum of all the neutrino flavor fluxes. All the reactions are sensitive only to the ^{8}B solar neutrino flux as in the case of SK. The results of the measured fluxes through the reactions mentioned above are given in Ref. [24]. The measured fluxes can be expressed in terms of the ν_e flux and the $(\nu_\mu + \nu_\tau)$ flux. Solutions for the measured fluxes are shown in Fig. 3.2. The solutions obtained from each reaction are consistent. The value of $(\nu_e + \nu_\mu + \nu_\tau)$ flux are consistent with the flux predicted by SSM. From these results, we conclude that a part of the electron neutrinos produced in the Sun oscillate into mu and tau neutrinos.

3.1.5 Borexino

Borexino [25] is a solar neutrino experiment which aim to detect the low energy ^{7}Be solar neutrinos with energy 0.862 MeV located in Laboratori Nazionali del Gran Sasso, Italy. The Borexino detector is filled with liquid scintillator of 300 ton. The best-fit value for the interaction rate is

$$R_{\text{Borexino}} = 46.0 \pm 1.5(\text{stat.})^{+1.5}_{-1.6}(\text{syst.})\text{counts}/(\text{day} \cdot 100\text{ton}). \tag{3.9}$$

This is 5.0σ lower than the SSM prediction.

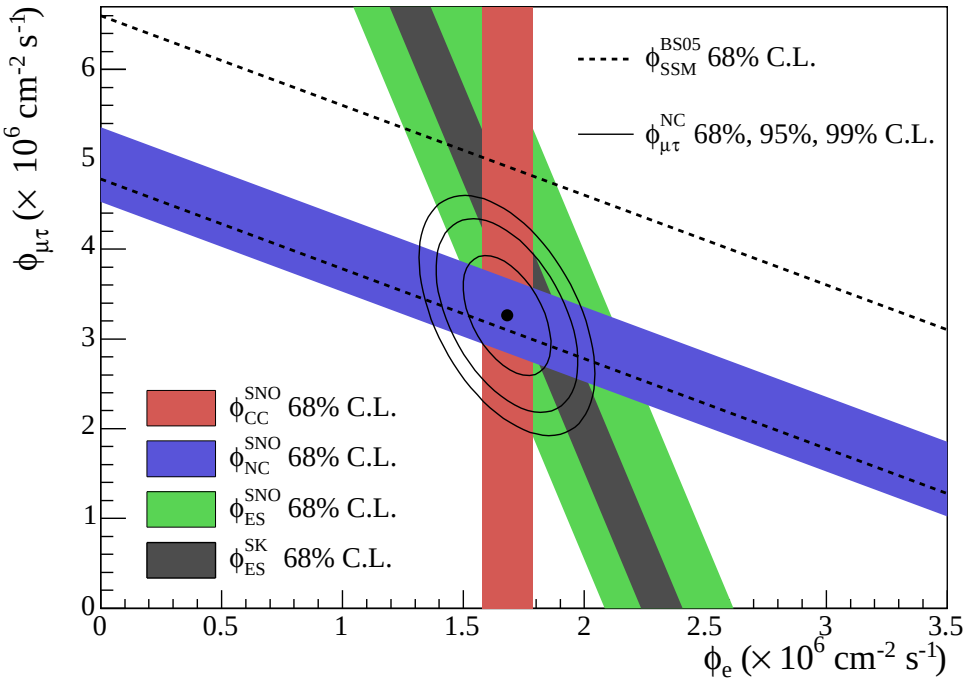

Figure 3.2: Solutions to the measured fluxes[24]. $\phi_{\mu\tau}$ stands for the ν_e flux and the $(\nu_\mu + \nu_\tau)$ flux and ϕ_e stands for the ν_e flux.

3.2 Atmospheric Neutrinos

Atmospheric neutrinos are produced by the collision between primary cosmic rays which mainly consist of protons and the nuclei in the atmosphere. After the collision, secondary cosmic rays are produced. Especially $\pi^{\pm}$ and $K^{\pm}$ in the secondary cosmic rays decay into neutrinos rapidly before hitting the Earth because their life time is short. A main contribution to the atmospheric neutrino flux is pion. Kaons also contribute to that at the high energy. Pions produced by the primary cosmic rays decay mainly into muons and mu neutrinos

$$\pi^+ \rightarrow \mu^+ + \nu_\mu, \tag{3.10}$$
$$\pi^- \rightarrow \mu^- + \bar{\nu}_\mu, \tag{3.11}$$

and muons produced by the pion decay subsequently decay into electrons, electron and mu neutrinos

$$\mu^+ \rightarrow e^+ + \nu_e + \bar{\nu}_\mu, \tag{3.12}$$
$$\mu^- \rightarrow e^- + \bar{\nu}_e + \nu_\mu. \tag{3.13}$$

Muons with the energy below about 1 GeV can decay before hitting the ground. In those energy regions, we find that the ratio of mu neutrino flux to electron neutrino flux

$$\frac{\phi_\mu + \bar{\phi}_\mu}{\phi_e + \bar{\phi}_e} \simeq 2. \tag{3.14}$$

At the energy above about 1 GeV, the ratio increases. Direction averaged atmospheric neutrino flux and the flavor ratios are shown as a function of neutrino energy in Fig. 3.3 and distributions of neutrino energies are shown in Fig. 3.4. The zenith angle dependence of the atmospheric neutrino fluxes at Kamioka are shown in Fig. 3.5.

The latest atmospheric neutrino fluxes are calculated with 3-dimensional treatment. In the 3D calculation, effects of the geomagnetic field and the 3-dimensional topology of the interactions are considered. Difference between 3D and 1D calculations is an enhancement of the flux for the horizontal direction which can be easily seen from Fig. 3.5. This is because the effective are of 3D calculation in which atmospheric neutrinos produced by the interactions of cosmic rays are larger than that of 1D.

As in Fig. 3.4, atmospheric neutrino events are categorized as follows

- **Fully Contained (FC) events** are events in which the neutrinos interact with water in the detector and the all particles produced by the interaction are contained in the inner detector.

- **Partially Contained (PC) events** are events in which the neutrinos interact with water in the detector and then a part of particles produced by the interaction are contained in the inner detector and the others are stopping in the outer detector.

- **Upward-through-going muon** are events in which the neutrinos coming from the below interact with the rock near the detector and muons produced by the interaction go through the detector.

- **Upward-stopping-going muon** are events in which the neutrinos coming from the below interact with the rock near the detector and muons produced by the interaction stop in the detector.

- **Sub-GeV Events** are events which are the FC events with the energy below 1.33 GeV.

- **Multi-GeVEvents** are events which are the FC events with the energy above 1.33 GeV.

One of the reason why atmospheric neutrino events are divided as mentioned above is that a correlation of scattering angle between incoming neutrinos and outgoing charged leptons is different in these categories.

3.2.1 Kamiokande Atmospheric Neutrino Experiment

The main features of Kamiokande were explained in subsection 3.1.3. As mentioned above Kamiokande is the water Cherenkov detector and hence measures the Cherenkov light emitted by electrons and muons produced by neutrino interactions. A event in which the detected Cherenkov light is considered to be a light which is emitted by electrons(muons) is called $e(\mu)$-like event. Atmospheric neutrino oscillation were firstly indicated in 1988 by Ref. [29] in which a measured flux of atmospheric electron neutrinos is consistent with the prediction, while that of atmospheric mu neutrinos is 59$\pm$7% (stat.) less than the prediction. This is called the atmospheric neutrino anomaly. After that Kamiokande measured so called a double ratio defined as

$$R_{\mu/e} \equiv \frac{(N_{\mu-\mathrm{like}}/N_{e-\mathrm{like}})_{\mathrm{data}}}{(N_{\mu-\mathrm{like}}/N_{e-\mathrm{like}})_{\mathrm{MC}}} \tag{3.15}$$

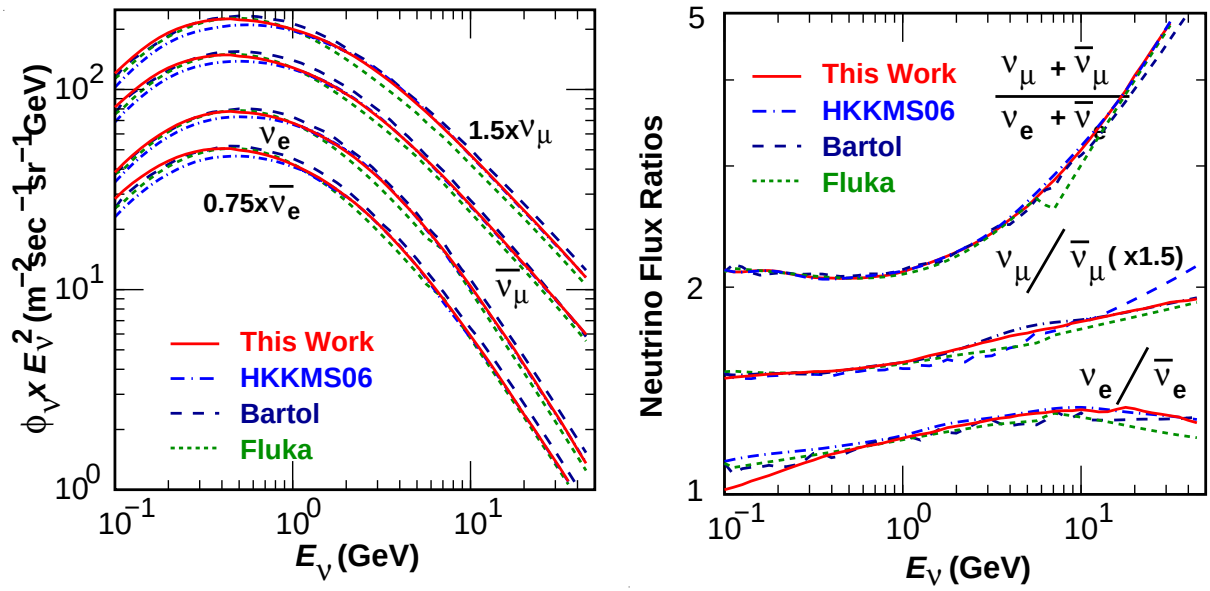

Figure 3.3: Direction averaged atmospheric neutrino flux predictions (left) and the flux ratio predictions (right) [26]. Red lines correspond to Honda 2011 flux.

where $N_{e(\mu)-\text{like}}$ stand for the number of $e(\mu)-$like events. The subscripts data and MC stand for the measurements and predictions by Monte Carlo simulation, respectively. The double ratio for sub-GeV events [30] is

$$R_{\mu/e}^{\text{sub}} = 0.60^{+0.07}_{-0.06}(stat.) \pm 0.05(syst.), \tag{3.16}$$

and that for multi-GeV events [31] is

$$R_{\mu/e}^{\text{multi}} = 0.57^{+0.08}_{-0.07}(stat.) \pm 0.07(syst.). \tag{3.17}$$

They are smaller than are expected and this anomaly can be explained by neutrino oscillations between $\nu_\mu \leftrightarrow \nu_\tau$.

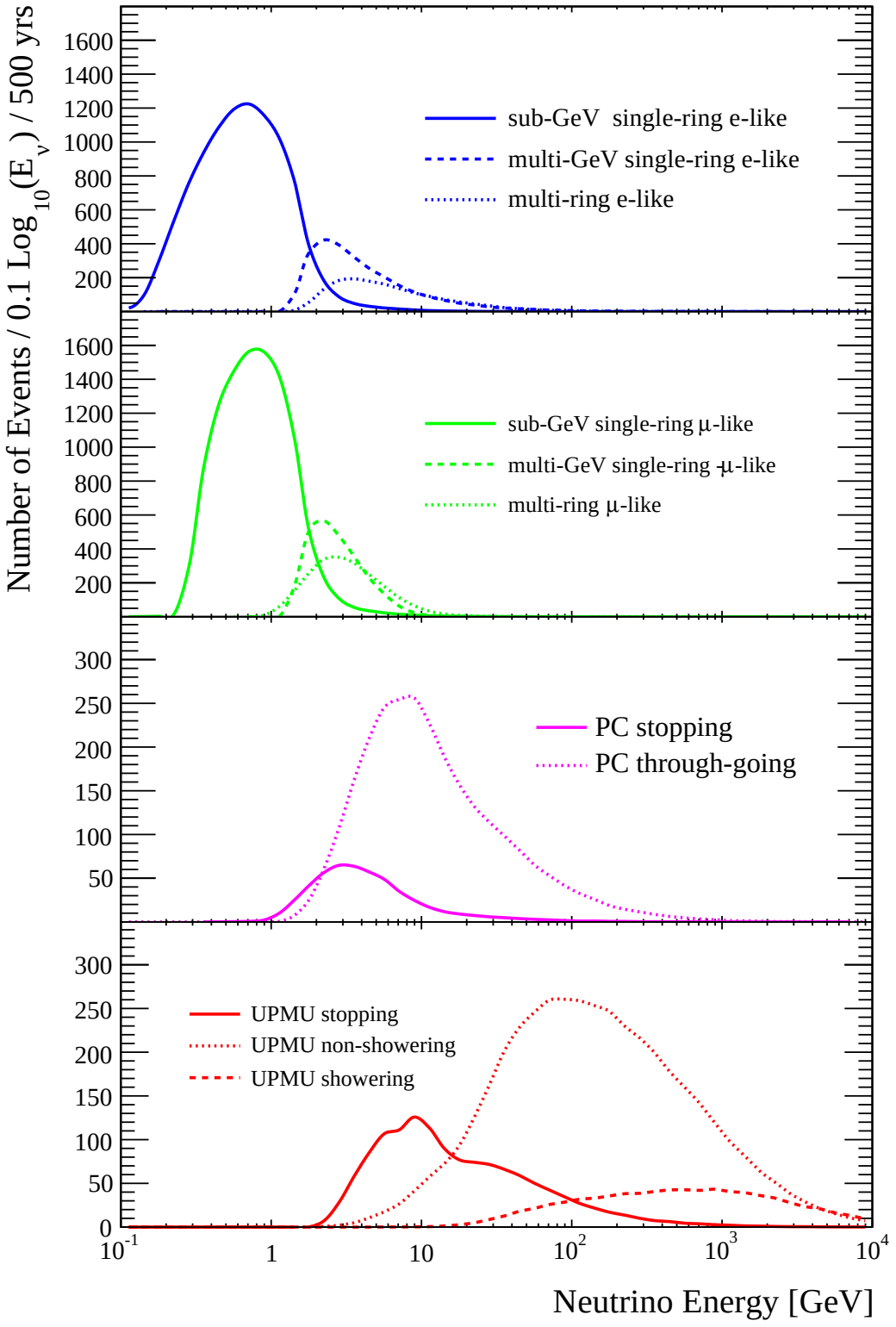

Figure 3.4: Distributions of neutrino energies for each sub-sample [27].

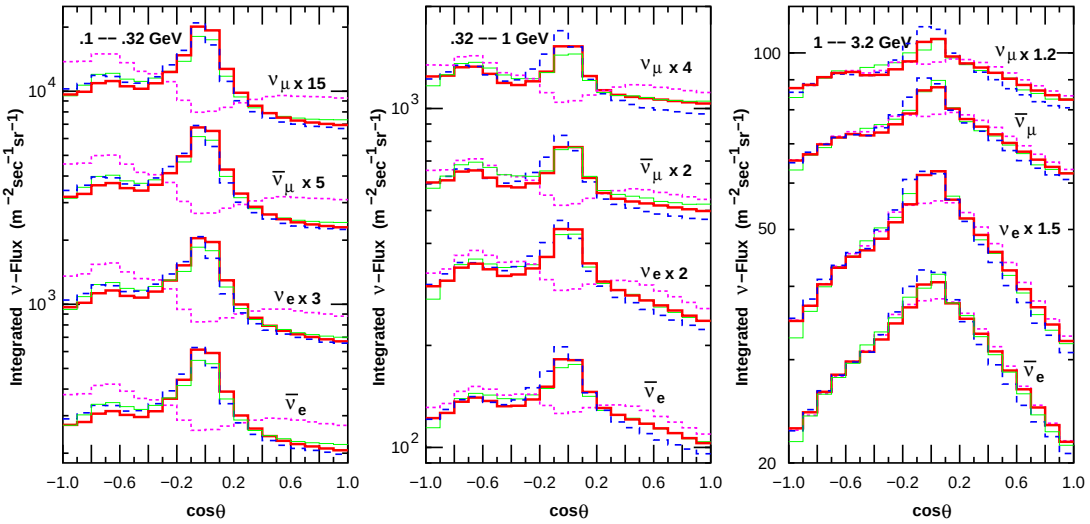

Figure 3.5: The zenith angle dependence of the atmospheric neutrino fluxes at Kamioka [28]. The red thick solid lines are for 3D calculation and pink dotted lines are for 1D calculation. The others are calculated by other groups.

3.2.2 Super-Kamiokande Atmospheric Neutrino Experiment

As in the case with Kamiokande, the main features of SK detector were explained in subsection 3.1.3. In SK, CC and NC interactions are considered

$$\begin{aligned}
\text{CC/NC (Quasi-)Elastic Scattering} \quad & \nu \quad + N \to \ell + N' \\
\text{CC/NC Single Meson Production} \quad & \nu \quad + N \to \ell + N' + meson \\
\text{CC/NC Deep Inelastic Scattering} \quad & \nu \quad + N \to \ell + N' + hadrons \\
\text{CC/NC Choherent Pion Production} \quad & \nu \quad + {}^{16}O \to \ell + {}^{16}O + \pi,
\end{aligned}$$

where $N^{(\prime)}$ stand for nucleons and ℓ stands for leptons. Typically the cross-sections for neutrinos are twice as large as that for anti-neutrinos.

First indication of atmospheric neutrino oscillation was presented in 1998 by SK [32]. SK measured up-down asymmetry defined as

$$A_\alpha^{\text{up-down}} \equiv \left(\frac{U - D}{U + D} \right)_\alpha \tag{3.18}$$

where U stands for the number of upward-going events, D stands for the number of downward-going events and $\alpha = e, \mu$ stands for the α-like events. Notice that the

high-energy atmospheric neutrino flux is up-down symmetric because the primary cosmic ray is isotropic and the effect of geomagnetic field is negligible at high-energy. The result [32] was

$$A_{\mu}^{\text{up-down}} = -0.296 \pm 0.048 \pm 0.01, \tag{3.19}$$

$$A_{e}^{\text{up-down}} = -0.036 \pm 0.067 \pm 0.02. \tag{3.20}$$

The up-down asymmetry for the μ-like events is a 6σ model-independent evidence of upward-going muon events deficit. On the other hand, that for e-like events is consistent with the prediction. These results can be explained by the $\nu_\mu \leftrightarrow \nu_\tau$ oscillation scenario.

Notice that SK can measure atmospheric neutrinos with high statistics for various neutrino energies and baselines but there are some uncertainties. For instance, the uncertainties of density profile of the Earth and the weak scattering angle correlation between neutrinos and charged leptons in the sub-GeV events may prevent us from detecting physics beyond the SM or determining the oscillation parameter precisely.

The latest SK results of oscillation parameter determination are presented in Ref. [33]. For the normal hierarchy the best-fit values are

$$\sin^2\theta_{23} = 0.575 \tag{3.21}$$

$$\Delta m^2_{31} = 2.6 \times 10^{-3}\ \text{eV}^2 \tag{3.22}$$

$$\delta = 4.19, \tag{3.23}$$

and, for the inverted hierarchy, the best-fit values are

$$\sin^2\theta_{23} = 0.575 \tag{3.24}$$

$$\Delta m^2_{31} = -2.3 \times 10^{-3}\ \text{eV}^2 \tag{3.25}$$

$$\delta = 3.84. \tag{3.26}$$

3.2.3 Hyper-Kamiokande Atmospheric Neutrino Experiment

Hyper-Kamiokande (HK) is the future neutrino oscillation experiment which aims to obtain neutrino measurements with high precision and also to search for nucleon decay. The HK letter of intent was published in 2011 [34] and the experimental setup and physics potentials were discussed. Thereafter the physics potential of determining the Dirac CP phase δ using the HK and a neutrino beam from J-PARC as the far detector and neutrino source, respectively, were presented [35]. In Ref. [35], a candidate site of HK is assumed to be at Tochibora mine, Kamioka town,

Gifu, JAPAN. HK is a water cherenkov detector like as the predecessor experiment Super-Kamiokande (SK) and the HK fiducial volume is assumed to be 0.56 Mton. Recently the plan of HK is changed. According to Kajita's talk in 1st atmospheric neutrino workshop, the detector design is changed to the one similar to SK and whose fiducial volume is 0.38 Mton because the cost for the previous design is too expensive. However, it is expected that decreasing of the number of events due to a reduced fiducial volume can be compensated by the improvement of the detection efficiencies of the photomultiplier.

3.3 Accelerator Neutrinos

3.3.1 K2K

The K2K experiment [36] was the first long baseline neutrino oscillation experiment in which measured neutrinos are artificially produced by the decay of pions produced by the collision between the targets and accelerated protons. K2K is called a long-baseline accelerator based neutrino experiment because the measured neutrinos are produced by the accelerator in KEK, Japan. The neutrino beam which is an almost pure ν_μ beam with a mean energy of 1.3 GeV is detected by the SK detector 250 km far from KEK. K2K was operated from 1999 to 2004. The main aim of K2K is to check the atmospheric neutrino oscillations in the laboratory. In a two flavor oscillation framework discussed in Section 3.5, the best-fit values for oscillation parameters related to atmospheric neutrino oscillations are

$$\sin^2 2\theta_{23} = 1.0, \tag{3.27}$$

$$|\Delta m^2_{31}| = 2.8 \times 10^{-3}\ \mathrm{eV}^2. \tag{3.28}$$

3.3.2 T2K

The T2K experiment [37, 38, 39, 40] is a successor experiment of K2K and is a currently running experiment. A neutrino narrow-band beam with a peak energy of 0.6 GeV is sent from J-PARC located in Tokai, Japan to the SK detector and the baseline length is 295 km. T2K can analyzes in a three flavor oscillation framework unlike K2K and can extract several oscillation parameters. T2K measure the neutrino mode during a period from 2010 to 2013 and the anti-neutrino mode from 2014. From the neutrino mode measurements [40] which include the $\nu_\mu \to \nu_\mu$ and $\nu_\mu \to \nu_e$

channels, the best-fit values for the normal hierarchy ($\Delta m^2_{31} > 0$) are

$$\begin{aligned} \Delta m^2_{31} &= 2.51 \times 10^{-3}\ \mathrm{eV}^2 \\ \sin^2\theta_{23} &= 0.524 \\ \sin^2\theta_{13} &= 0.0422 \\ \delta &= 1.91 \end{aligned}$$

and those for the inverted hierarchy ($\Delta m^2_{31} < 0$) are

$$\begin{aligned} \Delta m^2_{31} &= -2.49 \times 10^{-3}\ \mathrm{eV}^2 \\ \sin^2\theta_{23} &= 0.523 \\ \sin^2\theta_{13} &= 0.0491 \\ \delta &= 1.01. \end{aligned}$$

The results from the anti-neutrino mode are presented in Ref. [39] and consistent with the existing anti-neutrino experiments and the T2K $\nu_\mu \to \nu_\mu$ results. Notice that the best-fit value of θ_{13} from T2K data is lager than that from Reactor experiments presented later. Also there is a tension between the value of θ_{23} from T2K and that from NOνA experiment also presented later. T2K favors the maximal mixing of θ_{23} whereas the best-fit value of θ_{23} from NOνA is away form the maximal mixing.

3.3.3 MINOS

The MINOS experiment [41] is an accelerator experiment. An on-axis neutrino beam with a peak energy of 3 GeV sent from Fermilab, US is detected at the Soudan Underground Mine and a baseline length is 735 km. The neutrino beam mostly consists of ν_μ. The main MINOS detector is 5.4 kton steel-scintillator tracking calorimeters with toroidal magnetic fields. In addition to the neutrino beam, MINOS measures atmospheric neutrinos. The magnetized MINOS detector can separate neutrinos from anti-neutrinos through the CC interactions

$$\nu_\mu + X \to \mu^- + X' \tag{3.29}$$

$$\bar{\nu}_\mu + X \to \mu^+ + X'. \tag{3.30}$$

Data have been collected since 2005. MINOS presented the oscillation parameters in the two flavor framework extracted from the combined MINOS beam and atmospheric neutrino data [41]. Assuming that the oscillation parameters for neutrinos

and that for anti-neutrinos are the same, the best-fit values extracted from the neutrino sample are

$$\begin{aligned} |\Delta m^2_{31}| &= \left(2.4^{+0.09}_{-0.10}\right) \times 10^{-3}\ \mathrm{eV}^2 \\ \sin^2 2\theta_{23} &= 0.95^{+0.035}_{-0.036} \end{aligned}$$

and that from anti-neutrino sample are

$$\begin{aligned} |\Delta m^2_{31}| &= \left(2.5^{+0.23}_{-0.25}\right) \times 10^{-3}\ \mathrm{eV}^2 \\ \sin^2 2\theta_{23} &= 0.97^{+0.03}_{-0.08}. \end{aligned}$$

There is a good agreement between neutrino and anti-neutrino samples.

3.3.4 NOνA

The NOνA experiment [42, 43] is an accelerator experiment which uses an upgraded beam used in MINOS. The NOνA beam is an off-axis beam with a peak energy of 2 GeV. The main NOνA detector is located in Minnesota, US and 810 km away from Fermilab. The NOνA detector is composed of cells of liquid scintillator with a total mass of 14 kton and has sensitivities to the reactions as follows

$$\begin{aligned} \text{CC (Quasi-)Elastic Scattering} \quad & \nu_\mu \quad + N \to \mu^- + X' \\ \text{CC EM shower} \quad & \nu_e \quad + N \to e^- + X \\ \text{NC single } \pi^0 \text{ production} \quad & \nu \quad + N \to X + \pi^0. \end{aligned}$$

The NOνA [42] presented the results for the oscillation parameters as follows

$$\begin{aligned} |\Delta m^2_{32}| &= \left(2.52^{+0.20}_{-0.18}\right) \times 10^{-3}\ \mathrm{eV}^2 \\ \sin^2\theta_{23} &= 0.43 \quad \text{or} \quad \sin^2\theta_{23} = 0.60. \end{aligned}$$

As mentioned above, there is a tension between T2K and NOνA results for the value of θ_{23}.

3.4 Reactor Neutrinos

In this section, we give a review of two types of reactor neutrino experiments. One is a experiment which aims to measure the mixing angle θ_{13} and the other is a experiment which aims to measure the oscillation parameters related to the solar neutrino

oscillations. The former is the Double Chooz, Daya Bay and RENO experiments and the latter is the KamLand experiment.

Reactor neutrinos are produced by the nuclear fission at reactors and detected by the inverse β-decay reaction

$$\bar{\nu}_e + p \to e^+ + n. \tag{3.31}$$

In this reaction photons emitted by the pair annihilation of the positrons in the final state and surrounding electrons are detected. This signal is separated from the background by the delayed signal produced by the nuclear capture of the neutron. The peak of the anti-neutrino detection is at the energy of about 3.6 MeV.

3.4.1 Double Chooz

The Double Chooz experiment [44, 45] located in the Ardennes department, France is a reactor experiment in which measured $\bar{\nu}_e$ are produced by nuclear fission at the Chooz reactor. Double Chooz is a successor experiment of the Chooz experiment [46] which presented the upper limit on the value of θ_{13}

$$\sin^2 2\theta_{13} \lesssim 0.1 \quad \text{for} \quad |\Delta m^2_{31}| \sim 3 \times 10^{-3}\ \text{eV}^2. \tag{3.32}$$

A main goal of Double Chooz is to measure the precise value of θ_{13}. Double Chooz has the near and far detector which are 400 m and 1050 m far from the Chooz reactor, respectively. The near and far detector has collected data since 2015 and 2011, respectively. The Double Chooz neutrino detectors consist of three cylindrical tanks. The most inner tank is a 10.3 m^3 Gd-doped liquid scintillator detector as a neutrino target, the next tank is a 23 m^3 liquid scintillator detector which measures an energy of gamma ray escaping from the neutrino target, and the outer tank is a 110 m^3 paraffin oil buffer region.

In 2011 Double Chooz observed the disappearance of reactor electron antineutrinos [44]. This is the first indication of the non-zero θ_{13} from the reactor neutrino experiments. After that Double Chooz presented the result for the value of θ_{13} [45] and the best-fit value is

$$\sin^2 2\theta_{13} = 0.109 \pm 0.030 \pm 0.025. \tag{3.33}$$

3.4.2 Daya Bay

The Daya Bay experiment [47, 48] is the first experiment which observed the value of non-zero θ_{13} with more than 5 σ (March, 2012). The Daya Bay experiment is located

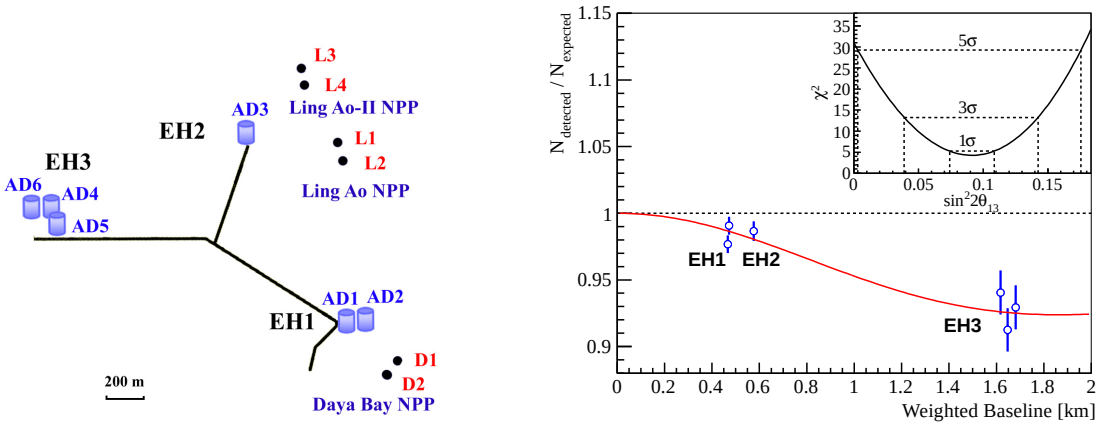

Figure 3.6: The layout of Daya Bay experiment (left). D1-2, L1-4 represent reactors, AD1-6 represent detectors, and EH1-3 represent experimental halls. The measured event ratio of neutrinos to expectation for each detector (right). In the no oscillation scenario, the ratio should be one. The red line stand for the prediction with the neutrino oscillations using measured value of θ_{13} [47].

at Daya Bay, China and layout of it is shown in Fig. 3.6 (left). There are six reactors and six neutrino detectors and baseline lengths between them are listed in Table 3.1. The Daya Bay detectors consist of three cylindrical layers. The most inner layer is a 20 ton 0.1 % Gd-doped liquid scintillator detector as a neutrino target, the medium layer is a pure 20 ton liquid scintillator detector and the most outer layer is 40 ton mineral oil buffer region.

In the three flavor neutrino oscillation framework analysis, Daya Bay presented the results of the value of θ_{13} [48]

$$\sin^2 2\theta_{13} = 0.071 \pm 0.011. \tag{3.34}$$

	D1,2	L1,2	L3,4
EH1	364	857	1307
EH2	1348	480	528
EH3	1912	1540	1548

Table 3.1: The baseline lengths (m) between experimental halls and reactors.

3.4.3 RENO

The RENO experiment [49, 50] located in South Korea presented the result of θ_{13} measurement one month after the announcement by Daya Bay. The result excluded the no neutrino oscillation hypothesis at 4.9σ. RENO has the near and far detectors similar to the Double Chooz and Daya Bay detectors. The near and far detectors are 294 m and 1383 m far from the reactor, respectively. The RENO detectors consist of three cylindrical tanks. The most inner tank is a 18.6 m^3 Gd-doped liquid scintillator detector as a neutrino target, the next tank is a 60 cm thick layer liquid scintillator detector, and the outer tank is a 65 ton mineral oil buffer region. The up-to-date result of RENO θ_{13} measurement [50] is

$$\sin^2 2\theta_{13} = 0.082 \pm 0.009 \pm 0.006. \tag{3.35}$$

3.4.4 KamLAND

The KamLAND experiment [51, 52, 53] is a experiment whose baselines are longer than those of the reactor experiments mentioned above. KamLAND was designed to detect electron anti-neutrinos produced by 53 reactors in Japan. About 80% of the $\bar{\nu}_e$ flux comes from 26 reactors located at an average distance of about 180 km. This configuration allows us to confirm so called the Large Mixing Angle (LMA) solution to the solar neutrino problem to be discussed in subsection 3.5.1 by looking at a L/E spectral distortion and data was taken from 2002 to 2009.

The KamLAND detector is located in the Kamioka mine. The location is the space which was used by the Kamiokande experiment. The KamLAND detector is a spherical balloon with 1 kton ultra pure liquid scintillator. The first KamLAND result which is the ratio of measured $\bar{\nu}_e$ flux with an energy above 3.4 MeV to the prediction was presented in 2002 [51]

$$R = 0.611 \pm 0.085 \pm 0.041. \tag{3.36}$$

This result exclude all solutions to the solar neutrino problem except for the LMA solution.

In 2008, KamLAND presented the most precise measurement of Δm^2_{21}. The good sensitivity of KamLAND to Δm^2_{21} is due to the L/E spectral distortion. By combining the KamLAND and solar neutrino experiments data, the oscillation parameters related to the solar neutrino oscillations in the two flavor framework are determined as follows

$$\Delta m^2_{21} = 7.59^{+0.21}_{-0.21} \times 10^{-5}\mathrm{eV}^2 \tag{3.37}$$

$$\tan^2\theta_{12} = 0.47^{+0.06}_{-0.05}. \tag{3.38}$$

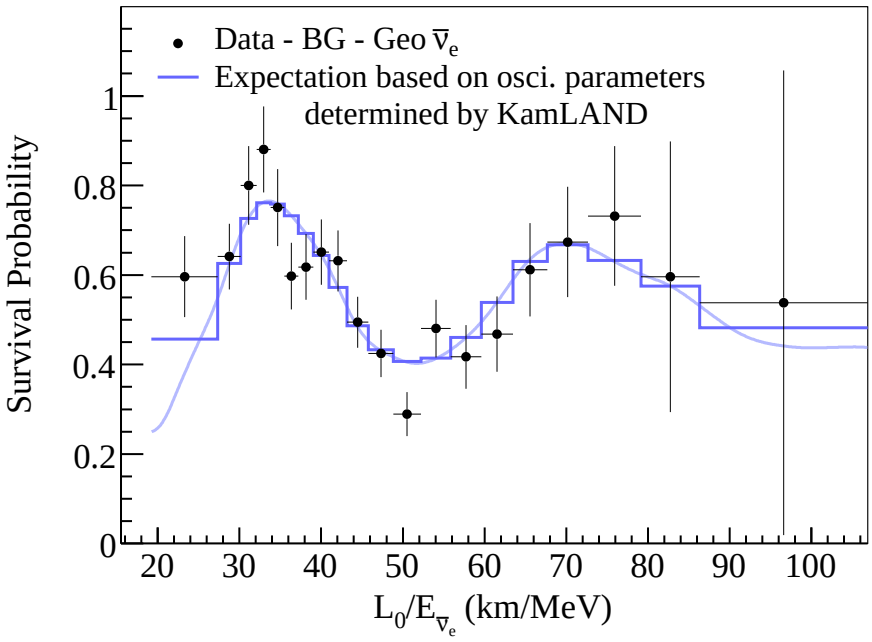

Figure 3.7: The measured reactor $\bar{\nu}_e$ energy spectrum in KamLAND as a function of L_0/E [52]. $L_0 = 180$ km is the effective baseline taken as a flux-weighted average.

Notice that there is a tension in which Δm^2_{21} extracted from the global fit of the solar neutrinos is 2σ smaller than that from the KamLAND experiment.

In 2010, KamLAND presented the neutrino oscillation parameter measurements in the three flavor framework [53]

$$\Delta m^2_{21} = 7.50^{+0.19}_{-0.20} \times 10^{-5}\text{eV}^2 \quad (3.39)$$

$$\tan^2\theta_{12} = 0.452^{+0.035}_{-0.033} \quad (3.40)$$

$$\sin^2\theta_{13} = 0.020^{+0.016}_{-0.016}. \quad (3.41)$$

In the analysis θ_{13} was taken as a free parameter and a non-zero θ_{13} is indicated with only 79% C.L.

3.5 Global Analysis of Neutrino Oscillation Experiments Data

The oscillation probabilities in the three flavor framework can be reduced to an effective two flavor form. This is due to the hierarchy of mass-squared differences and the small value of θ_{13}. Before the results on θ_{13} by T2K and the reactor neutrino experiments, θ_{13} was considered to be a very small parameter. Although we know the non-zero and not extremely small value of θ_{13}, the two flavor reduction is still valid to a good approximation. The smaller (Δm^2_{21}) and larger ($\Delta m^2_{31} \simeq \Delta m^2_{32}$) mass-squared differences correspond to solar and atmospheric scale mass-squared differences, respectively. The ratio of $|\Delta m^2_{21}|$ to $|\Delta m^2_{31}|$ is about 1/30. Scenarios can be divided into two cases. One is the case driven by the larger mass-squared difference Δm^2_{31} and the other is the case driven by the smaller one Δm^2_{21}. In the case driven by Δm^2_{31}, the effects of Δm^2_{21} are small. On the other hand, in the case driven by Δm^2_{21}, the effects of Δm^2_{31} are washed out.

Recently neutrino experiments have reached a point where the effects of three neutrino mixing can be measured. In this section we discuss some oscillation probabilities used in the experiment analysis and give the best-fit oscillation parameters from the global analysis of neutrino oscillation experiments data.

3.5.1 Neutrino Oscillation Analysis Driven by Δm^2_{21}

The neutrino oscillations driven by Δm^2_{21} are the solar neutrino and long baseline reactor neutrino oscillation in which the (anti) electron neutrino survival oscillation probabilities are measured.

The solar neutrino survival probability $P(\nu_e \to \nu_e)$ is approximately driven by one mass-squared difference Δm^2_{21} and given by

$$P(\nu_e \to \nu_e) = c^4_{13} P_{\text{eff}} + s^4_{13}. \tag{3.42}$$

P_{eff} can be calculated by using the effective 2×2 Hamiltonian H_{eff} written as

$$H_{\text{eff}} = \frac{\Delta m^2_{21}}{4E} \begin{pmatrix} -\cos 2\theta_{12} & \sin 2\theta_{12} \\ \sin 2\theta_{12} & \cos 2\theta_{12} \end{pmatrix} + \begin{pmatrix} c^2_{13} A & 0 \\ 0 & 0 \end{pmatrix},$$

where $A = \sqrt{2} G_F N_e$ is the matter potential. An exact form of P_{eff} is

$$P_{\text{eff}} = \frac{1}{2} + \frac{1}{2} \cos 2\theta_{12} \frac{\Delta E_{21} \cos 2\theta_{12} - A c^2_{13}}{\sqrt{(\Delta E_{21} \cos^2 2\theta_{12} - A c^2_{13})^2 + (\Delta E_{21} \sin 2\theta_{12})^2}}. \tag{3.43}$$

P_{eff} with $\theta_{13} \to 0$ is called the effective two flavor oscillation probability. The best-fit values from solar neutrino experiments are [54]

$$\begin{aligned} \sin^2\theta_{12} &= 0.308 \pm 0.014, \\ \Delta m^2_{21} &= 4.84^{+1.26}_{-0.60}. \end{aligned}$$

There is another experiment called KamLAND that measures the solar neutrino oscillation parameters Δm^2_{21} and θ_{12}. The oscillation probability measured in KamLAND is the disappearance probability of the anti-electron neutrinos emitted by the nuclear power plants

$$P(\bar{\nu}_e \to \bar{\nu}_e) = c^2_{13}\left(1 - \sin^2 2\theta_{12}\sin^2\frac{\Delta m^2_{21}L}{4E}\right). \tag{3.44}$$

Before KamLAND experiment, four solutions to the solar neutrino problem were known: (a) the Large Mixing Angle (LMA) solution, (b) the Small Mixing Angle (SMA) solution, (c) the LOW (low probability and low mass) solution, and (d) the just-so or vacuum (VAC) solution. These solutions are shown in Fig. 3.8.

As mentioned above KamLAND confirmed the LMA solution and the best-fit values from KamLand experiment are [54]

$$\begin{aligned} \sin^2\theta_{12} &= 0.316^{+0.0134}_{-0.026}, \\ \Delta m^2_{21} &= 7.54^{+0.19}_{-0.18}. \end{aligned}$$

The best-fit values form the combined solar and KamLand data are [54]

$$\begin{aligned} \sin^2\theta_{12} &= 0.308 \pm 0.012, \\ \Delta m^2_{21} &= 7.49^{+0.19}_{-0.18}. \end{aligned}$$

There is a 2σ tension between the mass-squared difference deduced from the solar neutrino observations and the one from the KamLAND experiment.

3.5.2 Neutrino Oscillation Analysis Driven by Δm^2_{31}

The neutrino oscillations driven by Δm^2_{31} are atmospheric, accelerator and reactor neutrino oscillations. The oscillation channels which are relevant to atmospheric and accelerator neutrinos are $\nu_e \leftrightarrow \nu_\mu$ and $\nu_\mu \leftrightarrow \nu_\mu$ channels. Among them the main contribution to θ_{23} determination is the $\nu_\mu \leftrightarrow \nu_\mu$ channel. The $\nu_\mu \to \nu_\mu$ oscillation

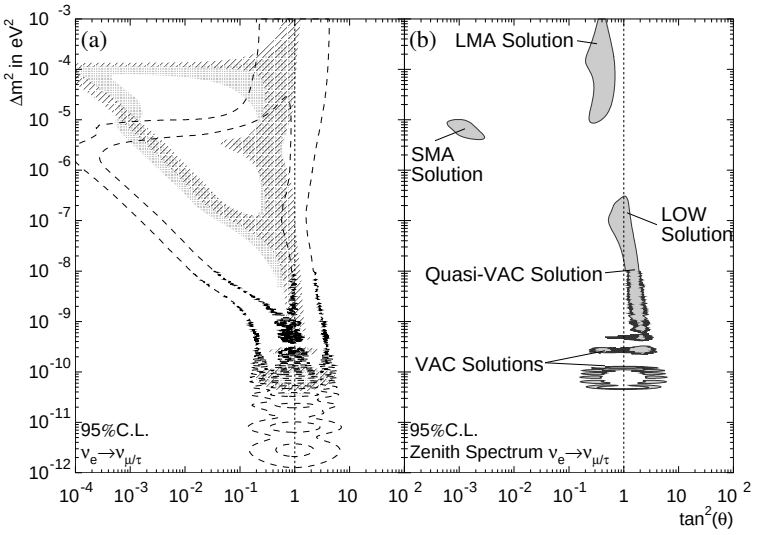

Figure 3.8: The shaded area stands for the allowed region of Homestake data, the hatched area stands for that of the SNO charged-current rate, the area in the dashed line stands for that of Gallex/GNO and SAGE [55]. All contours in this figure are 95% C.L.

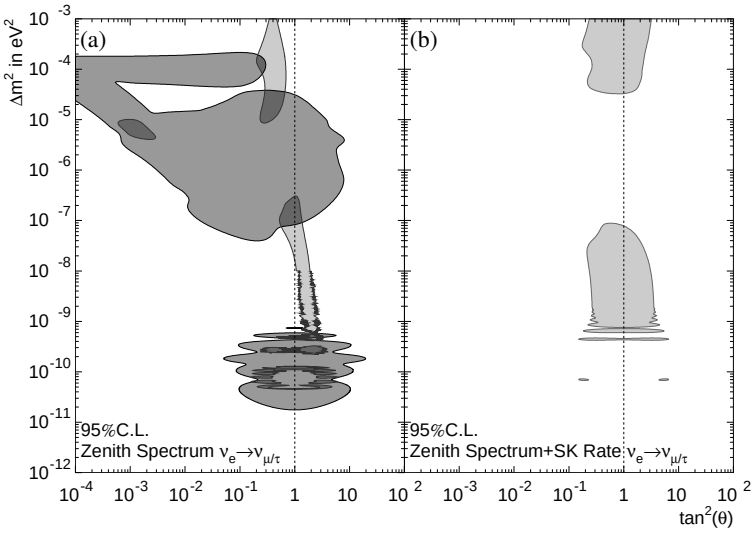

Figure 3.9: (a) The gray areas stand for excluded regions by SK data [55]. (b) The allowed region given by SK data. All contours in this figure are 95% C.L.

probability $P(\nu_\mu \to \nu_\mu)$ with $\Delta m^2_{21} \to 0$ and $\theta_{13} \to 0$ (the two flavor framework) is given as

$$1 - P(\nu_\mu \to \nu_\mu) = \sin^2 2\theta_{23} \sin^2 \left(\frac{\Delta m^2_{31} L}{4E} \right) \tag{3.45}$$

where L and E stand for a neutrino flight path length and energy, respectively. One can easily find that the oscillation probability (3.45) is unchanged by $\theta_{23} \to \pi/2 - \theta_{23}$ or $\Delta m^2_{31} \to -\Delta m^2_{31}$. These invariances cause degeneracies in the parameter determination. Currently, the neutrino oscillation parameters are extracted not only from the two flavor framework but also from the three flavor framework. The allowed regions by various experiments are shown in Fig. 3.10.

The short-baseline reactor neutrino experiments measure the electron anti-neutrino survival $P(\bar{\nu}_e \to \bar{\nu}_e)$ driven by Δm^2_{31}. The probability with $\Delta m^2_{21} \to 0$ is given as

$$1 - P(\bar{\nu}_e \to \bar{\nu}_e) = \sin^2 2\theta_{13} \sin^2 \left(\frac{\Delta m^2_{31} L}{4E} \right), \tag{3.46}$$

and depicted in Fig. 3.6.

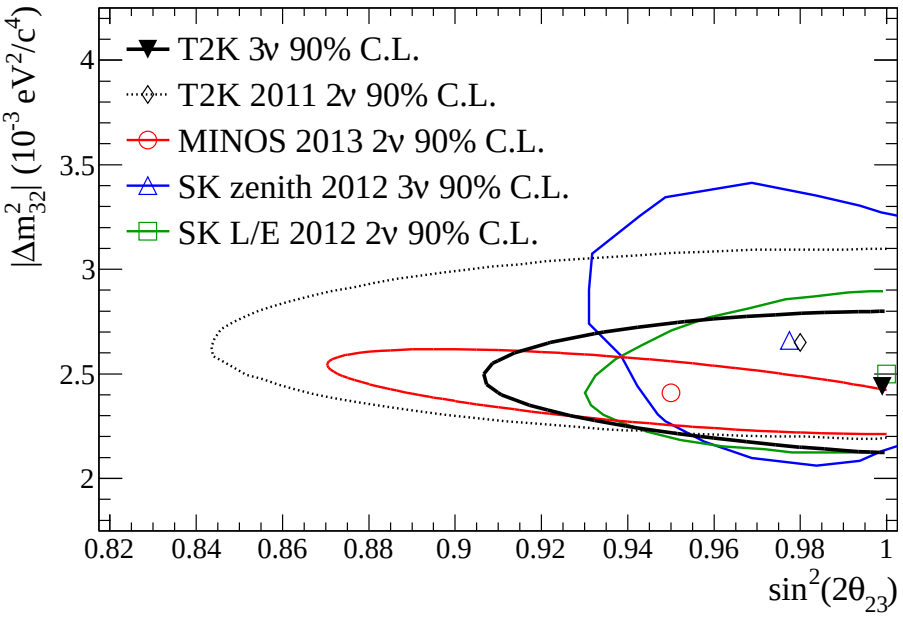

Figure 3.10: The allowed regions at 90% C.L. for $\sin^2 2\theta_{23}$ v.s. $|\Delta m^2_{32}|$ [56].

3.5.3 Global Neutrino Oscillation Analysis

Global analysis of neutrino oscillation experiments data in the three flavor framework can be found in Ref. [57]. Relations between the oscillation parameters and experiments are listed in Table 3.2 and the best-fit oscillation parameters from global data in the three flavor framework are listed in Table 3.3.

Experiment	Dominant	Important
Solar Experiments	θ_{12}	Δm^2_{21}, θ_{13}
Reactor LBL (KamLAND)	Δm^2_{21}	θ_{12}, θ_{13}
Reactor MBL (Daya-Bay, Reno, D-Chooz)	θ_{13}	$\lvert\Delta m^2_{3\ell}\rvert$
Atmospheric Experiments	θ_{23}	$\lvert\Delta m^2_{3\ell}\rvert$, θ_{13}, $\delta_{\rm CP}$
Accelerator LBL ν_μ Disapp (Minos, NOνA, T2K)	$\lvert\Delta m^2_{3\ell}\rvert$, θ_{23}	
Accelerator LBL ν_e App (Minos, NOνA, T2K)	$\delta_{\rm CP}$	θ_{13}, θ_{23}, sign$(\Delta m^2_{3\ell})$

Table 3.2: Relations between the oscillation parameters and experiments [57]. The larger mass-squared difference is denoted as $\Delta m^2_{3\ell}$ with $\ell = 1$ for the normal hierarchy and $\ell = 2$ for the inverted hierarchy.

	Normal Ordering ($\Delta\chi^2 = 0.97$)		Inverted Ordering (best-fit)		Any Ordering
	bfp $\pm1\sigma$	3σ range	bfp $\pm1\sigma$	3σ range	3σ range
$\sin^2\theta_{12}$	$0.304^{+0.013}_{-0.012}$	$0.270 \to 0.344$	$0.304^{+0.013}_{-0.012}$	$0.270 \to 0.344$	$0.270 \to 0.344$
$\theta_{12}/^\circ$	$33.48^{+0.78}_{-0.75}$	$31.29 \to 35.91$	$33.48^{+0.78}_{-0.75}$	$31.29 \to 35.91$	$31.29 \to 35.91$
$\sin^2\theta_{23}$	$0.452^{+0.052}_{-0.028}$	$0.382 \to 0.643$	$0.579^{+0.025}_{-0.037}$	$0.389 \to 0.644$	$0.385 \to 0.644$
$\theta_{23}/^\circ$	$42.3^{+3.0}_{-1.6}$	$38.2 \to 53.3$	$49.5^{+1.5}_{-2.2}$	$38.6 \to 53.3$	$38.3 \to 53.3$
$\sin^2\theta_{13}$	$0.0218^{+0.0010}_{-0.0010}$	$0.0186 \to 0.0250$	$0.0219^{+0.0011}_{-0.0010}$	$0.0188 \to 0.0251$	$0.0188 \to 0.0251$
$\theta_{13}/^\circ$	$8.50^{+0.20}_{-0.21}$	$7.85 \to 9.10$	$8.51^{+0.20}_{-0.21}$	$7.87 \to 9.11$	$7.87 \to 9.11$
$\delta_{\rm CP}/^\circ$	306^{+39}_{-70}	$0 \to 360$	254^{+63}_{-62}	$0 \to 360$	$0 \to 360$
$\frac{\Delta m^2_{21}}{10^{-5}\ \mathrm{eV}^2}$	$7.50^{+0.19}_{-0.17}$	$7.02 \to 8.09$	$7.50^{+0.19}_{-0.17}$	$7.02 \to 8.09$	$7.02 \to 8.09$
$\frac{\Delta m^2_{3\ell}}{10^{-3}\ \mathrm{eV}^2}$	$+2.457^{+0.047}_{-0.047}$	$+2.317 \to +2.607$	$-2.449^{+0.048}_{-0.047}$	$-2.590 \to -2.307$	$\begin{bmatrix}+2.325 \to +2.599\\ -2.590 \to -2.307\end{bmatrix}$

Table 3.3: The best-fit oscillation parameters from global data in the three flavor framework [57]. Normal and inverted ordering correspond to normal and inverted hierarchy, respectively. The values in the 1st (2nd) column are obtained assuming the normal (inverted) hiearachy. In the 3rd column the values are minimized with respect to the mass hierarchy. Note that $\Delta m^2_{3\ell} \equiv \Delta m^2_{31} > 0$ for NH and $\Delta m^2_{3\ell} \equiv \Delta m^2_{32} < 0$ for IH.

Chapter 4

Neutrino Nonstandard Interactions Phenomenology

So far we discussed the neutrino oscillations in the standard three flavor framework. In this section we discuss phenomenology of neutrino oscillations with flavor-dependent neutrino NonStandard Interactions (NSI) which have been studied as the new physics candidates. There are two types of NSI. One is a neutral current nonstandard interaction [1, 2, 3] and the other is a charged current nonstandard interaction [4]. The neutral current NSI affects the neutrino propagation through the matter effect and hence experiments with a long baseline such as atmospheric neutrino and LBL experiments are expected to have the sensitivity to the neutral current NSI. On the other hand, the charged current NSI causes zero distance effects in neutrino oscillation. In this thesis, we concentrate on the effects of neutral current NSI in neutrino propagation because a hint for the neutral current NSI has been suggested. It was pointed out in Ref. [58] that there is a tension between the mass-squared difference deduced from the solar neutrino observations and the one from the KamLAND experiment, and that the tension can be resolved by introducing the neutral current NSI whose strength is comparable to the SM intearctions in neutrino propagation. Such a hint for NSI gives us a strong motivation to study NSI in propagation in details.

Constraints on $\epsilon_{\alpha\beta}$ have been discussed by many people in the past [1]; from atmospheric neutrinos [61, 62, 63, 64, 65], from e^+e^- colliders [66], from the compilation of various neutrino data [67], from solar neutrinos [68, 69, 70], from $\nu_e e$ or $\bar{\nu}_e e$ scatterings [71, 72], from solar and reactor neutrinos [73], from solar, reactor and accelerator neutrinos [74]. The constraints on ϵ_{ee} and $\epsilon_{e\tau}$ from the atmospheric neutrino has been

[1] See Refs. [59, 60] for extensive references.

discussed in Ref. [75] along with those from the long-baseline experiments, in Ref. [76] by the Super-Kamiokande Collaboration, in Refs. [77, 78, 79, 80, 81] on the future atmospheric neutrino experiments, with the ansatz different from ours mentioned later.

In addition to the view of phenomenology, it should be mentioned that some models predict large non-standard interactions [82, 83, 84], and hence such large NSI effects are worth investigating also from the view point of model building.

4.1 Neutrino Oscillations with NSI

Let us start with the effective flavor-dependent neutral current neutrino nonstandard interactions in propagation given by

$$\mathcal{L}_{\rm eff}^{\rm NSI} = -2\sqrt{2}\,\epsilon_{\alpha\beta}^{ff'P} G_F \left(\overline{\nu}_{\alpha L}\gamma_\mu \nu_{\beta L}\right) \left(\overline{f}_P \gamma^\mu f'_P\right), \tag{4.1}$$

where f_P and f'_P stand for fermions with chirality P and $\epsilon_{\alpha\beta}^{ff'P}$ is a dimensionless constant which is normalized by the Fermi coupling constant G_F. The presence of NSI (4.1) modifies the MSW potential in the flavor basis:

$$\sqrt{2}G_F N_e \begin{pmatrix} 1 & 0 & 0 \\ 0 & 0 & 0 \\ 0 & 0 & 0 \end{pmatrix} \to \mathcal{A}\,, \tag{4.2}$$

where

$$\mathcal{A} \equiv \sqrt{2}G_F N_e \begin{pmatrix} 1+\epsilon_{ee} & \epsilon_{e\mu} & \epsilon_{e\tau} \\ \epsilon_{\mu e} & \epsilon_{\mu\mu} & \epsilon_{\mu\tau} \\ \epsilon_{\tau e} & \epsilon_{\tau\mu} & \epsilon_{\tau\tau} \end{pmatrix}, \tag{4.3}$$

$\epsilon_{\alpha\beta}$ is defined by

$$\epsilon_{\alpha\beta} \equiv \sum_{f=e,u,d} \frac{N_f}{N_e} \epsilon_{\alpha\beta}^f\,, \tag{4.4}$$

and N_f $(f = e, u, d)$ stands for number densities of fermions f. Here we defined the new NSI parameters as $\epsilon_{\alpha\beta}^{fP} \equiv \epsilon_{\alpha\beta}^{ffP}$ and $\epsilon_{\alpha\beta}^{f} \equiv \epsilon_{\alpha\beta}^{fL} + \epsilon_{\alpha\beta}^{fR}$ since the matter effect is sensitive only to the coherent scattering and only to the vector part in the interaction. As can be seen from the definition of $\epsilon_{\alpha\beta}$, the neutrino oscillation experiments on the Earth are sensitive only to the sum of $\epsilon_{\alpha\beta}^{f}$. We call the most general parametrization (4.3) of NSI in the flavor basis the standard NSI parametrization in this thesis. In

the three flavor neutrino oscillation framework with NSI, the neutrino evolution is governed by the Dirac equation:

$$i\frac{d}{dx}\begin{pmatrix}\nu_e(x)\\ \nu_\mu(x)\\ \nu_\tau(x)\end{pmatrix} = \left[U\,\mathrm{diag}\,(0,\Delta E_{21},\Delta E_{31})\,U^{-1}+\mathcal{A}\right]\begin{pmatrix}\nu_e(x)\\ \nu_\mu(x)\\ \nu_\tau(x)\end{pmatrix}, \tag{4.5}$$

where U is the leptonic mixing matrix defined by

$$U \equiv \begin{pmatrix} c_{12}c_{13} & s_{12}c_{13} & s_{13}e^{-i\delta_{\rm CP}} \\ -s_{12}c_{23}-c_{12}s_{23}s_{13}e^{i\delta_{\rm CP}} & c_{12}c_{23}-s_{12}s_{23}s_{13}e^{i\delta_{\rm CP}} & s_{23}c_{13} \\ s_{12}s_{23}-c_{12}c_{23}s_{13}e^{i\delta_{\rm CP}} & -c_{12}s_{23}-s_{12}c_{23}s_{13}e^{i\delta_{\rm CP}} & c_{23}c_{13}\end{pmatrix}, \tag{4.6}$$

and $\Delta E_{jk} \equiv \Delta m^2_{jk}/2E \equiv (m^2_j - m^2_k)/2E$, $c_{jk} \equiv \cos\theta_{jk}$, $s_{jk} \equiv \sin\theta_{jk}$.

4.2 Constraints on NSI from Solar Neutrinos

In Refs. [58, 85] it was pointed out that there is a tension between the two mass squared differences extracted from the KamLAND and solar neutrino experiments. The mass squared difference Δm^2_{21} ($= 4.7\times10^{-5}\mathrm{eV}^2$) extracted from the solar neutrino data is 2σ smaller than that from the KamLAND data Δm^2_{21} ($= 7.5\times10^{-5}\mathrm{eV}^2$). The authors of Refs. [58, 85] discussed the tension can be removed by introducing NSI in propagation.

To discuss the effect of NSI on solar neutrinos, we reduce the 3×3 Hamiltonian in the Dirac equation Eq. (4.5) to an effective 2×2 Hamiltonian to get the survival probability $P(\nu_e\to\nu_e)$ because solar neutrinos are approximately driven by one mass squared difference Δm^2_{21} [58]. The survival probability $P(\nu_e\to\nu_e)$ can be written as

$$P(\nu_e\to\nu_e) = c^4_{13}P_{\rm eff} + s^4_{13}, \tag{4.7}$$

where $P_{\rm eff}$ is

$$P_{\rm eff} = \frac{1}{2}\left(1+\cos2\tilde{\theta}\cos2\theta_{12}\right), \tag{4.8}$$

$$\tan2\tilde{\theta} = \frac{|\Delta m^2_{21}\sin2\theta_{12}/4E + A\sum_f \epsilon^f_N N_f/N_e|}{\Delta m^2_{21}\cos2\theta_{12}/4E - A(c^2_{13}/2 - \sum_f \epsilon^f_D N_f/N_e)}. \tag{4.9}$$

$P_{\rm eff}$ can be calculated by using the effective 2×2 Hamiltonian $H^{\rm eff}$ written as

$$H^{\rm eff} = \frac{\Delta m^2_{21}}{4E}\begin{pmatrix}-\cos2\theta_{12} & \sin2\theta_{12}\\ \sin2\theta_{12} & \cos2\theta_{12}\end{pmatrix} + \begin{pmatrix}c^2_{13}A & 0\\ 0 & 0\end{pmatrix} + A\sum_{f=e,u,d}\frac{N_f}{N_e}\begin{pmatrix}-\epsilon^f_D & \epsilon^f_N\\ \epsilon^{f*}_N & \epsilon^f_D\end{pmatrix}, \tag{4.10}$$

where ϵ^f_D and ϵ^f_N are linear combinations of the standard NSI parameters:

$$\begin{aligned}
\epsilon^f_D &= c_{13}s_{13}\mathrm{Re}\left[e^{i\delta_{\rm CP}}\left(s_{23}\epsilon^f_{e\mu}+c_{23}\epsilon^f_{e\tau}\right)\right]-\left(1+s^2_{13}\right)c_{23}s_{23}\mathrm{Re}\left[\epsilon^f_{\mu\tau}\right] \\
&\quad -\frac{c^2_{13}}{2}\left(\epsilon^f_{ee}-\epsilon^f_{\mu\mu}\right)+\frac{s^2_{23}-s^2_{13}c^2_{23}}{2}\left(\epsilon^f_{\tau\tau}-\epsilon^f_{\mu\mu}\right) \\
\epsilon^f_N &= c_{13}\left(c_{23}\epsilon^f_{e\mu}-s_{23}\epsilon^f_{e\tau}\right)+s_{13}e^{-i\delta_{\rm CP}}\left[s^2_{23}\epsilon^f_{\mu\tau}-c^2_{23}\epsilon^{f*}_{\mu\tau}+c_{23}s_{23}\left(\epsilon^f_{\tau\tau}-\epsilon^f_{\mu\mu}\right)\right].
\end{aligned} \tag{4.11}$$

Ref. [58, 85] discussed the sensitivity of solar neutrino and KamLAND experiments to ϵ^f_D and real ϵ^f_N for one particular choice of $f = u$ or $f = d$ at a time. The results are shown in Fig. 4.1. The best-fit values from the solar neutrino and KamLAND data are $(\epsilon^u_D, \epsilon^u_N) = (-0.22, -0.30)$ and $(\epsilon^d_D, \epsilon^d_N) = (-0.12, -0.16)$ and that from the global analysis of the neutrino oscillation data are $(\epsilon^u_D, \epsilon^u_N) = (-0.140, -0.030)$ and $(\epsilon^d_D, \epsilon^d_N) = (-0.145, -0.036)$. These results give us a hint for the existence of NSI.

In addition to the above, Ref. [58, 85] also discussed the possibility of the dark-side solution ($\Delta m^2_{21} > 0$ and $\theta_{12} > \pi/4$) which requires NSI in the solar neutrino problem. The dark-side solution arises from the symmetry of the Hamiltonian (4.10) and survival probability (4.7). To discuss the origin of dark-side solution, we consider ranges of the oscillation parameters. We can assume $\Delta m^2_{21} > 0$ without loss of generality because the Hamiltonian (4.10) is invariant under the transformation $(\Delta m^2_{21}, \theta_{12}) \to (-\Delta m^2_{21}, \theta_{12} + \pi/2)$. Next, we can restrict θ_{12} range to $-\pi/2 \le \theta_{12} \le \pi/2$ because its dependence appears $2\theta_{12}$ in survival probability (4.7). The probability has no sensitivity to the overall sign of the non-diagonal component of the Hamiltonian (4.10) and hence there is the symmetry $(\theta_{12}, \epsilon^f_N) \to (-\theta_{12}, -\epsilon^f_N)$ in the probability. Taking all symmetries into account, the ranges of the oscillation parameters which we have to consider are $\Delta m^2_{21} > 0$ and $0 \le \theta_{12} \le \pi/2$. Let us consider the transformations

$$\begin{aligned}
\Delta m^2_{21} &\to -\Delta m^2_{21}, \\
\epsilon^f_N &\to -\epsilon^f_N, \\
c^2_{13}/2 - \sum_f \epsilon^f_D N_f/N_e &\to -\left(c^2_{13}/2 - \sum_f \epsilon^f_D N_f/N_e\right).
\end{aligned}$$

Under the transformations the oscillation probability is unchanged and the transformations Δm^2_{21} and ϵ^f_N can be absorbed into that of θ_{12}. That is why the dark-side solution ($\theta_{12} > \pi/4$) is confused with the standard LAM solutions ($\theta_{12} < \pi/4$). The allowed regions for the dark-side solution are disconnected from that for the standard LMA solution in the plane $(\epsilon^f_D, \epsilon^f_N)$ and those for the dark-side solution within 3σ do not contain the standard scenario $\epsilon^f_D = \epsilon^f_N = 0$.

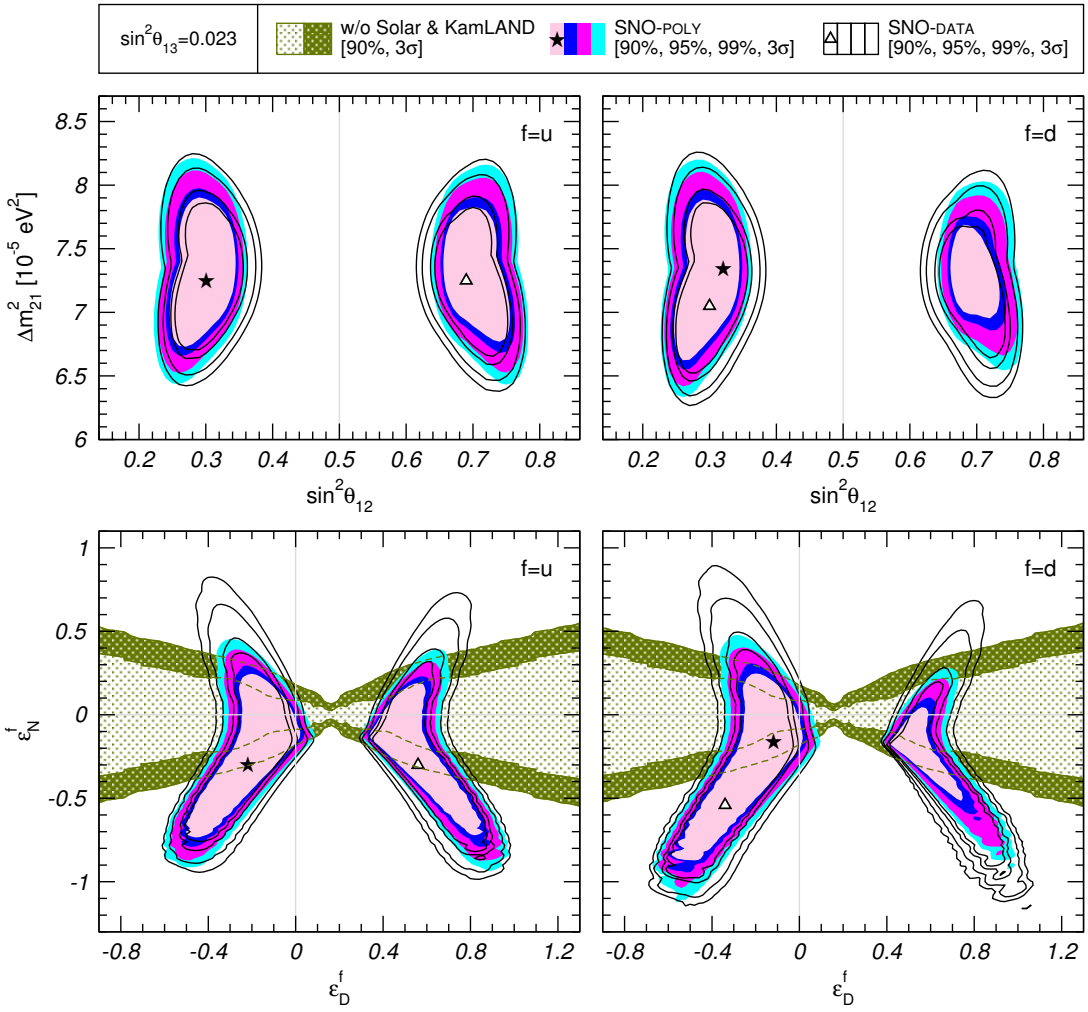

Figure 4.1: The allowed regions in the $(\epsilon^f_D, \epsilon^f_N)$ plane [58]. The SNO results are included in two different forms. The allowed regions given by the SNO results of low energy threshold analysis are labeled as SNO-POLY and those given by the other results of SNO are labeled as SNO-DATA. The best-fit point given by SNO-DATA (SNO-POLY) is marked with a star (triangle). The green dotted regions are given by the analysis of the atmospheric and LBL data.

4.3 Constraints on NSI from Atmospheric Neutrinos

In this section, we describe the constraints on NSI from the atmospheric neutrino experiments and introduce a relation between ϵ_{ee}, $|\epsilon_{e\tau}|$ and $\epsilon_{\tau\tau}$ and the matter angle β. Atmospheric neutrinos go through the Earth and interact with electrons, up and down quarks. In the Earth, the number densities of electrons, protons and neutrons are approximately equal and hence those of up quarks and down quarks are approximately the same. From these, one can define $\epsilon_{\alpha\beta}$ as

$$\epsilon_{\alpha\beta} = \epsilon^e_{\alpha\beta} + 3\epsilon^u_{\alpha\beta} + 3\epsilon^d_{\alpha\beta}, \tag{4.12}$$

and we have the following limits [67, 86] on $\epsilon_{\alpha\beta}$ at 90% C.L.:

$$\begin{pmatrix} |\epsilon_{ee}| < 4 \times 10^0 & |\epsilon_{e\mu}| < 3 \times 10^{-1} & |\epsilon_{e\tau}| < 3 \times 10^0 \\ & |\epsilon_{\mu\mu}| < 7 \times 10^{-2} & |\epsilon_{\mu\tau}| < 3 \times 10^{-1} \\ & & |\epsilon_{\tau\tau}| < 2 \times 10^1 \end{pmatrix}. \tag{4.13}$$

To investigate the sensitivity of the atmospheric neutrino experiment to ϵ^f_D and ϵ^f_N, we have to convert ϵ^f_D and ϵ^f_N into $\epsilon^f_{\alpha\beta}$ because ϵ^f_D and ϵ^f_N are valid only in the

solar neutrinos analysis. ϵ^f_D and ϵ^f_N are expressed in terms of $\epsilon^f_{\alpha\beta}$ as the following:

$$
\begin{aligned}
|\epsilon^f_{e\tau}| &= \frac{\sin\left(\phi^f_{\mu\tau}\right) t_{13}}{\sin\left(\delta_{cp}+\phi^f_{e\tau}\right) s_{23}}|\epsilon^f_{\mu\tau}| + \frac{\sin\left(\delta_{cp}+\phi^f_{e\mu}\right)}{t_{23}\sin\left(\delta_{cp}+\phi^f_{e\tau}\right)}|\epsilon^f_{e\mu}| \\
&\quad - \frac{\sin\left(\delta_{cp}+\psi^f\right)}{\sin\left(\delta_{cp}+\phi^f_{e\tau}\right) s_{23}c_{13}}|\epsilon^f_N|, \\
\epsilon^f_{\tau\tau} - \epsilon^f_{\mu\mu} &= 2\left\{\frac{\cos\phi^f_{\mu\tau}}{\tan 2\theta_{23}} + \frac{\sin\phi^f_{\mu\tau}}{\tan\left(\delta_{cp}+\phi^f_{e\tau}\right)\sin 2\theta_{23}}\right\}|\epsilon^f_{\mu\tau}| \\
&\quad + \frac{\sin\left(\phi^f_{e\mu}-\phi^f_{e\tau}\right)}{s_{23}t_{13}\sin\left(\delta_{cp}+\phi^f_{e\tau}\right)}|\epsilon^f_{e\mu}| - \frac{2\sin(\psi^f-\phi^f_{e\tau})}{\sin(\delta_{cp}+\phi^f_{e\tau})s_{13}\sin 2\theta_{23}}|\epsilon^f_N|, \\
\epsilon^f_{ee} - \epsilon^f_{\mu\mu} &= 2\left[\frac{s^2_{23}-s^2_{13}c^2_{23}}{c^2_{13}}\left\{\frac{\cos\phi^f_{\mu\tau}}{\tan 2\theta_{23}} + \frac{\sin\phi^f_{\mu\tau}}{\tan\left(\delta_{cp}+\phi^f_{e\tau}\right)\sin 2\theta_{23}}\right\}\right. \\
&\quad \left. + \frac{t^2_{13}}{t_{23}}\cdot\frac{\sin\phi^f_{\mu\tau}}{\tan\left(\delta_{cp}+\phi^f_{e\tau}\right)} - \frac{1+s^2_{13}}{2c^2_{13}}\sin 2\theta_{23}\cos\phi_{\mu\tau}\right]|\epsilon^f_{\mu\tau}| \\
&\quad + 2\left[\frac{s^2_{23}-s^2_{13}c^2_{23}}{s_{23}\sin 2\theta_{13}}\cdot\frac{\sin\left(\phi^f_{e\mu}-\phi^f_{e\tau}\right)}{\sin\left(\delta_{cp}+\phi^f_{e\tau}\right)} + t_{13}s_{23}\cos\left(\delta_{cp}+\phi^f_{e\mu}\right)\right. \\
&\quad \left. + \frac{t_{13}c_{23}}{t_{23}}\cdot\frac{\sin(\delta_{cp}+\phi^f_{e\mu})}{\tan\left(\delta_{cp}+\phi^f_{e\tau}\right)\sin 2\theta_{23}}\right]|\epsilon^f_{e\mu}| \\
&\quad - 2\left[\frac{s^2_{23}-s^2_{13}c^2_{23}}{s_{13}c^2_{13}\sin 2\theta_{23}}\cdot\frac{\sin\left(\psi^f-\phi^f_{e\tau}\right)}{\sin\left(\delta_{cp}+\phi^f_{e\tau}\right)}\right. \\
&\quad \left. + \frac{t_{13}}{t_{23}c_{13}}\cdot\frac{\sin(\delta_{cp}+\psi^f)}{\tan\left(\delta_{cp}+\phi^f_{e\tau}\right)}\right]|\epsilon^f_N| - \frac{2}{c^2_{13}}\epsilon^f_D\,,
\end{aligned}
\tag{4.14}
$$

where $\psi^f = \arg(\epsilon^f_N)$, $\phi^f_{\alpha\beta} = \arg(\epsilon^f_{\alpha\beta})$ and $t_{ij} \equiv \tan\theta_{ij}$. When we consider only one particular choice of $f = u$ or $f = d$ at a time as in Ref. [58], from the definition of $\epsilon_{\alpha\beta}$ (4.12), we cannot distinguish the case of $f = u$ from that of $f = d$ in the atmospheric

neutrinos analysis. Therefore we concentrate on only one particular choice of $f = d$ in this thesis and then we have

$$\begin{aligned}
\epsilon_{\alpha\beta} &= 3\epsilon^d_{\alpha\beta} \\
\phi_{\alpha\beta} &\equiv \arg\left(\epsilon_{\alpha\beta}\right) = \arg\left(\epsilon^d_{\alpha\beta}\right) \\
\epsilon_D &= \epsilon^d_D \\
\epsilon_N &= \epsilon^d_N \\
\psi &\equiv \arg\left(\epsilon^d_N\right) .
\end{aligned} \tag{4.15}$$

The case with $\epsilon_{\alpha\mu} = 0$ $(\alpha = e, \mu, \tau)$

It was pointed out in Refs. [87, 88] that if the μ components of $\epsilon_{\alpha\beta}$ are set to zero then the high-energy atmospheric neutrino data, where the matter effects are dominant, are consistent with NSI only when the following inequality is hold:

$$\min_{\pm}\left(\left|1 + \epsilon_{ee} + \epsilon_{\tau\tau} \pm \sqrt{(1 + \epsilon_{ee} - \epsilon_{\tau\tau})^2 + 4|\epsilon_{e\tau}|^2}\right|\right) \lesssim 0.4 , \tag{4.16}$$

where the arguments of the absolute value on the left hand side are the two nonzero eigenvalues of the matrix $\mathcal{A}$ in the absence of $\epsilon_{\alpha\mu}$ $(\alpha = e, \mu, \tau)$ component, and the $+$ $(-)$ sign in $\pm$ is chosen when $1 + \epsilon_{ee} + \epsilon_{\tau\tau}$ is negative (positive). To understand the meaning of inequality (4.16), we compare the behavior of high-energy atmospheric neutrino oscillation probability in the standard scenario with that in the NSI scenario. In the standard scenario, the disappearance oscillation probability of the high-energy atmospheric neutrinos in the limit of $\Delta m^2_{21} \to 0$ are expressed as follows:

$$\begin{aligned}
1 - P(\nu_\mu \to \nu_\mu) &= 4\sum_{j<k}[\tilde{X}^{\mu\mu}_j \tilde{X}^{\mu\mu}_k] \sin^2\left(\frac{\left(\tilde{E}_j - \tilde{E}_k\right) L}{2}\right) \\
&\simeq 4\left(\tilde{X}^{\mu\mu}_1 \tilde{X}^{\mu\mu}_2 \sin^2\left(\frac{\Delta E_{31} c^2_{13} L}{2}\right) + \left(\tilde{X}^{\mu\mu}_1 + \tilde{X}^{\mu\mu}_2\right) \tilde{X}^{\mu\mu}_3 \sin^2\left(\frac{AL}{2}\right)\right) \\
&\simeq 4\left(\frac{X^{\mu\mu}_3}{c^2_{13}}\left(1 - \frac{X^{\mu\mu}_3}{c^2_{13}}\right)\left(\frac{\Delta E_{31} c^2_{13} L}{2}\right)^2 + \left(\frac{\Delta E_{31}}{A}\right)^2 X^{\mu\mu}_3 s^2_{13} \sin^2\left(\frac{AL}{2}\right)\right)
\end{aligned}$$

where

$$
\begin{aligned}
X_3^{\mu\mu} &\equiv U_{\mu 3} U_{\mu 3}^*, \\
\tilde{X}_1^{\mu\mu} &\simeq \frac{X_3^{\mu\mu}}{c_{13}^2}, \\
\tilde{X}_2^{\mu\mu} &\simeq 1 - \frac{X_3^{\mu\mu}}{c_{13}^2}, \\
\tilde{X}_3^{\mu\mu} &\simeq \left(\frac{\Delta E_{31}}{A}\right)^2 X_3^{\mu\mu} s_{13}^2, \\
\tilde{E}_1 &\simeq \frac{\Delta E_{31} + A - \sqrt{(\Delta E_{31}\cos 2\theta_{13} - A)^2 + (\Delta E_{31}\sin 2\theta_{13})^2}}{2}, \\
\tilde{E}_2 &\simeq 0, \\
\tilde{E}_3 &\simeq \frac{\Delta E_{31} + A + \sqrt{(\Delta E_{31}\cos 2\theta_{13} - A)^2 + (\Delta E_{31}\sin 2\theta_{13})^2}}{2}.
\end{aligned}
$$

The most important behavior of the disappearance oscillation probability is the energy dependence:

$$1 - P(\nu_\mu \to \nu_\mu) \propto E^{-2}. \tag{4.17}$$

To obtain the disappearance oscillation probability with NSI, we diagonalize the matter potential:

$$\mathcal{A} = \sqrt{2} G_F N_e \begin{pmatrix} 1+\epsilon_{ee} & 0 & \epsilon_{e\tau} \\ 0 & 0 & 0 \\ \epsilon_{\tau e} & 0 & \epsilon_{\tau\tau} \end{pmatrix} = \mathcal{O}\mathrm{diag}\left(\lambda_{e'}, 0, \lambda_{\tau'}\right)\mathcal{O}^\dagger, \tag{4.18}$$

where

$$
\begin{aligned}
\mathcal{O} &= \begin{pmatrix} \cos\beta & 0 & -e^{i\phi_{e\tau}}\sin\beta \\ 0 & 1 & 0 \\ e^{-i\phi_{e\tau}}\sin\beta & 0 & \cos\beta \end{pmatrix}, \\
\lambda_{e'} &= \sqrt{2} G_F N_e \left(\frac{1+\epsilon_{ee}+\epsilon_{\tau\tau}}{2} + \sqrt{\left(\frac{1+\epsilon_{ee}-\epsilon_{\tau\tau}}{2}\right)^2 + |\epsilon_{e\tau}|^2} \right), \\
\lambda_{\tau'} &= \sqrt{2} G_F N_e \left(\frac{1+\epsilon_{ee}+\epsilon_{\tau\tau}}{2} - \sqrt{\left(\frac{1+\epsilon_{ee}-\epsilon_{\tau\tau}}{2}\right)^2 + |\epsilon_{e\tau}|^2} \right), \\
\tan 2\beta &\equiv \frac{2|\epsilon_{e\tau}|}{1+\epsilon_{ee}-\epsilon_{\tau\tau}}.
\end{aligned}
$$

The Dirac eq. in the basis where the matter potential is diagonal is

$$i\frac{d}{dx}\begin{pmatrix}\nu'_e\\ \nu_\mu\\ \nu'_\tau\end{pmatrix} = \left[U'\mathrm{diag}\left(0,\Delta E_{21},\Delta E_{31}\right)U'^{-1} + \mathrm{diag}\left(\lambda_{e'},0,\lambda_{\tau'}\right)\right]\begin{pmatrix}\nu'_e\\ \nu_\mu\\ \nu'_\tau\end{pmatrix}$$

where

$$\begin{aligned} U' &\equiv \mathcal{O}^\dagger U, \\ \begin{pmatrix}\nu'_e\\ \nu_\mu\\ \nu'_\tau\end{pmatrix} &\equiv \mathcal{O}^\dagger \begin{pmatrix}\nu_e\\ \nu_\mu\\ \nu_\tau\end{pmatrix}. \end{aligned} \tag{4.19}$$

If we assume the condition $|\lambda_{\tau'}| \ll \Delta E_{31}$, the Dirac eq. in the diagonal matter potential basis is similar to standard one. The disappearance oscillation probability with NSI $P(\nu_\mu \to \nu_\mu)_{\mathrm{NSI}}$ can be obtained by the replacements $U \to U'$ and $A \to \lambda_{e'}$ and we require that the following condition should be satisfied:

$$1 - P(\nu_\mu \to \nu_\mu)_{\mathrm{NSI}} \propto E^{-2}.$$

If we do not assume the condition $|\lambda_{\tau'}| \ll \Delta E_{31}$, the disappearance oscillation probability with NSI not proportional to E^{-2}. The mismatch of energy dependence constrains NSI strongly and hence Eq. (4.16) plays an important role.

Notice that in the limit of $\lambda_{\tau'} = 0$, $\epsilon_{\tau\tau}$ and $|\epsilon_{e\tau}|$ satisfy a parabolic relation

$$\epsilon_{\tau\tau} = \frac{|\epsilon_{e\tau}|^2}{1+\epsilon_{ee}} \tag{4.20}$$

and hence $\epsilon_{\tau\tau}$ can be eliminated. We see in Fig 4.4 that the relation can be satisfied by the data to a good approximation. In the limit of Eq. (4.20), the disappearance oscillation probability of the high-energy atmospheric neutrinos can be reduced to $\nu_\mu \leftrightarrow \nu'_\tau$ vacuum oscillation like two-flavor form (ν'_τ is a mixture of ν_e and ν_μ due to the presence of NSI) in spite of nonvanishing $\tau\tau$ component in the matter potential. This means that the disappearance oscillation probability with NSI of the high-energy atmospheric neutrinos is proportional to E^{-2}

$$1 - P(\nu_\mu \to \nu_\mu) = \sin^2 2\theta_{\mathrm{atm}} \sin^2\left(\frac{\Delta m^2_{\mathrm{atm}} L}{4E}\right) \propto \frac{1}{E^2} \tag{4.21}$$

as in the case of the standard two flavor neutrino oscillation framework.

We have plotted a distribution of ϵ_{ee} and $|\epsilon_{e\tau}|$ for a given set (ϵ_D, ϵ_N) in Fig. 4.2. The red crosses are solutions of Eq. (4.14) and blue squares are special solutions that satisfy the constraint (4.16) from the high-energy atmospheric neutrino oscillation data. The one particular parameter set (ϵ_D, ϵ_N) gives the several parameter sets $(\epsilon_{ee}, |\epsilon_{e\tau}|)$ due to variation of oscillation and NSI parameters. This is why we should consider the non-trivial mapping between $\epsilon_{\alpha\beta}$ and $\epsilon_{D,N}$.

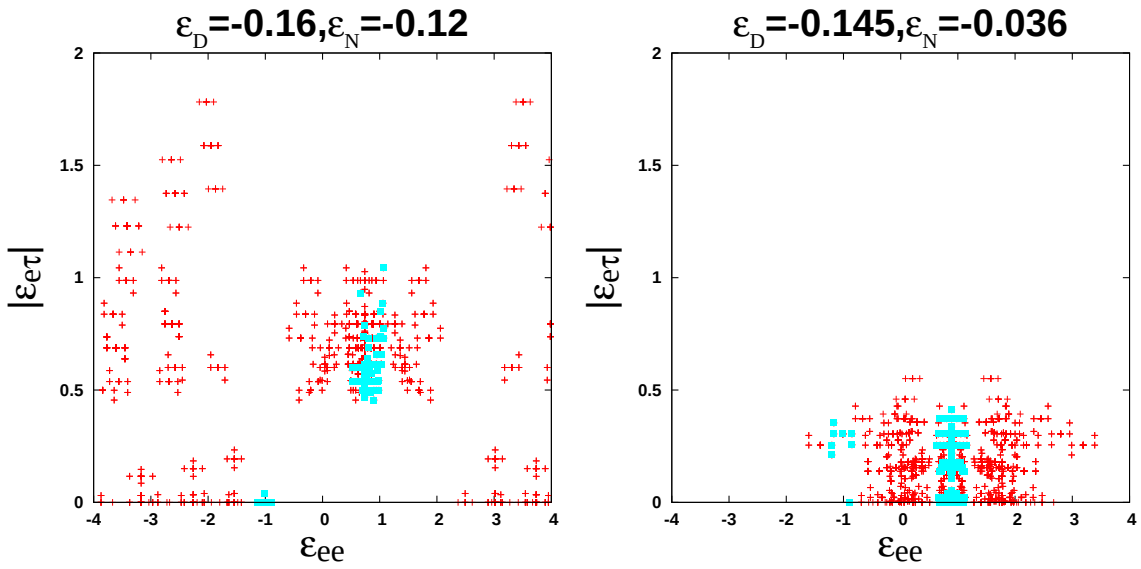

Figure 4.2: A distribution of ϵ_{ee} and $|\epsilon_{e\tau}|$ for a given set (ϵ_D, ϵ_N). Red crosses are solutions of Eq. (4.14) and blue squares are special solutions which satisfy the inequality (4.16).

Next let us discuss the matter angle β introduced in the diagonalization of matter potential [87, 88]. The matter angle β determines the mixing between the standard flavor basis $\nu_{e,\tau}$ defined by the W-boson exchange interaction and the modified flavor basis $\nu'_{e,\tau}$ due to the presence of NSI with components $\epsilon_{\alpha\beta}$ $(\alpha, \beta = e, \tau)$. As we have seen above, it is convenient to take the modified flavor basis in the discussion on the sensitivity of atmospheric neutrino experiments to NSI. We assume the case $\lambda_{\tau'} = 0$, for simplicity, and then $\tan\beta$ can be written as

$$\tan\beta = \frac{|\epsilon_{e\tau}|}{1 + \epsilon_{ee}}.$$

Using this quantity, the disappearance probability of high-energy atmospheric neu-

trinos in the limit of $\Delta m^2_{21} \to 0$ can be obtained by the changes in Eq. (4.17):

$$\begin{aligned} U &\to U' = \begin{pmatrix} \cos\beta & 0 & e^{i\phi_{e\tau}}\sin\beta \\ 0 & 1 & 0 \\ -e^{-i\phi_{e\tau}}\sin\beta & 0 & \cos\beta \end{pmatrix} U \\ A &\to \sqrt{2}G_F N_e \left(1+\epsilon_{ee}\right)\left(1+\tan^2\beta\right). \end{aligned}$$

The disappearance probability of high-energy atmospheric neutrinos depends on $\arg(\epsilon_{e\tau}) = \phi_{e\tau}$, ϵ_{ee} and $\tan\beta$. The high-energy atmospheric neutrino oscillation experiments data have less sensitivity to ee component of the matter potential because the observation can be well explained by vacuum two flavor neutrino oscillation. The sensitivity of atmospheric neutrino oscillation experiments to NSI is given after marginalizing over $\phi_{e\tau}$ and therefore atmospheric neutrino oscillation experiments constrain $\tan\beta$. In Ref. [89], the constraint $|\tan\beta| \lesssim 0.8$ (at 2.5σ) from the SK data for 4438 days is given.

It is instructive to discuss the relation between the standard parametrization $\epsilon_{\alpha\beta}$ and the set of the parametrizations $(\epsilon^f_D,\, \epsilon^f_N)$ in the simplest case. In the simplest case, we assume the parabolic relation (4.20) and set $\theta_{13} = 0$, $\theta_{23} = \pi/4$, which is a good approximation to some extent. Then, introducing a new angle

$$\tan\beta' \equiv \frac{\tan\beta}{\sqrt{2}}\,, \tag{4.22}$$

we can derive the following relation (See Appendix A.1 for the derivation and the expression for a more general case.):

$$\frac{|3\epsilon_N|}{1/2 - 3\epsilon_D} = \tan 2\beta'\,. \tag{4.23}$$

The region $|\epsilon_{e\tau}|/|1+\epsilon_{ee}| < \tan\beta$, which is the area surrounded by the $\epsilon_{e\tau} = 0$ axis and the straight line $|\epsilon_{e\tau}| = \tan\beta\,|1+\epsilon_{ee}|$ with the gradient $\tan\beta$ and the x-intercept $\epsilon_{ee} = -1$, is the allowed region in the $(\epsilon_{ee},\, |\epsilon_{e\tau}|)$ plane by the atmospheric neutrino data under the assumption of the parabolic relation (4.20). The corresponding region in the $(\epsilon_D,\, \epsilon_N)$ plane is approximately given by the one surrounded by the $\epsilon_N = 0$ axis and the straight line $|\epsilon_N| = \tan 2\beta'\,|1/6 - \epsilon_D|$ with the gradient $\tan 2\beta'$ and the x-intercept $\epsilon_D = 1/6$. The correspondence between $\tan\beta$ and $\tan 2\beta'$ can be seen in Fig 4.3.

The case with $\epsilon_{\alpha\mu} \neq 0$ $(\alpha = e, \mu, \tau)$

From here we take into consideration all the components of $\epsilon_{\alpha\beta}$ including the μ components, and lift the parabolic relation (4.20). Even in this case, because of the

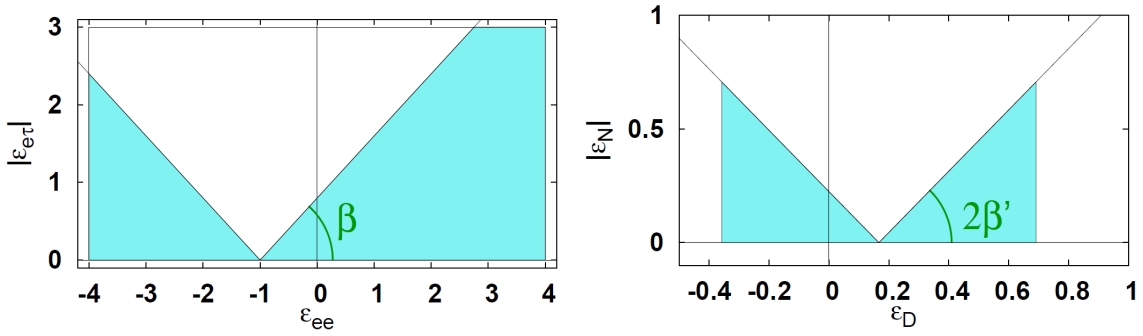

Figure 4.3: The allowed regions given by $\tan\beta$ and $\tan 2\beta'$.

strong constraints (4.13) on the $\epsilon_{\alpha\mu}$ components, the three eigenvalues of the matter potential matrix $\mathcal{A}$ are approximately 0 and $1+\epsilon_{ee}+\epsilon_{\tau\tau}\pm\sqrt{(1+\epsilon_{ee}-\epsilon_{\tau\tau})^2+4|\epsilon_{e\tau}|^2}$. So most of the discussions in the previous subsection are approximately valid. In particular, the constraint from the high energy data of the atmospheric neutrinos can be approximately given by Eq. (4.16). We note that another derivation of the relation (4.20) was given in Ref. [90].[2] The high-energy behavior of the disappearance oscillation probability in the presence of NSI without switching off any $\epsilon_{\alpha\beta}$ can be written as

$$1 - P(\nu_\mu \to \nu_\mu) \simeq c_0 + c_1 \frac{\sqrt{2} G_F N_e}{E} + \mathcal{O}\left(\frac{1}{E^2}\right). \tag{4.24}$$

This expression requires $|c_0| \ll 1$ and $|c_1| \ll 1$ so that the presence of NSI is consistent with the high-energy atmospheric neutrino experiments data. The constraints on c_0 and c_1 imply $\epsilon_{e\mu} \simeq \epsilon_{\mu\mu} \simeq \epsilon_{\tau\mu} \simeq 0$ and $\epsilon_{\tau\tau} \simeq |\epsilon_{e\tau}|^2/(1+\epsilon_{ee})$.

[2]The oscillation probability in the presence of NSI was given in the low energy region in Ref. [91].

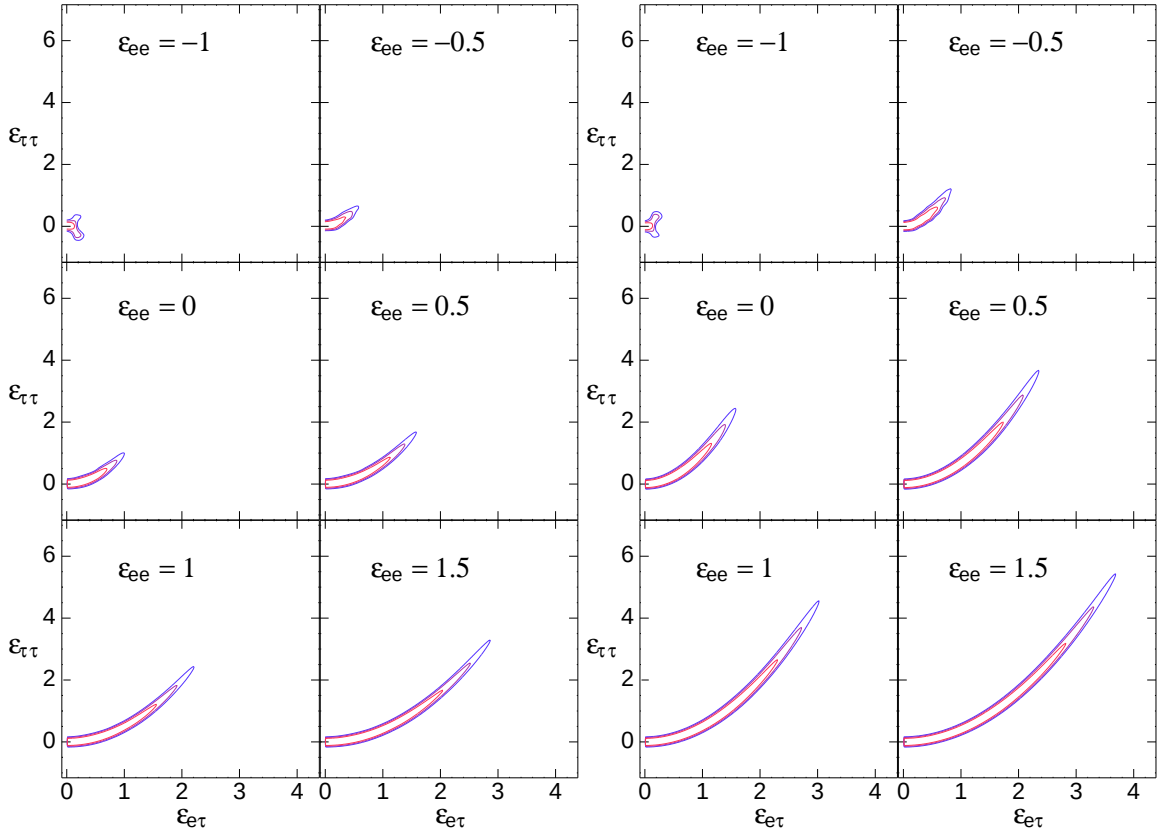

Figure 4.4: The allowed regions for normal (left) and inverted (right) hierarchy from a combined fit of the atmospheric and K2K data [88]. In this analysis the oscillation parameters θ_{13} and Δm^2_{21} are set to zero. The contours, from the inner to the outer, correspond to 95%, 99% and 3 σ C.L.

Chapter 5

Sensitivity of Atmospheric Neutrino Experiments to NSI

In this chapter the sensitivity of the future atmospheric neutrino experiment HK to NSI is studied assuming that the mass hierarchy is known. The analysis was performed with the codes which were used in Ref. [92, 93, 94, 89, 95]. There are two NSI parametrizations currently known. We discuss the sensitivity to NSI parameterized as $\epsilon_{\alpha\beta}$ and $\epsilon_{D,N}$ in HK.

5.1 Sensitivity of Hyper-Kamiokande

In this section we discuss the sensitivity to NSI of the Hyper-Kamiokande (HK) atmospheric neutrino experiment whose data is assumed to be taken for 4438 days. In our analysis of the sensitivity to NSI, we assume that the mass hierarchy is known because there may be some hints on the mass hierarchy determination by the time HK accumulate the data for 4438 days. We consider two cases, one of which is the case assuming that $\epsilon_{\alpha\mu} = 0$ ($\alpha = e, \mu\tau$) and $\epsilon_{\tau\tau} = |\epsilon_{e\tau}|^2/(1+\epsilon_{ee})$, and the other is the case without these assumptions.

We assume that the HK fiducial volume is 0.56 Mton [1], and that the HK detector has the same detection efficiencies as those of Super-Kamiokande (SK) and that HK atmospheric neutrino data consist of the sub-GeV, multi-GeV and upward going

[1]Recently there is a new design with the reduced fiducial volume (two tanks with the fiducial volume 0.19 Mton each). However, decreasing of the number of events due to a reduced fiducial volume can be compensated by the improvement of the detection efficiencies. Since the details of the new design are not known, we will analyze the atmospheric neutrino measurements at Hyperkamiokande with the parameters in the old design throughout this thesis.

μ events as in the case of SK. As HK is the future experiment, the number of events calculated with the standard three flavor oscillation scenario are used as the experimental data for fitting. The reference values of oscillation parameters used in the calculation of the experimental data are the following:

$$\begin{aligned} \Delta\bar{m}^2_{31} = 2.5\times10^{-3}\mathrm{eV}^2, \sin^2\bar{\theta}_{23} = 0.5, \bar{\delta}_{\mathrm{CP}} = 0, \\ \sin^2 2\bar{\theta}_{12} = 0.86, \sin^2 2\bar{\theta}_{13} = 0.1, \Delta\bar{m}^2_{21} = 7.6\times10^{-5}\mathrm{eV}^2\,, \end{aligned} \tag{5.1}$$

where the parameters with a bar denote those for the reference value of "the experimental data". The information on the zenith angle bins for the sub-GeV, multi-GeV and upward going μ events are given in Ref. [96] while that on the energy bins is not available. We analyze with the ten zenith angle bins as in Ref. [96]. As the experimental data is calculated by our codes, we can use any information on the energy spectrum of the number of events and analyze with any number of the energy bins.

Before moving on to the discussions on the sensitivity of HK to NSI, we investigate the significance of the wrong mass hierarchy to check the validity of our codes. We calculated the significance of the wrong mass hierarchy with different numbers of the energy bins and found that the significance calculated by our codes with two energy bins in the contained events and one energy bin in the upward going μ events is similar to the one in Ref. [34]. The more we increase the energy bins, the larger significance of the wrong mass hierarchy becomes as long as the width of each energy bin is larger than the uncertainty due to the energy resolution. In the case of the analysis of the sensitivity to NSI, the allowed regions with more than two energy bins are smaller than those with two energy bins. In this thesis, therefore, we adopt two energy bins in the contained events and one energy bin in the upward going μ events so that the results are conservative. Notice that in the case with $\epsilon_{\alpha\mu} = 0$ ($\alpha = e, \mu, \tau$) and $\epsilon_{\tau\tau} = |\epsilon_{e\tau}|^2/(1+\epsilon_{ee})$, the energy rate (one energy bin) analysis of the sensitivity of HK to NSI is also given.

In the HK rate analysis χ^2 is defined as

$$\chi^2 = \min_{\theta_{23},|\Delta m^2_{32}|,\delta,\arg(\epsilon_{e\tau})} \left(\chi^2_{\mathrm{sub-GeV}} + \chi^2_{\mathrm{multi-GeV}} + \chi^2_{\mathrm{upward}}\right), \tag{5.2}$$

where

$$\chi^2_{\text{sub-GeV}} = \min_{\alpha_s,\beta' s}\left[\frac{\beta_{s1}^2}{\sigma_{\beta s1}^2}+\frac{\beta_{s2}^2}{\sigma_{\beta s2}^2}+\sum_{j=1}^{10}\left\{\frac{1}{n_j^s(e)}\left[\alpha_s\left(1-\frac{\beta_{s1}}{2}+\frac{\beta_{s2}}{2}\right)N_j^s(\nu_e\to\nu_e)\right.\right.\right.$$
$$+\alpha_s\left(1+\frac{\beta_{s1}}{2}+\frac{\beta_{s2}}{2}\right)N_j^s(\nu_\mu\to\nu_e)$$
$$+\alpha_s\left(1-\frac{\beta_{s1}}{2}-\frac{\beta_{s2}}{2}\right)N_j^s(\bar\nu_e\to\bar\nu_e)$$
$$\left.+\alpha_s\left(1+\frac{\beta_{s1}}{2}-\frac{\beta_{s2}}{2}\right)N_j^s(\bar\nu_\mu\to\bar\nu_e)-n_j^s(e)\right]^2$$
$$+\frac{1}{n_j^s(\mu)}\left[\alpha_s\left(1-\frac{\beta_{s1}}{2}+\frac{\beta_{s2}}{2}\right)N_j^s(\nu_e\to\nu_\mu)\right.$$
$$+\alpha_s\left(1+\frac{\beta_{s1}}{2}+\frac{\beta_{s2}}{2}\right)N_j^s(\nu_\mu\to\nu_\mu)$$
$$+\alpha_s\left(1-\frac{\beta_{s1}}{2}-\frac{\beta_{s2}}{2}\right)N_j^s(\bar\nu_e\to\bar\nu_\mu)$$
$$\left.\left.\left.+\alpha_s\left(1+\frac{\beta_{s1}}{2}-\frac{\beta_{s2}}{2}\right)N_j^s(\bar\nu_\mu\to\bar\nu_\mu)-n_j^s(\mu)\right]^2\right\}\right], \qquad (5.3)$$

$$
\begin{aligned}
\chi^2_{\rm multi-GeV} \;=\; \min_{\alpha_m,\beta' s} \Bigg[& \frac{\beta_{m1}^2}{\sigma_{\beta m1}^2} + \frac{\beta_{m2}^2}{\sigma_{\beta m2}^2} + \sum_{j=1}^{10} \Bigg\{ \frac{1}{n_j^m(e)} \Bigg[\alpha_s \left(1 - \frac{\beta_{m1}}{2} + \frac{\beta_{m2}}{2} \right) N_j^m(\nu_e \to \nu_e) \\
& + \alpha_s \left(1 + \frac{\beta_{m1}}{2} + \frac{\beta_{m2}}{2} \right) N_j^m(\nu_\mu \to \nu_e) \\
& + \alpha_s \left(1 - \frac{\beta_{m1}}{2} - \frac{\beta_{m2}}{2} \right) N_j^m(\bar\nu_e \to \bar\nu_e) \\
& + \alpha_s \left(1 + \frac{\beta_{m1}}{2} - \frac{\beta_{m2}}{2} \right) N_j^m(\bar\nu_\mu \to \bar\nu_e) - n_j^m(e) \Bigg]^2 \\
& + \frac{1}{n_j^m(\mu)} \Bigg[\alpha_s \left(1 - \frac{\beta_{m1}}{2} + \frac{\beta_{m2}}{2} \right) N_j^m(\nu_e \to \nu_\mu) \\
& + \alpha_s \left(1 + \frac{\beta_{m1}}{2} + \frac{\beta_{m2}}{2} \right) N_j^m(\nu_\mu \to \nu_\mu) \\
& + \alpha_s \left(1 - \frac{\beta_{m1}}{2} - \frac{\beta_{m2}}{2} \right) N_j^m(\bar\nu_e \to \bar\nu_\mu) \\
& + \alpha_s \left(1 + \frac{\beta_{m1}}{2} - \frac{\beta_{m2}}{2} \right) N_j^m(\bar\nu_\mu \to \bar\nu_\mu) - n_j^m(\mu) \Bigg]^2 \Bigg\} \Bigg] ,
\end{aligned}
\tag{5.4}
$$

$$
\begin{aligned}
\chi^2_{\rm upward} \;=\; \min_{\alpha_u} \Bigg\{ & \frac{\alpha_u^2}{\sigma_\alpha^2} + \sum_{j=1}^{10} \frac{1}{n_j^u(\mu)} \left[(1+\alpha_u) N_j^u(\nu_e \to \nu_\mu) + (1+\alpha_u) N_j^u(\nu_\mu \to \nu_\mu) \right. \\
& \left. + (1+\alpha_u) N_j^u(\bar\nu_e \to \bar\nu_\mu) + (1+\alpha_u) N_j^u(\bar\nu_\mu \to \bar\nu_\mu) - n_j^u(\mu) \right]^2 \Bigg\} .
\end{aligned}
\tag{5.5}
$$

The summation on j runs over the ten zenith angle bins. $n_j^a(\alpha)$ $(a = s, m; \alpha = e, \mu)$ and $n_j^u(\mu)$ stand for "the experimental data" for combined neutrino and anti-neutrino number of events for the sub-GeV and multi-GeV events, and that for the upward going μ events, respectively. $N_j^a(\nu_\alpha \to \nu_\beta)(N_j^a(\bar\nu_\alpha \to \bar\nu_\beta))$ stands for the prediction with our codes for the number of ℓ_β-like events $(\ell_\beta = e, \mu)$ of the sub-GeV and multi-GeV events and $N_j^u(\nu_\alpha \to \nu_\beta)(N_j^u(\bar\nu_\alpha \to \bar\nu_\beta))$ stands for that of the upward going μ events. α_a $(a = s, m, u)$ stands for the uncertainty in the overall flux normalization for the sub-GeV, multi-GeV, and upward going μ events, β_{a1} (β_{a2}) stands for the uncertainty in the relative normalization between ν_e - ν_μ flux (ν - $\bar\nu$ flux) for the sub-GeV $(a = s)$ and multi-GeV $(a = m)$ events, respectively. It is understood that χ^2 is minimized with respect to α_s, β_{sk} $(k = 1, 2)$, α_m, β_{mk} $(k = 1, 2)$, α_u. We have

put the systematic errors

$$\begin{aligned}
&\sigma_{\beta s1} = \sigma_{\beta m1} = 0.03, \\
&\sigma_{\beta s2} = \sigma_{\beta m2} = 0.05, \\
&\sigma_{\alpha} = 0.2
\end{aligned} \tag{5.6}$$

and we have assumed that α_s and α_m for the contained events are free parameters as in Ref. [97]. We have omitted the other uncertainties, such as the E_ν spectral index, the relative normalization between PC and FC and up-down correlation, etc., for simplicity. In particular, we confirmed that taking a uncertainty in the E_ν spectral index which is omitted in our analysis into consideration gives negligible contributions to χ^2. In addition to minimizing systematic uncertainty parameters, χ^2 is also minimized with respect to the mixing angle θ_{23}, the mass-squared difference $|\Delta m^2_{31}|$, the Dirac CP phase δ and the NSI phase $\arg(\epsilon_{e\tau})$. The other oscillation parameters give little effect on χ^2, so we have fixed them as $\sin^2 2\theta_{12} = 0.86$, $\sin^2 2\theta_{13} = 0.1$ and $\Delta m^2_{21} = 7.6 \times 10^{-5}\mathrm{eV}^2$.

On the other hand, in the case with the energy spectrum analysis, χ^2 for the

Sub-GeV and multi-GeV events in eq. (5.2) are replaced by

$$
\begin{aligned}
&\chi^2_{\rm sub-GeV} \\
= &\min_{\alpha_s,\beta' s,\gamma' s} \left[\frac{\beta_{s1}^2}{\sigma_{\beta s1}^2} + \frac{\beta_{s2}^2}{\sigma_{\beta s2}^2} + \frac{\gamma_{L1}^2}{\sigma_{\gamma L1}^2} + \frac{\gamma_{L2}^2}{\sigma_{\gamma L2}^2} + \frac{\gamma_{H1}^2}{\sigma_{\gamma H1}^2} + \frac{\gamma_{H2}^2}{\sigma_{\gamma H2}^2} \right. \\
&+ \sum_{A=L,H} \sum_{j=1}^{10} \left\{ \frac{1}{n_{Aj}^s(e)} \left[\alpha_s \left(1 - \frac{\beta_{s1}}{2} + \frac{\beta_{s2}}{2} + \frac{\gamma_{A1}^j}{2} \right) N_{Aj}^s(\nu_e \to \nu_e) \right. \right. \\
&+ \alpha_s \left(1 + \frac{\beta_{s1}}{2} + \frac{\beta_{s2}}{2} + \frac{\gamma_{A1}^j}{2} \right) N_{Aj}^s(\nu_\mu \to \nu_e) \\
&+ \alpha_s \left(1 - \frac{\beta_{s1}}{2} - \frac{\beta_{s2}}{2} + \frac{\gamma_{A1}^j}{2} \right) N_{Aj}^s(\bar{\nu}_e \to \bar{\nu}_e) \\
&\left. + \alpha_s \left(1 + \frac{\beta_{s1}}{2} - \frac{\beta_{s2}}{2} + \frac{\gamma_{A1}^j}{2} \right) N_{Aj}^s(\bar{\nu}_\mu \to \bar{\nu}_e) - n_{Aj}^s(e) \right]^2 \\
&+ \frac{1}{n_{Aj}^s(\mu)} \left[\alpha_s \left(1 - \frac{\beta_{s1}}{2} + \frac{\beta_{s2}}{2} + \frac{\gamma_{A2}^j}{2} \right) N_{Aj}^s(\nu_e \to \nu_\mu) \right. \\
&+ \alpha_s \left(1 + \frac{\beta_{s1}}{2} + \frac{\beta_{s2}}{2} + \frac{\gamma_{A2}^j}{2} \right) N_{Aj}^s(\nu_\mu \to \nu_\mu) \\
&+ \alpha_s \left(1 - \frac{\beta_{s1}}{2} - \frac{\beta_{s2}}{2} + \frac{\gamma_{A2}^j}{2} \right) N_{Aj}^s(\bar{\nu}_e \to \bar{\nu}_\mu) \\
&\left. \left. \left. + \alpha_s \left(1 + \frac{\beta_{s1}}{2} - \frac{\beta_{s2}}{2} + \frac{\gamma_{A2}^j}{2} \right) N_{Aj}^s(\bar{\nu}_\mu \to \bar{\nu}_\mu) - n_{Aj}^s(\mu) \right]^2 \right\} \right] , \qquad (5.7)
\end{aligned}
$$

$$
\begin{aligned}
&\chi^2_{\text{multi-GeV}} \\
= &\min_{\alpha_m,\beta's,\gamma's} \left[\frac{\beta^2_{m1}}{\sigma^2_{\beta m1}} + \frac{\beta^2_{m2}}{\sigma^2_{\beta m2}} + \frac{\gamma^2_1}{\sigma^2_{\gamma 1}} + \frac{\gamma^2_2}{\sigma^2_{\gamma 2}} \right. \\
&+ \sum_{A=L,H} \sum_{j=1}^{10} \left\{ \frac{1}{n^m_{Aj}(e)} \left[\alpha_m \left(1 - \frac{\beta_{m1}}{2} + \frac{\beta_{m2}}{2} + \frac{\gamma^j_1}{2} \right) N^m_{Aj}(\nu_e \to \nu_e) \right. \right. \\
&+\alpha_m \left(1 + \frac{\beta_{m1}}{2} + \frac{\beta_{m2}}{2} + \frac{\gamma^j_1}{2} \right) N^m_{Aj}(\nu_\mu \to \nu_e) \\
&+\alpha_m \left(1 - \frac{\beta_{m1}}{2} - \frac{\beta_{m2}}{2} + \frac{\gamma^j_1}{2} \right) N^m_{Aj}(\bar{\nu}_e \to \bar{\nu}_e) \\
&\left. +\alpha_m \left(1 + \frac{\beta_{m1}}{2} - \frac{\beta_{m2}}{2} + \frac{\gamma^j_1}{2} \right) N^m_{Aj}(\bar{\nu}_\mu \to \bar{\nu}_e) - n^m_{Aj}(e) \right]^2 \\
&+ \frac{1}{n^m_{Aj}(\mu)} \left[\alpha_m \left(1 - \frac{\beta_{m1}}{2} + \frac{\beta_{m2}}{2} + \frac{\gamma^j_2}{2} \right) N^m_{Aj}(\nu_e \to \nu_\mu) \right. \\
&+\alpha_m \left(1 + \frac{\beta_{m1}}{2} + \frac{\beta_{m2}}{2} + \frac{\gamma^j_2}{2} \right) N^m_{Aj}(\nu_\mu \to \nu_\mu) \\
&+\alpha_m \left(1 - \frac{\beta_{m1}}{2} - \frac{\beta_{m2}}{2} + \frac{\gamma^j_2}{2} \right) N^m_{Aj}(\bar{\nu}_e \to \bar{\nu}_\mu) \\
&\left. \left. \left. +\alpha_m \left(1 + \frac{\beta_{m1}}{2} - \frac{\beta_{m2}}{2} + \frac{\gamma^j_2}{2} \right) N^m_{Aj}(\bar{\nu}_\mu \to \bar{\nu}_\mu) - n^m_{Aj}(\mu) \right]^2 \right\} \right] . \qquad (5.8)
\end{aligned}
$$

The summation on $A = L, H$ runs over the two energy bins. The indices L and H stand for the lower ($E < E_{\text{th}}$) and higher ($E > E_{\text{th}}$) energy bins, respectively. For all the zenith angle bins, the threshold energy for the sub-GeV events is 0.5GeV and that for the multi-GeV events is 3.2GeV. The threshold energy E_{th} is chosen so that the numbers of events for the lower and higher energy bins are approximately equal. The experimental data $n^a_{Aj}(\alpha)$ ($a = s, m; \alpha = e, \mu$) stands for the sum of the number of neutrinos and antineutrinos events for the sub-GeV and multi-GeV events, and the experimental data $n^u_j(\mu)$ stands for that for the upward going μ events. $N^a_{Aj}(\nu_\alpha \to \nu_\beta)(N^a_{Aj}(\bar{\nu}_\alpha \to \bar{\nu}_\beta))$ stands for the prediction with our codes for the number of ℓ_β-like events ($\ell_\beta = e, \mu$) of the sub-GeV and multi-GeV events and $N^u_j(\nu_\alpha \to \nu_\beta)(N^u_j(\bar{\nu}_\alpha \to \bar{\nu}_\beta))$ stands for that of the upward going μ events.

We introduced the flavor and energy dependent relative normalization between the upward and downward bins for the sub-GeV and multi-GeV events $\gamma's$

$$\gamma^j_{A1,2} = \begin{cases} \gamma_{A1,2} & (j \leq j_{\rm th}; A = L, H) \\ -\gamma_{A1,2} & (j > j_{\rm th}; A = L, H) \end{cases}$$
$$\gamma^j_{1,2} = \begin{cases} \gamma_{1,2} & (j \leq j_{\rm th}) \\ -\gamma_{1,2} & (j > j_{\rm th}). \end{cases}$$

Here $j_{\rm th} = 3$ is the index which separates the upward and downward bins and determined in the investigation of the significance of the wrong mass hierarchy. We have checked that the choice of the upward-downward separation index $j_{\rm th}$ do not affect the sensitivity to NSI significantly. We have set the systematic errors to the same values as in Ref. [97]

$$\begin{aligned} &\sigma_{\beta s1} = \sigma_{\beta m1} = 0.03, \\ &\sigma_{\beta s2} = \sigma_{\beta m2} = 0.05, \\ &\sigma_{\alpha} = 0.2, \\ &\sigma_{\gamma L1} = 0.005, \\ &\sigma_{\gamma L2} = 0.008, \\ &\sigma_{\gamma H1} = 0.021, \\ &\sigma_{\gamma H2} = 0.018, \\ &\sigma_{\gamma 1} = 0.015, \\ &\sigma_{\gamma 2} = 0.008, \end{aligned} \tag{5.9}$$

and omitted other systematic errors for simplicity as is the case with the energy rate analysis.

5.1.1 The case with $\epsilon_{\alpha\mu} = 0$ and $\epsilon_{\tau\tau} = |\epsilon_{e\tau}|^2/(1 + \epsilon_{ee})$

In this subsection we show the results of energy rate and spectrum analysis in the case with $\epsilon_{\alpha\mu} = 0$ ($\alpha = e, \mu, \tau$) and $\epsilon_{\tau\tau} = |\epsilon_{e\tau}|^2/(1 + \epsilon_{ee})$ at HK. The allowed regions from energy rate (spectrum) analysis are shown in the upper (lower) panel of Fig. 5.1. From the energy rate analysis, we get a constraint on $\tan\beta = |\epsilon_{e\tau}|/|(1+\epsilon_{ee})| \lesssim 0.3$ at 2.5σC.L. On the other hand, from the energy spectrum analysis, we get constraints $-0.1 \lesssim \epsilon_{ee} \lesssim 0.2$ and $|\epsilon_{e\tau}| < 0.08$ at 2.5σ (98.8%) C.L. for the normal hierarchy and $-0.4 \lesssim \epsilon_{ee} \lesssim 1.2$ and $|\epsilon_{e\tau}| < 0.34$ at 2.5σ (98.8%) C.L. for the inverted hierarchy.

Notice that the constraints from normal hierarchy are much stronger than those from inverted hierarchy in both the energy rate and spectrum analysis and the energy spectrum analysis gives the narrow allowed regions compared with those from

energy rate analysis. To understand these phenomena, we have plotted $\chi^2_{\mathrm{multi-GeV}}$ as a function of ϵ_{ee} with $|\epsilon_{e\tau}| = 0$ in Fig. 5.2. Hence the multi-GeV events are sensitive to the matter effect and hence to NSI. In plotting Fig. 5.2, we have taken into account only the statistical errors for simplicity, and we assume that the HK detector could distinguish neutrinos and antineutrinos for both e-like and μ-like events in all the energy ranges of the multi-GeV events, and that the detection efficiency is the same for both neutrinos and antineutrinos. Since the SK collaboration distinguish neutrinos and antineutrinos only for the multi-GeV e-like events [96], our assumption here may not be realistic, and the separate plots for neutrinos or for antineutrinos except for the e-like events should be regarded as information for theoretical consideration. Comparing the figures ((a) and (b)) in the top row and those ((e) and (f)) in the bottom row, we see that, even if some of the data set in the spectrum analysis have a sensitivity to the effect of ϵ_{ee}, the data in the rate analysis does not necessarily have a sensitivity to ϵ_{ee}. This is prominent for $\epsilon_{ee} > 0$. While it is not clear to us why the sensitivity is lost only for $\epsilon_{ee} > 0$, we have found that, if we try to fit the same data with the numbers of events with the wrong mass hierarchy, then the plot becomes left-right reversed, i.e., the sensitivity is lost only for $\epsilon_{ee} < 0$. On the other hand, by comparing the figures ((c) and (d)) in the middle row and those ((e) and (f)) in the bottom row, we see that, in the case of the inverted mass hierarchy, even though the separate $\bar{\nu}_\mu$ data has a sensitivity to ϵ_{ee}, the combined data $\nu_\mu + \bar{\nu}_\mu$ loses a sensitivity. We could not explain these phenomena using the analytic expression for the oscillation probability, but we interpret this loss of sensitivity as a destructive phenomenon between neutrinos and antineutrinos in the rate analysis, and between the lower and higher energy bins in the spectrum analysis for the inverted mass hierarchy.

To visualize how this destructive phenomenon happens in terms of the numbers of events, we have plotted in Fig. 5.3 the difference of the numbers of the multi-GeV μ-like events with standard scenario and those with NSI for a typical case: (ϵ_{ee}, $\epsilon_{e\tau}$)=(2,0). From Fig. 5.3 we see that each positive and negative contribution to the difference in the ν_μ events (Fig. 5.3 (a)) is almost cancelled by negative and positive contribution in the $\bar{\nu}_\mu$ events Fig. 5.3 (b), so the difference in the combined events (Fig. 5.3 (c)) significance is reduced.

Although we have not thoroughly investigated, according to our investigation for a specific case ($\epsilon_{ee} = 0$), this destructive phenomenon does not happen for $|\epsilon_{e\tau}|$, i.e., distinction between neutrinos and antineutrinos does not make much difference on the sensitivity to $|\epsilon_{e\tau}|$. This conclusion is consistent with the result of Ref. [79], in which the sensitivity to $|\epsilon_{e\tau}|$ was studied, although they took a set of assumptions different from ours. This destructive phenomenon seems to be characteristic to the sensitivity to ϵ_{ee} because of the asymmetry between the cases for $\epsilon_{ee} + 1 > 0$ and for

$\epsilon_{ee} + 1 < 0$.

It is expected that the HK experiment will be able to use information on the energy spectrum, so we believe that the allowed region in the lower panel in Fig. 5.1 with the energy spectrum analysis reflects the true HK sensitivity more than that in the upper panel does. Therefore we also adopt the energy spectrum analysis in the next subsection.

Next let us discuss the case where "the experimental data" is the one obtained with $(\epsilon_{ee}, \epsilon_{e\tau}) \neq (0, 0)$. The analysis is the same as the energy spectrum analysis in this subsection, except that the "the experimental data" is produced assuming the presence of NSI. The results are shown in Fig. 5.4, where the allowed regions at 2.5σ ($\Delta\chi^2 = 8.8$ for 2 degrees of freedom) around the true points are depicted. The straight lines $|\epsilon_{e\tau}| = 0.8 \times |1 + \epsilon_{ee}|$ in Fig. 5.4 stand for the approximate bound from the SK atmospheric neutrinos [89], and we have examined only the points below these straight lines. As seen from Fig. 5.4, the errors in ϵ_{ee} and $|\epsilon_{e\tau}|$ are small for $|\epsilon_{ee}| \lesssim 2$ in the case of the normal hierarchy and for $-3 \lesssim \epsilon_{ee} \lesssim 1$ in the case of the inverted hierarchy. The errors are large otherwise, and the reason that the errors are large is because a sensitivity is lost due to a destructive phenomenon between neutrinos and antineutrinos as was discussed above.

We note in passing that there are a couple of points in Fig. 5.4, where the allowed region has an additional isolated island. This is regarded as so-called parameter degeneracy, which is classified into the intrinsic degeneracy [98], the sign degeneracy [10] and the octant degeneracy [11, 8] in the standard three-flavor framework, in the presence of the NSI. Since little is known about parameter degeneracy in the presence of the new physics and since the study of the subject is beyond the scope of this thesis, we do not discuss parameter degeneracy with NSI here.

5.1.2 The case without any assumptions

In this subsection we show results of sensitivities to NSI without the assumptions. A definition of χ^2 and NSI parameterization used in this subsection are different from those used in the preceding subsection. NSI is parametrized as $\epsilon_{D,N}$ and hence the allowed regions are given in the $(\epsilon_D, |\epsilon_N|)$ plane.

χ^2 used in the analysis is defined as

$$\chi^2 = \min_{\theta_{23}, |\Delta m^2_{32}|, \delta, \epsilon_{\alpha\beta}} \left(\chi^2_{\text{sub-GeV}} + \chi^2_{\text{multi-GeV}} + \chi^2_{\text{upward}} + \chi^2_{\text{prior}} \right), \tag{5.10}$$

where $\chi^2_{\text{sub-GeV}}$, $\chi^2_{\text{multi-GeV}}$ and χ^2_{upward} are the same as in the energy spectrum anal-

ysis discussed in the preceding subsection and $\chi^2_{\rm prior}$ is defined as

$$\chi^2_{\rm prior} = \Delta\chi^2_{\rm prior}\frac{|\epsilon^f_{e\mu}|^2}{|\delta\epsilon^f_{e\mu}|^2} + \Delta\chi^2_{\rm prior}\frac{|\epsilon^f_{\mu\tau}|^2}{|\delta\epsilon^f_{\mu\tau}|^2}. \tag{5.11}$$

Where $\Delta\chi^2_{\rm prior} = 2.7$ in $\chi^2_{\rm prior}$ stands for χ^2 for 90%CL with 1 d.o.f. and $|\delta\epsilon^f_{e\mu}| = |\delta\epsilon^f_{\mu\tau}| = 0.05$ stand for constraint on corresponding NSI at 90%CL, respectively. It is also understood that χ^2 is minimized with respect to the systematic uncertainty, the oscillation parameters θ_{23}, $|\Delta m^2_{31}|$, δ, and the NSI parameter except for ϵ_D and $|\epsilon_N|$.

The sensitivity of the atmospheric neutrino experiment to NSI which is parametrized as (ϵ_D, ϵ_N) is studied as follows.

1. Set a grid on the (ϵ_D, $|\epsilon_N|$) plane.

2. Calculate a parameter set ($|\epsilon_{e\tau}|, \epsilon_{ee} - \epsilon_{\mu\mu}, \epsilon_{\tau\tau} - \epsilon_{\mu\mu}$) via Eq. (4.14) for the given point (ϵ_D, $|\epsilon_N|$) on the grid varying Δm^2_{31}, θ_{23}, $\delta_{\rm CP}$, $|\epsilon_{e\mu}|$, $|\epsilon_{\mu\tau}|$, ψ and $\phi_{\alpha\beta}$.

3. Dismiss the parameter set if it does not satisfy any one of the following criteria:

$$|\epsilon_{e\tau}| \leq 1.5 \tag{5.12}$$
$$|\epsilon_{ee} - \epsilon_{\mu\mu}| \leq 2.0 \tag{5.13}$$
$$\min_{\pm}\left(\left|1 + (\epsilon_{ee} - \epsilon_{\mu\mu}) + (\epsilon_{\tau\tau} - \epsilon_{\mu\mu}) \pm \sqrt{(1 + \epsilon_{ee} - \epsilon_{\tau\tau})^2 + 4|\epsilon_{e\tau}|^2}\right|\right) \leq 0.4 \tag{5.14}$$

4. Calculate χ^2 for each parameter set which passed the criteria mentioned above and then obtain the minimum value of χ^2 for the given (ϵ_D, $|\epsilon_N|$).

As mentioned in section 4.3, the atmospheric neutrino experiments constrain the relation between ϵ_{ee}, $|\epsilon_{e\tau}|$ and $\epsilon_{\tau\tau}$. Eq. (5.14) is still valid when we replace ϵ_{ee} with $(\epsilon_{ee} - \epsilon_{\mu\mu})$ and $\epsilon_{\tau\tau}$ with $(\epsilon_{\tau\tau} - \epsilon_{\mu\mu})$. This replacement can be understood as a redefinition of the standard NSI parameterization because one can always subtract the modified MSW potential (4.3) by a matrix proportional to identity, say $\epsilon_{\mu\mu}\mathbf{1}_{3\times3}$, as far as the oscillation probability is concerned. Therefore if the parameter set ($|\epsilon_{e\tau}|, \epsilon_{ee} - \epsilon_{\mu\mu}, \epsilon_{\tau\tau} - \epsilon_{\mu\mu}$) which is determined by the independent parameters dose not satisfy Eq. (5.14), we can exclude it without fitting to the experimental data. In addition to this criterion, we can also exclude the parameter set which dose not satisfy Eq. (5.12) or Eq. (5.13). Eqs. (5.12) and (5.13) are sufficient conditions for significance to be larger than 5σ in the analysis with $\epsilon_{\alpha\mu} = 0$ and $\epsilon_{\tau\tau} = |\epsilon_{e\tau}|^2/(1 + \epsilon_{ee})$ (the results were given in the preceding subsection 5.1.1). When small parameters

$\epsilon_{\alpha\mu}$ are introduced, these conditions are expected to be valid to avoid calculating meanless parameter sets.

Taking into account the constraints on NSI given by the previous researches, we vary NSI parameters as follows:

$$\begin{aligned} 0 \leq \quad & |\epsilon^d_{e\mu}| \quad \leq 0.05 \\ 0 \leq \quad & |\epsilon^d_{\mu\tau}| \quad \leq 0.05 \\ 0 \leq \quad & \phi_{\alpha\beta} \quad < 2\pi \\ 0 \leq \quad & \psi \quad < 2\pi. \end{aligned} \tag{5.15}$$

The results are shown in Fig. 5.5. The best-fit values $(\epsilon^d_D, \epsilon^d_N) = (-0.12, -0.16)$ for NSI with $f = d$ from the solar neutrino and KamLAND data given by Ref. [58] is excluded at 11σ (8.2σ) for the normal (inverted) hierarchy. In the case of NSI with $f = u$, the best-fit value $(\epsilon^u_D, \epsilon^u_N) = (-0.22, -0.30)$ is far from the standard scenario $(\epsilon_D, \epsilon_N) = (0.0, 0.0)$ compared with the case of $f = u$ and also excluded at 38σ (35σ) for the normal (inverted) hierarchy. On the other hand, the best-fit value from the global analysis of the neutrino oscillation data [58] $(\epsilon^d_D, \epsilon^d_N) = (-0.145, -0.036)$ for NSI with $f = d$ is excluded at 5.0σ (3.7σ) for the normal (inverted) hierarchy. In the case of NSI with $f = u$, the best-fit value $(\epsilon^u_D, \epsilon^u_N) = (-0.140, -0.030)$ is excluded at 5.0σ (1.4σ) for the normal (inverted) hierarchy. Notice that the fermion subscript f on ϵ^f_D and ϵ^f_N is important in the case of the solar neutrinos analysis because the number densities of up and down quarks are different in the Sun. On the other hand, as mentioned above, in the case of atmospheric neutrinos the fermion subscript is not important because the number densities of up and down quarks are approximately the same in the Earth. Sensitivities to NSI with a different choice of true δ value are shown Fig. 5.6.

To compare our results with the one given in Ref. [58], we show the allowed regions assuming real ϵ_N in Fig. 5.7. This is given by setting $\arg(\epsilon_N) = \psi = 0, \pi$ in Eq. (4.11), where $\delta_{\rm CP}$ and $\phi_{\alpha\beta}$ do not need to be 0 or π. As can be seen from Fig. 5.7, the allowed regions for positive ϵ_N and for negative one are almost symmetric. We found that the allowed regions in Fig. 5.5 are not so different from that in the upper plane of Fig. 5.7. Therefore the sensitivity of the HK atmospheric neutrino experiment to ψ is poor. Sensitivities to NSI assuming real ϵ_N with a different choice of true δ value are shown Fig. 5.8.

To see which bin contributes to χ^2 most, we focused on the number of events difference between the standard scenario and the scenario with NSI (the red and black circle points in Fig. 5.5). Then we found that the multi-GeV μ-like events coming from the below in the high-energy-bin most contributes to χ^2. This is because

difference between the oscillation probability with NSI and without NSI is large where the neutrino energy is above 10 GeV. We plotted the numbers of events for the multi-GeV μ-like events in the high-energy-bin in Fig. 5.9.

Finally, in Fig. 5.10, we have plotted the sensitivity of HK to NSI for the best-fit values of the global and (solar+KamLand) data as a function of the data size. We found that the best-fit value from the (solar+KamLand) data is excluded at 5σ after about 2(4) years of exposure in the case of NH(IH) assuming 0.56Mton fiducial volume. The best-fit value of the global data is excluded at 5σ after about 12 years of exposure in the case of NH. On the other hand in the case of IH, the best-fit value of the global data is excluded at 2σ after about 20 years of exposure. Fig. 5.10 shows that the sensitivities are almost proportional to the data size and therefore those are dominated by statistics.

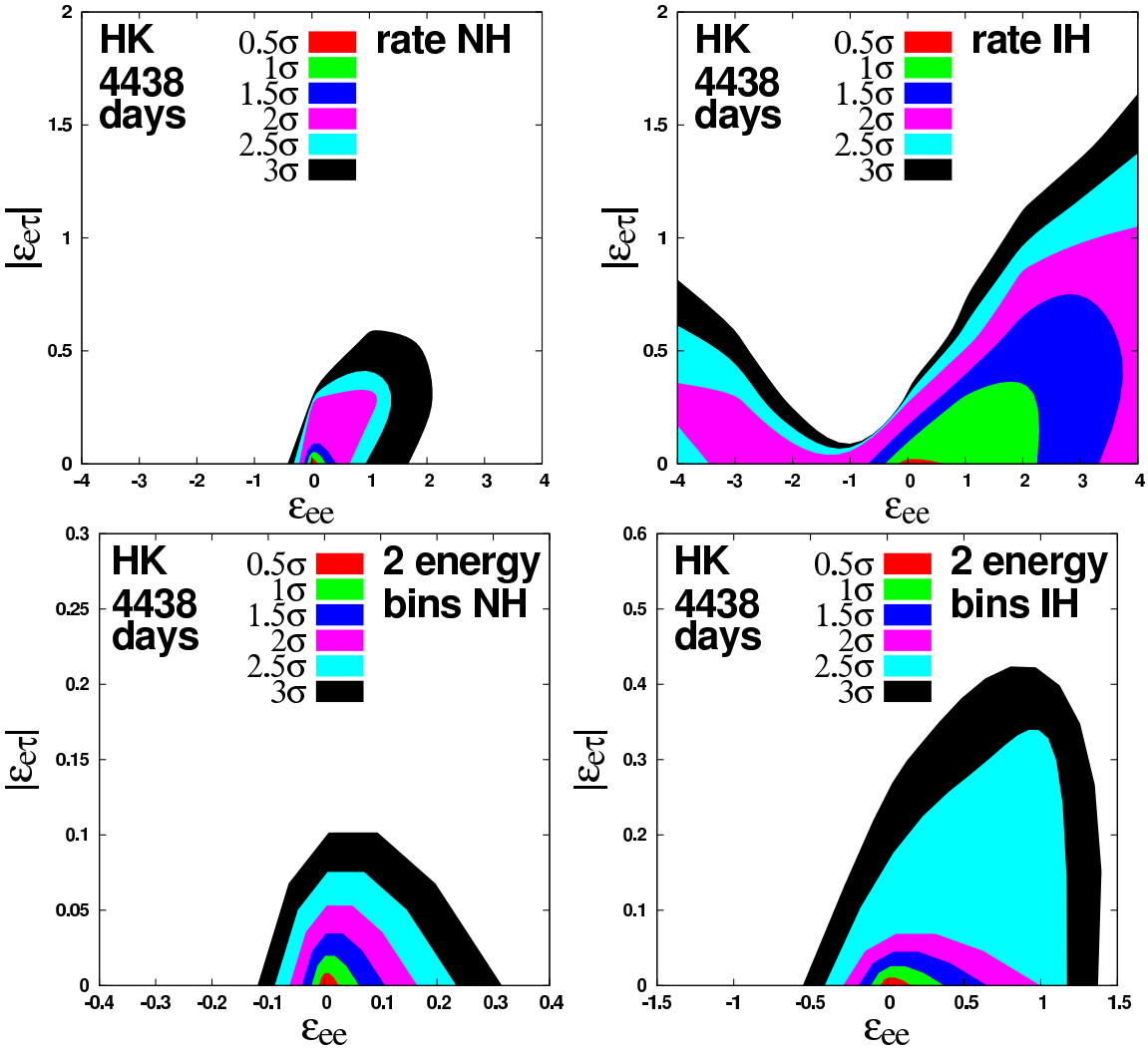

Figure 5.1: Upper panel: The allowed region in the (ϵ_{ee}, $|\epsilon_{e\tau}|$) plane from the HK atmospheric neutrino data for a normal mass hierarchy (left panel) and for an inverted mass hierarchy (right panel) from the energy-rate analysis. Lower panel: The same allowed region as the upper panel from the two energy-bin analysis. Notice that the vertical scales in the lower panel are different for both mass hierarchies from the one in the upper panel.

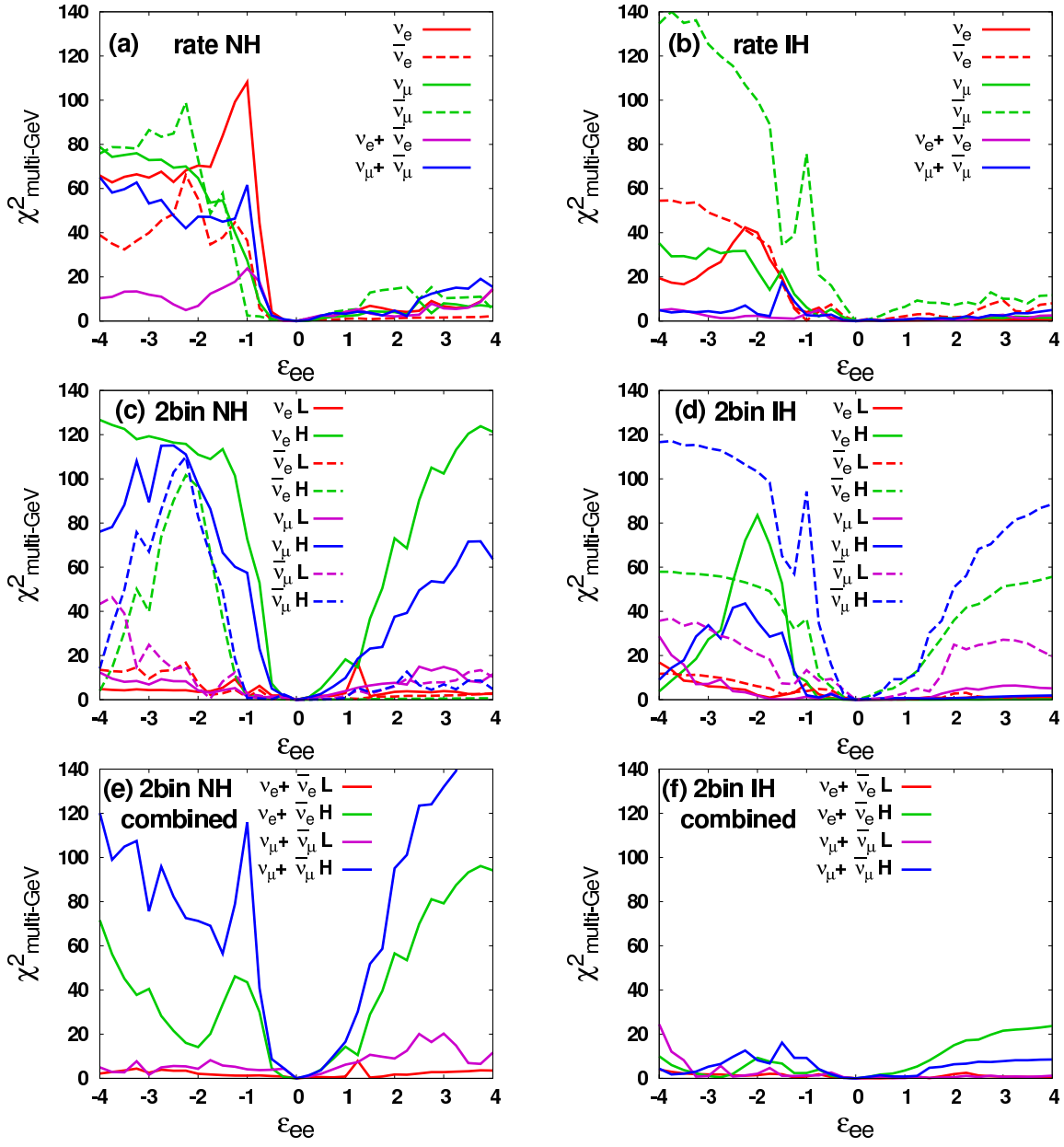

Figure 5.2: The behaviors of $\chi^2_{\text{multi}-\text{GeV}}$ for $\epsilon_{e\tau} = 0$ as a function of ϵ_{ee}. (a), (b): Energy rate analysis for NH (a) and IH (b). (c), (d): Energy spectrum analysis for NH (d) and IH (e) for the separate neutrino or antineutrino events. (e), (f): Energy spectrum analysis for NH (e) and IH (f) using only the combined numbers of events of $\nu_e + \bar{\nu}_e$ and $\nu_\mu + \bar{\nu}_\mu$. In (a), (b), (c) and (d), the plots for the separate neutrino or antineutrino events are created based on the assumption that HK could distinguish neutrinos and antineutrinos.

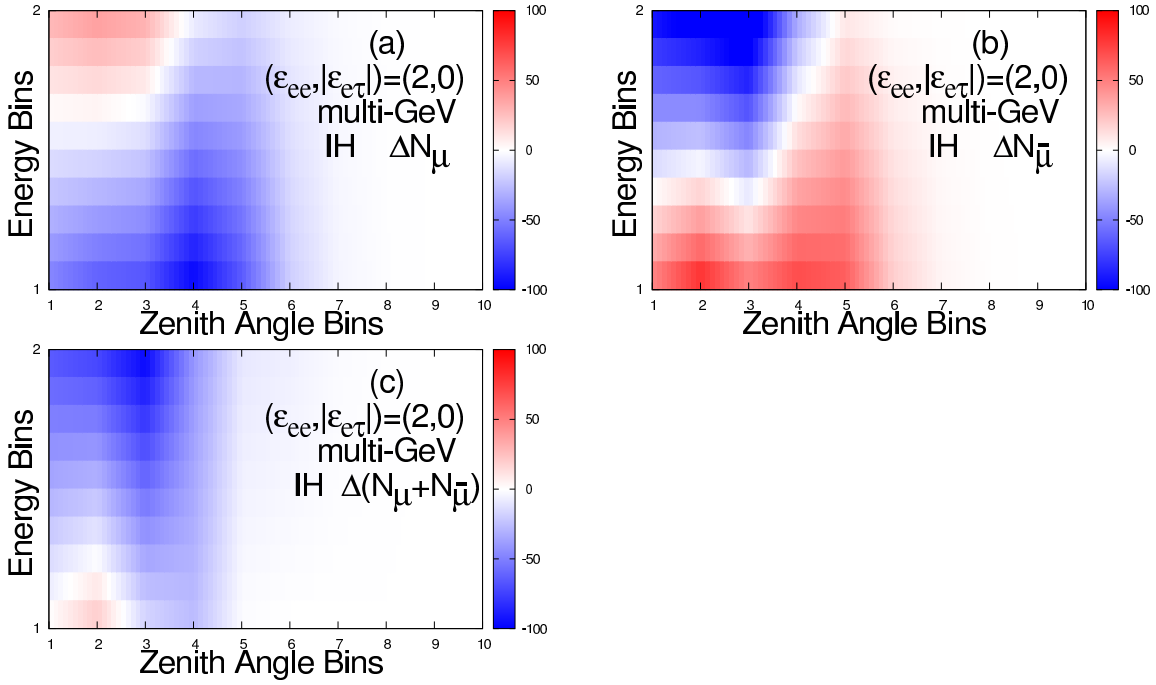

Figure 5.3: The behaviors of the difference of the numbers of the multi-GeV μ-like events with the standard scenario and those with NSI (ϵ_{ee}, $\epsilon_{e\tau}$)=(2,0). The vertical axis stands for the energy bin (1 for the lower energy and 2 for the higher energy), and the horizontal axis is the zenith angle bin (1 for $-1.0 < \cos\Theta < -0.8$, $\cdots$, 10 for $0.8 < \cos\Theta < 1.0$). (a): The difference of the numbers of the multi-GeV ν_μ-like events. (b): The difference of the numbers of the multi-GeV $\bar{\nu}_\mu$-like events. (c): The difference of the numbers of the multi-GeV ν_μ-like and $\bar{\nu}_\mu$-like events.

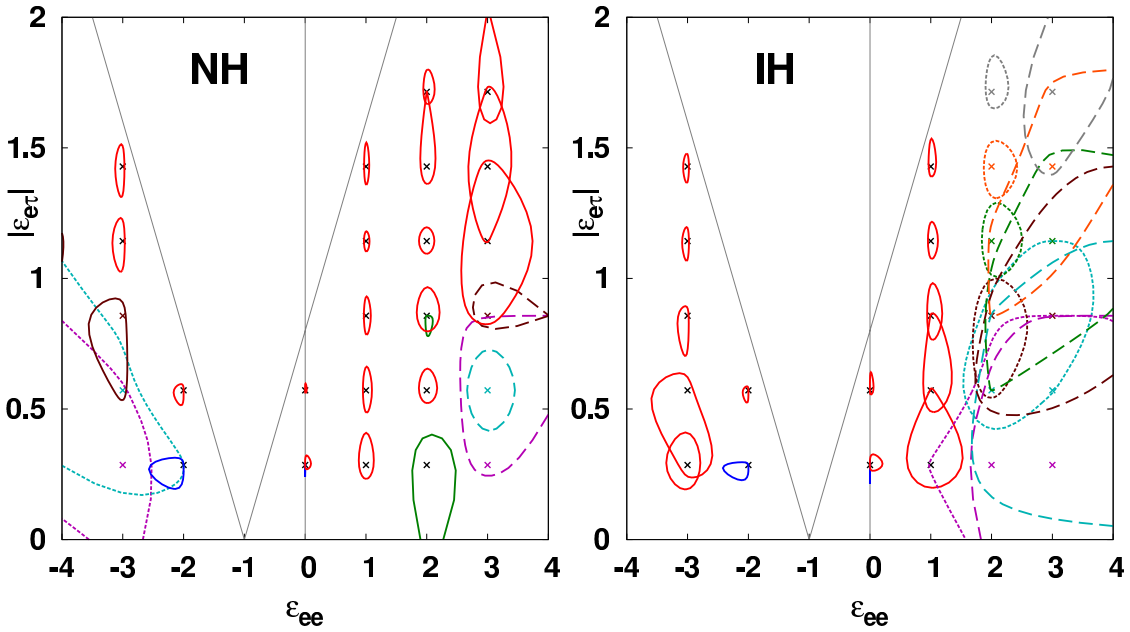

Figure 5.4: The allowed region at 2.5σC.L. around the point $(\epsilon_{ee}, |\epsilon_{e\tau}|) \neq (0, 0)$, where $\bar{\delta} = \arg(\bar{\epsilon}_{e\tau}) = 0$ is assumed. Most of the allowed regions are connected, but those around a few points have an isolated island, and they are depicted in different colors: In the left panel, the blue curves around (ϵ_{ee}, $|\epsilon_{e\tau}|$)=(-2, 2/7) and (0, 2/7) correspond to the degenerate allowed regions for the true values of (-2, 2/7), the green curves around (2, 2/7) and (2, 6/7) are the degenerate allowed regions for the true values of (2, 2/7), and the brown curves around (-3, 6/7) and (-4, 8/7) are the degenerate allowed regions for the true values of (-3, 6/7). In the right panel, the blue curves around (-2, 2/7) and (0, 2/7) correspond to the degenerate allowed regions for the true values of (-2, 2/7). The allowed regions at $\epsilon_{ee} = \pm 3$ for the normal mass hierarchy and at $\epsilon_{ee} = 2, 3$ for the inverted mass hierarchy are much wider compared with other cases, so their boundary are shown with dashed lines for $\epsilon_{ee} = 3$ (NH & IH) and with dotted lines for $\epsilon_{ee} = -3$ (NH) and $\epsilon_{ee} = 2$ (IH). Also these boundary and their centers are shown in different colors: purple for $|\epsilon_{e\tau}| = 2/7$, light blue for $|\epsilon_{e\tau}| = 4/7$, brown for $|\epsilon_{e\tau}| = 6/7$, green for $|\epsilon_{e\tau}| = 8/7$, orange for $|\epsilon_{e\tau}| = 10/7$, and grey for $|\epsilon_{e\tau}| = 12/7$.

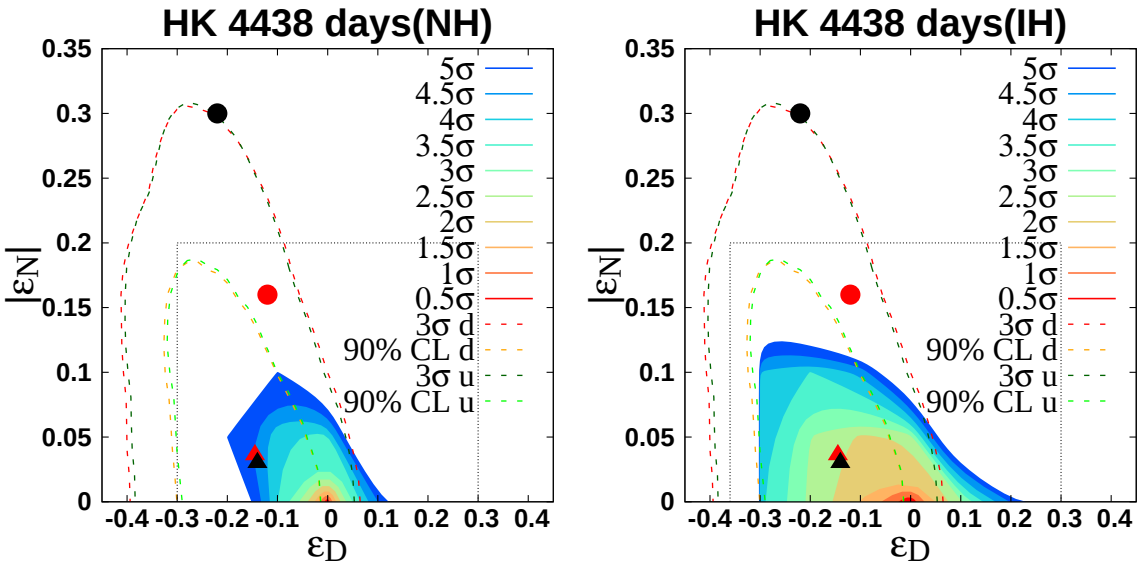

Figure 5.5: The allowed region in the (ϵ_D, $|\epsilon_N|$) plane from the HK atmospheric neutrino data for the normal hierarchy (left panel) and for the inverted hierarchy (right panel). We calculated χ^2 for (ϵ_D, $|\epsilon_N|$) inside the area surrounded by dotted lines and at the best-fit points. The red ($f = d$) and black ($f = u$) circles indicate the best-fit point from the solar neutrino and KamLAND data [58] for NSI with $(\epsilon^d_D, \epsilon^d_N) = (-0.12, -0.16)$ (red) and that for NSI with $(\epsilon^u_D, \epsilon^u_N) = (-0.22, -0.30)$ (black), respectively. In the case of the normal hierarchy, χ^2 for the red and black circles are 128.49 (11σ) and 1670.4 (38σ), respectively, and in the case of the inverted hierarchy, χ^2 for the red and black circles are 72.531 (8.2σ) and 1265.4 (35σ), respectively. The red and black triangles indicate the best-fit value from the global neutrino oscillation experiments analysis [58] for NSI with $(\epsilon^d_D, \epsilon^d_N) = (-0.145, -0.036)$ (red) and that for NSI with $(\epsilon^u_D, \epsilon^u_N) = (-0.140, -0.030)$ (black), respectively. In the case of the normal hierarchy, χ^2 for the red and black triangles are 28.967 (5.0σ) and 28.2934 (5.0σ), respectively, and in the case of the inverted hierarchy, χ^2 for the red and black triangles are 4.1077 (1.5σ) and 3.7412 (1.4σ), respectively. The dashed lines are the boundaries of the allowed regions from the global neutrino oscillation experiments analysis. For reference, we plotted for both the cases with $f = u$ and $f = d$.

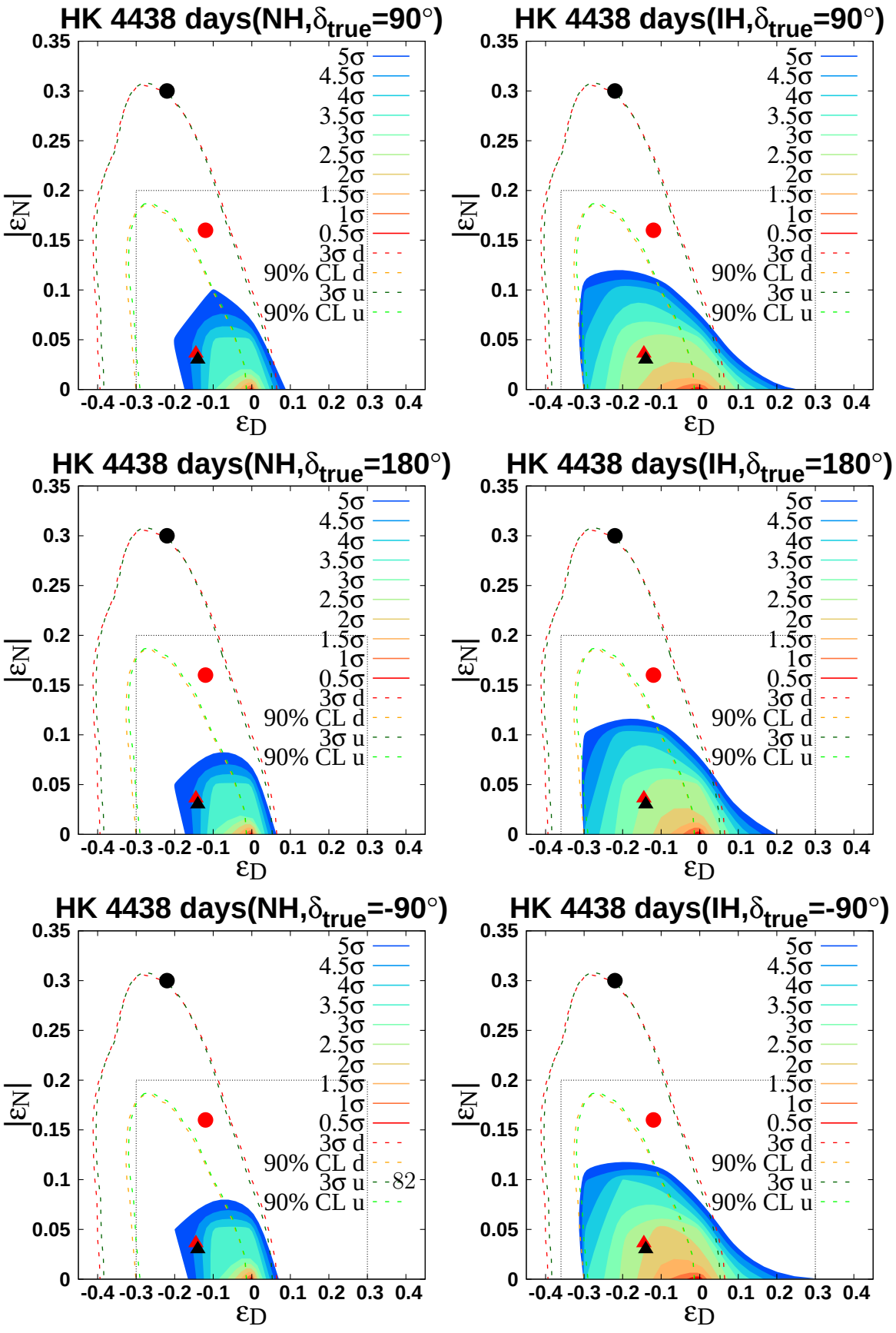

Figure 5.6: The same plots of Fig. 5.5 except a choice of the value of true δ.

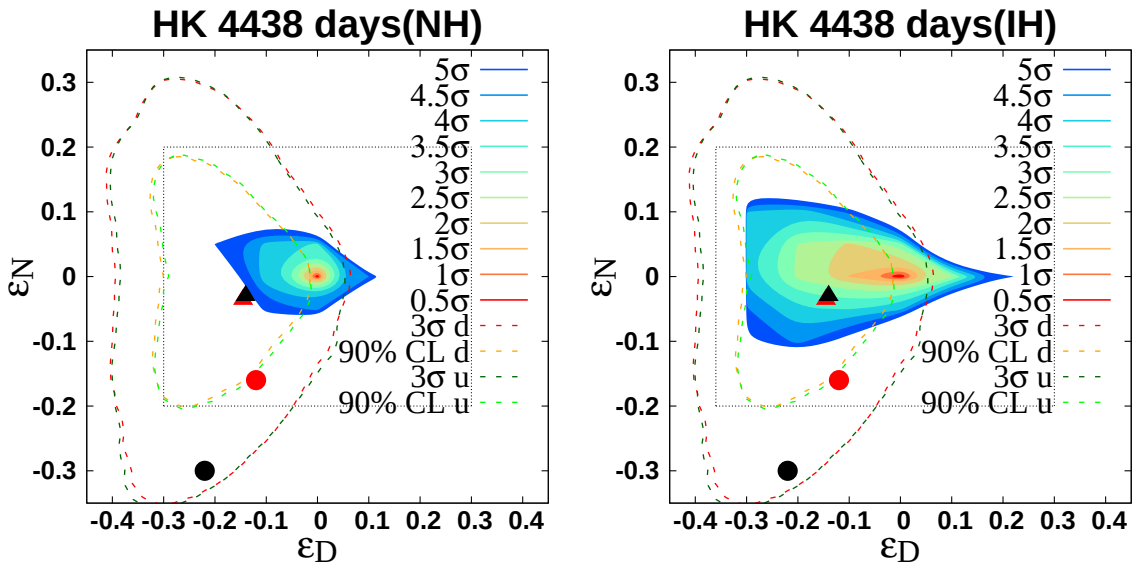

Figure 5.7: The allowed regions assuming real ϵ_N.

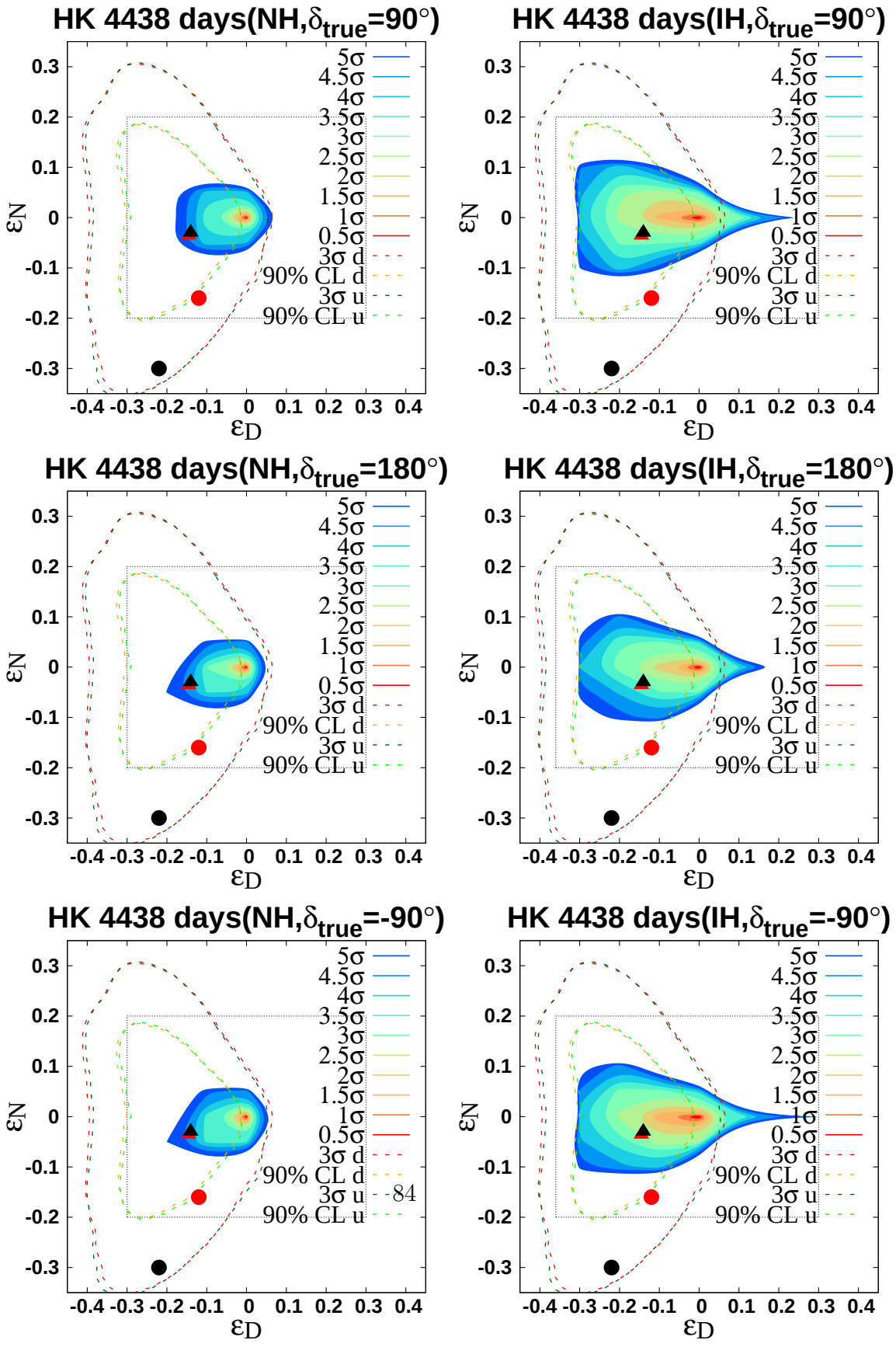

Figure 5.8: The same plots of Fig. 5.7 except a choice of the value of δ.

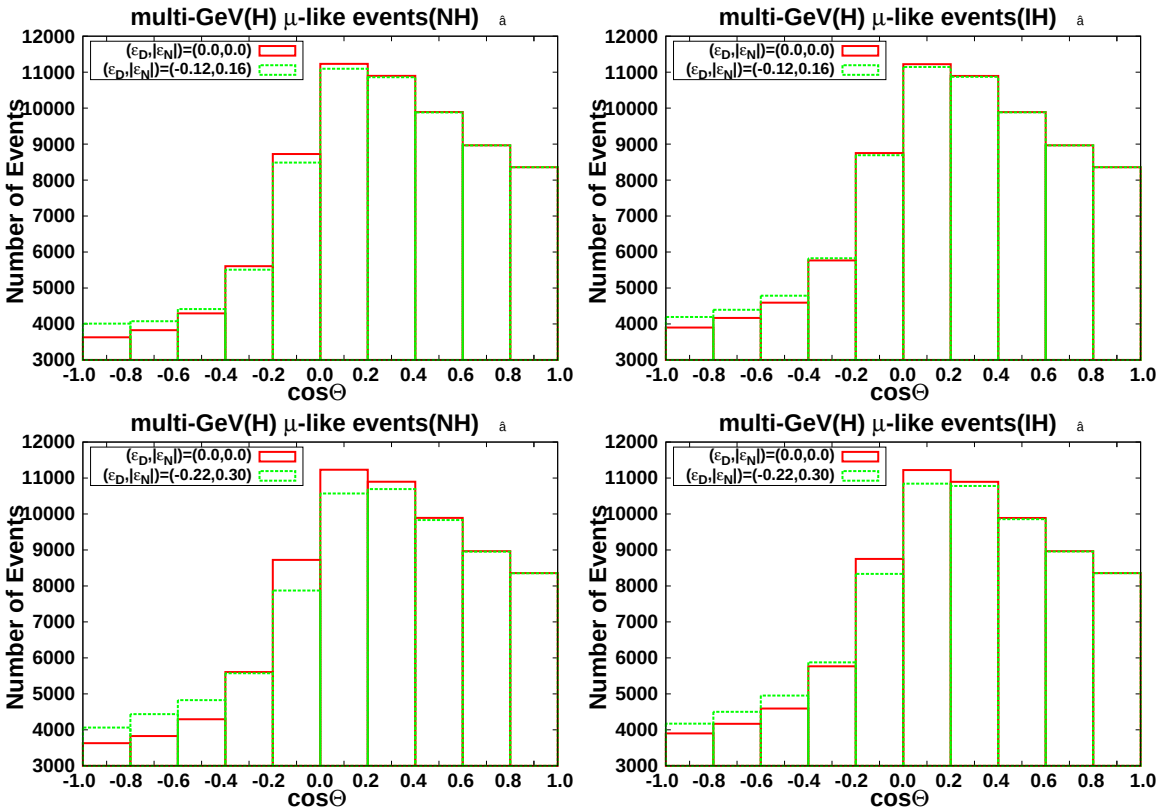

Figure 5.9: The number of the high-energy-bin multi-GeV μ-like events (the red and green boxes are the standard scenario and the scenario with NSI, respectively). The horizontal axis is the zenith angle bin.

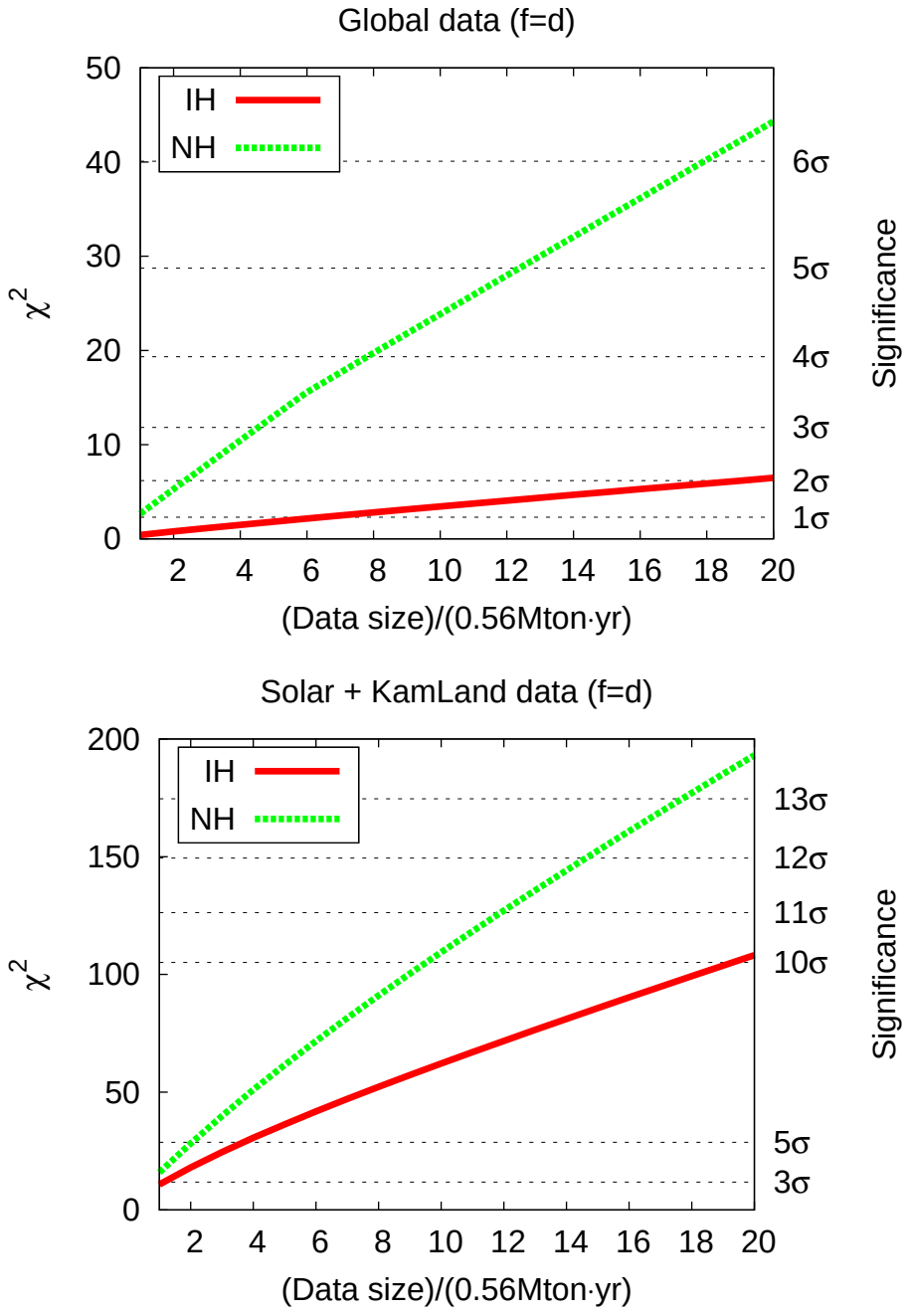

Figure 5.10: The sensitivity of HK to NSI for the NSI best-fit values from the global and (solar+KamLand) data as a function of the data size assuming 0.56Mton fiducial volume.

Chapter 6

A Octant Degeneracy in Hyper Kamiokande

In this chapter we discuss how the octant degeneracy appear in the atmospheric neutrino oscillation measurements at HK. This can be understood by looking at the number of events for several values of θ_{23}. Notice that the octant degeneracy is accompanied by the mass hierarchy degeneracy. Parameter degeneracy in the standard three flavor framework has been widely discussed in the context of long baseline experiments, while the subject has not been discussed much in the atmospheric neutrino measurements. HK observes e-like and μ-like events and the sensitivity to physical parameters can be discussed by χ^2 which is expressed in terms of the number of observed neutrinos. We express the number of $e(\mu)$-like events as $N_j^{e\alpha}$ ($N_j^{\mu\alpha}$) where α stands for the flavor of the original flux and j stands for the zenith angle bin index. We denote the numbers of events for anti-neutrinos as $N_j^{\bar{\alpha}\bar{\beta}}$. The zenith angle bin index is determined by the direction of the incident neutrino.

The data is generated with the codes that were used in Ref. [92, 93, 94, 89, 95]. We assume that the data is taken for 2000 days, that the HK fiducial volumes are 0.56 Mton, that the HK detector has the same detection efficiencies as those of SK and that HK atmospheric neutrino data consist of the sub-GeV, multi-GeV and upward going μ events as in the case of SK. The information on the zenith angle bins for the sub-GeV, multi-GeV and upward going μ events are given in Ref. [96] while that on the energy bins is not available. We analyze with the ten zenith angle bins as in Ref. [96]. As the number of events are calculated by our codes, we can use any information on the energy spectrum of the number of events and analyze with any number of the energy bins. Because of the reason discussed in section 5.1, we adopt two energy bins in the contained events and one energy bin in the upward going μ

events.

As mentioned above the octant degeneracy is accompanied by the mass hierarchy degeneracy and the matter effect is important in the mass hierarchy determination. We focus on the multi-GeV events for the zenith angle bin $j = 1$ ($-1.0 < \cos\Theta < -0.8$) which is sensitive to the matter effect where Θ is the zenith angle. Then the number of events are generated as follows:

$$
\begin{aligned}
N_1^{\mu e}(NH) &= 498 \pm 108 \\
N_1^{\bar{\mu}\bar{e}}(NH) &= 66 \pm 15 \\
N_1^{ee}(NH) &= 898 \pm 1 \\
N_1^{\bar{e}\bar{e}}(NH) &= 573 \pm 9 \times 10^{-2} \\
N_1^{e\mu}(NH) &= 11 \pm 3 \\
N_1^{\bar{e}\bar{\mu}}(NH) &= 2 \pm 5 \times 10^{-4} \\
N_1^{\mu\mu}(NH) &= 1970 \pm 130 \\
N_1^{\bar{\mu}\bar{\mu}}(NH) &= 1040 \pm 35
\end{aligned}
$$

$$
\begin{aligned}
N_1^{\mu e}(IH) &= 118 \pm 26 \\
N_1^{\bar{\mu}\bar{e}}(IH) &= 259 \pm 56 \\
N_1^{ee}(IH) &= 1093 \pm 1 \\
N_1^{\bar{e}\bar{e}}(IH) &= 474 \pm 9 \times 10^{-1}\,, \\
N_1^{e\mu}(IH) &= 41 \pm 10 \\
N_1^{\bar{e}\bar{\mu}}(IH) &= 3 \pm 5 \times 10^{-3} \\
N_1^{\mu\mu}(IH) &= 2180 \pm 70 \\
N_1^{\bar{\mu}\bar{\mu}}(IH) &= 950 \pm 65
\end{aligned}
$$

where the uncertainties come from variation of θ_{23} and δ. The atmospheric neutrino experiment measurements are usually the sum of each channel for $e(\mu)$-like events. We can identify the dominant channel of the $e(\mu)$-like events from the number of events listed above. The main contribution for the μ-like event uncertainty comes from the $\nu_\mu \to \nu_\mu$ channel and that for the e-like event uncertainty comes from the $\nu_\mu \to \nu_e$ channel. The number of events are shown in Fig. 6.1.

We can understand the behavior of Fig. 6.1 by looking at the oscillation probability for the dominant channel. The difference between the oscillation probabilities

for two different values of θ_{23} [99] are given by

$$\begin{aligned} & P(\nu_\mu \to \nu_\mu; \theta'_{23}) - P(\nu_\mu \to \nu_\mu; \theta_{23}) \simeq (\sin^2 2\theta'_{23} - \sin^2 2\theta_{23}) \\ \times \quad & \left\{ \cos^2 \tilde{\theta}_{13} \sin^2 \left(\frac{\Lambda_+ L}{2} \right) + \sin^2 \tilde{\theta}_{13} \sin^2 \left(\frac{\Lambda_- L}{2} \right) \right\} \\ - \quad & (\sin^4 \theta'_{23} - \sin^4 \theta_{23}) \sin^2 2\tilde{\theta}_{13} \sin^2 \left(\frac{\Delta \tilde{E}_{31} L}{2} \right) , \end{aligned} \tag{6.1}$$

$$P(\nu_\mu \to \nu_e; \theta'_{23}) - P(\nu_\mu \to \nu_e; \theta_{23}) \simeq (\sin^2 \theta'_{23} - \sin^2 \theta_{23}) \sin^2 \left(\frac{\Delta \tilde{E}_{31} L}{2} \right) , \tag{6.2}$$

where

$$\begin{aligned} \Delta E_{jk} &\equiv \frac{\Delta m^2_{jk}}{2E} \equiv \frac{m^2_j - m^2_k}{2E}, \\ A &\equiv \sqrt{2} G_F N_e, \\ \Delta \tilde{E}_{31} &\equiv \left\{ (\Delta E_{31} \cos 2\theta_{13} - A)^2 + (\Delta E_{31} \sin 2\theta_{13})^2 \right\}^{1/2}, \\ \Lambda_\pm &\equiv \frac{\Delta E_{31} + A \pm \Delta \tilde{E}_{31}}{2}, \\ |\tilde{U}_{\mu 1}|^2 &\simeq \frac{\Delta E_{31} (\Lambda_+ - \Delta E_{31})}{2 \Delta \tilde{E}_{31} \Lambda_-}, \\ |\tilde{U}_{\mu 3}|^2 &\simeq \frac{\Delta E_{31} (\Delta E_{31} - \Lambda_-)}{2 \Delta \tilde{E}_{31} \Lambda_+}, \\ \tan 2\tilde{\theta}_{13} &\equiv \frac{\Delta E_{31} \sin 2\theta_{13}}{\Delta E_{31} \cos 2\theta_{13} - A}, \end{aligned}$$

G_F is the Fermi coupling constant and N_e is the density of electrons. These probabilities are correct to first order in $|\Delta m^2_{21}|/|\Delta m^2_{31}|$ and to all order in θ_{13}. The probabilities for anti-neutrinos is given by changing $A \to -A$. The most significant effect of the different values of θ_{23} can be found near the resonance point where the value of $\tilde{\theta}_{13}$ is close to $\pi/4$. For example, in the case of the normal hierarchy, the $\sin^4 \theta_{23}$ term is dominant in Eq. (6.1) near the resonance point and we found that the $\nu_\mu \to \nu_\mu$ disappearance probability for the 2nd octant is smaller than that for the 1st octant and that the $\nu_\mu \to \nu_e$ appearance probability for the 2nd octant is larger than that for the 1st octant. This behavior is consistent with Fig. 6.1.

The total multi-GeV number of events which are usually measured in the atmospheric neutrino experiments are shown in Fig. 6.2. We found that the number of events for the inverted hierarchy with the 2nd octant and that for the normal hierarchy with the 1st octant are indistinguishable. This is the reason why the octant degeneracy is occur in the atmospheric neutrino experiments.

Fig. 6.3 shows the mass hierarchy sensitivity χ^2 as a function of true δ for the HK experiment. χ^2 for the sensitivity is defined by

$$\chi^2 \equiv \min_{\text{param.}} \sum_j \frac{1}{\sigma_j^2} \left[N_j(\text{WH}) - N_j(\text{TH}) \right]^2 , \tag{6.3}$$

where TH (WH) stands for the true (wrong) mass hierarchy and σ_j is the error for j-th bin data. In Eq. (6.3) it is understood that the systematic errors are introduced by the method of pulls as in the case of the investigation of NSI. In Eq. (6.3) "param." stands for the test variables θ_{23} and δ which we are marginalizing over. The purple band in the figure corresponds to sensitivity in NH and the blue band corresponds to sensitivity in IH. The width of the band is due to the variation of true θ_{23} from 40° to 50° which is the current allowed values of θ_{23}. From the figure we observe that, for conservative value of θ_{23},[1] the mass hierarchy χ^2 is close to 6 around $\delta = 0^\circ$ for both NH and IH and for optimistic value of θ_{23}, the mass hierarchy sensitivity increases to $\chi^2 = 30$ for NH around $\delta \pm 180^\circ$ for NH and $\chi^2 = 18$ for IH around $\delta = +60^\circ$. Here it is interesting to see that the mass hierarchy sensitivity for IH is in general poorer than that for NH. It is also important to note that for $-180^\circ < \delta < -60^\circ$, the width of the IH band is very narrow. The different behaviors of the mass hierarchy sensitivity for NH and IH can be understood by looking at the uncertainties of the number of events come from variation of θ_{23} and δ. The most crucial point is that the uncertainties in the numbers of events for NH are larger than those for IH. If we take $TH = IH$, it is easy to fit the number of events of IH to those of NH by varying θ_{23}. That is why the mass hierarchy sensitivity for $TH = IH$ is poorer than that for $TH = NH$.

[1]The word "conservative (optimistic)" means the value of θ_{23} for which the mass hierarchy sensitivity is minimum (maximum).

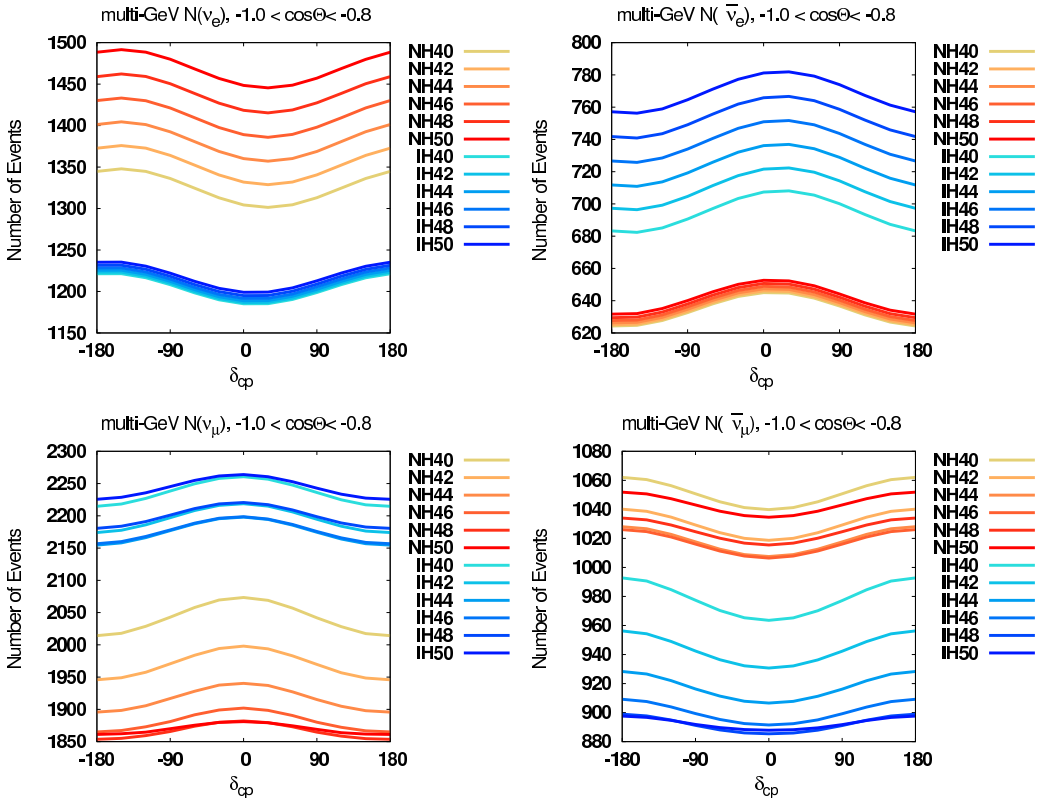

Figure 6.1: The numbers of the multi-GeV neutrino (anti-neutrino) events for the zenith angle $-1 < \cos\Theta < -0.8$ [99].

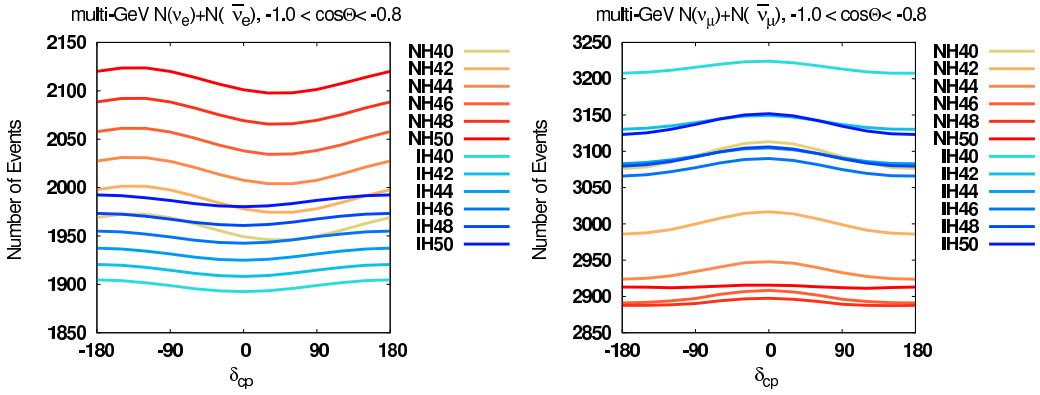

Figure 6.2: The numbers of the multi-GeV e-like (μ-like) events for the zenith angle $-1 < \cos\Theta < -0.8$ [99].

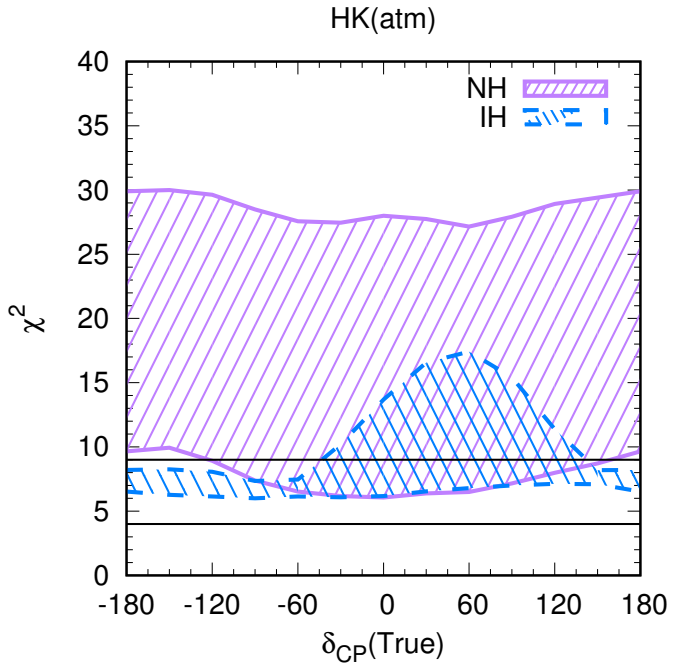

Figure 6.3: The sensitivity of the HK atmospheric neutrino experiment to the mass hierarchy.

Chapter 7

Conclusions

In this thesis, we investigated the sensitivities of the future atmospheric neutrino experiment to neutral current NSI in propagation assuming that the data is taken for 4438 days and that the mass hierarchy is known. At the first stage of investigating NSI, we considered NSI parameterized as $\epsilon_{\alpha\beta}$. In the case with $\epsilon_{\mu\alpha} = 0$ ($\alpha = e, \mu, \tau$) and $\epsilon_{\tau\tau} = |\epsilon_{e\tau}|^2/(1 + \epsilon_{ee})$, from the HK atmospheric neutrino data for 4438 days rate analysis, we obtained the constraint $|\tan\beta| = |\epsilon_{e\tau}|/|1 + \epsilon_{ee}| < 0.3$ at 2.5 σ. In addition to the energy rate analysis, we performed the energy spectrum analysis of the HK data. From the energy spectrum analysis, we obtained the constraint on NSI as $-0.1 \lesssim \epsilon_{ee} \lesssim 0.2$ and $|\epsilon_{e\tau}| < 0.08$ at 2.5σ for the normal hierarchy and $-0.4 \lesssim \epsilon_{ee} \lesssim 1.2$ and $|\epsilon_{e\tau}| < 0.34$ at 2.5σ for the inverted hierarchy. To understand the difference between normal and inverted hierarchy, we investigated the sensitivity of multi-GeV events to ϵ_{ee} in the case of $\epsilon_{e\tau} = 0$ and then we found that the sensitivity of combined $\nu_\mu + \bar{\nu}_\mu$ data is poor even though that of separated $\bar{\nu}_\mu$ data is good only in the case of inverted hierarchy. We interpret this behavior as a destructive phenomenon between neutrinos and antineutrinos for the inverted mass hierarchy. We discussed the potential sensitivity to determine nonzero NSI at HK if the nature is described by nonzero NSI with the ansatz mentioned above. HK will be able to determine NSI parameter precisely for the region $|\epsilon_{ee}| \lesssim 2$ ($-3 \lesssim \epsilon_{ee} \lesssim 1$) in the case of normal (inverted) hierarchy. The difference between normal and inverted hierarchy is due to the destructive phenomenon.

Because we found that the HK has a good sensitivity to NSI, we investigated the possibility to observe nonzero NSI indicated by the tension between solar neutrinos and KamLAND data taking all NSI parameters into account. This is the second stage of investigating NSI. In this stage, we do not assume the parabolic relation between $\epsilon_{\tau\tau}$ and $|\epsilon_{e\tau}|$ for a given ϵ_{ee} so that $\epsilon_{\tau\tau}$ is regarded as an independent parameter.

We obtained the sensitivity of HK to NSI parameterized as $\epsilon_{D,N}$ which are linear combination of $\epsilon_{\alpha\beta}$, because the nonzero NSI indications are given in terms of $\epsilon_{D,N}$. We have taken into account the mapping from the standard parametrization $\epsilon_{\alpha\beta}$ to $\epsilon_{D,N}$ introduced in the solar neutrino analysis. In our analysis, if the nature is not described by NSI, HK will exclude the scenario in which the tension between solar neutrinos and KamLAND data are solved by NSI at 5.0 σ (1.4 σ) for the normal (inverted) hierarchy. We showed that the channel which is most sensitive to NSI is the μ-like multi-GeV high energy bin and the zenith angle bin from below. This is because the matter effect is modified by NSI and the data set which contributes to the sensitivity to the matter effect most is the multi-GeV one.

It is worth noting that the scenario with NSI can be tested by looking at the multi-GeV μ-like events in the future atmospheric neutrino experiments with high precision measurements.

In addition to the investigation of NSI, we investigated the octant degeneracy in HK assuming that the data is taken for 2000 days. We showed the number of ν_e, $\bar{\nu}_e$, ν_μ and $\bar{\nu}_\mu$ multi-GeV events which are regarded as information for theoretical consideration and the numbers of neutrinos and anti-neutrinos combined multi-GeV events which are usually called e-like or μ-like events. The number of events are given for several values of θ_{23} and as a function of CP phase δ. We can understand the behavior of number of events by analytical considerations of oscillation probabilities and found that it is difficult to separate the case of normal hierarchy with 1st octant from that of inverted hierarchy with 2nd octant for both the e-like or μ-like events.

Chapter A

Appendix

A.1 The relation between the standard parametrization $\epsilon_{\alpha\beta}$ and $(\epsilon_D,\ \epsilon_N)$

In this appendix we discuss the relation between the standard NSI parametrization $\epsilon_{\alpha\beta}$ and the parametrization introduced in the investigation of NSI effects in solar neutrinos (ϵ_D^f, ϵ_N^f) in the simplest case, i.e. $\theta_{13}=0$, $\theta_{23}=\pi/4$, $\epsilon_{\alpha\mu}=0$ ($\alpha=e,\mu,\tau$).

We introduce the notation $\epsilon_{\alpha\beta}=3\epsilon^d_{\alpha\beta}$, $\epsilon_D=\epsilon^d_D$ and $\epsilon_N=\epsilon^d_N$. Then Eq. (4.11) becomes

$$3\epsilon_D=-\frac{1}{2}\epsilon_{ee}+\frac{1}{4}\epsilon_{\tau\tau} \tag{A.1}$$

$$3\epsilon_N=-\frac{1}{\sqrt{2}}\,\epsilon_{e\tau}\,. \tag{A.2}$$

The two nonvanishing eigenvalues of the matter potential in the standard NSI parametrization $\lambda_{e'}$, $\lambda_{\tau'}$ in the unit of $\sqrt{2}G_FN_e$ are given by

$$\begin{pmatrix}\lambda_{e'}\\ \lambda_{\tau'}\end{pmatrix}=\frac{1+\epsilon_{ee}+\epsilon_{\tau\tau}}{2}\pm\sqrt{\left(\frac{1+\epsilon_{ee}-\epsilon_{\tau\tau}}{2}\right)^2+|\epsilon_{e\tau}|^2}\,,$$

and it is easy to show the following relations

$$\lambda_{e'}+\lambda_{\tau'}=1+\epsilon_{ee}+\epsilon_{\tau\tau} \tag{A.3}$$

$$\lambda_{e'}\,\lambda_{\tau'}=(1+\epsilon_{ee})\,\epsilon_{\tau\tau}-|\epsilon_{e\tau}|^2. \tag{A.4}$$

Assuming $1+\epsilon_{ee}>0$, $\epsilon_{\tau\tau}>0$, we postulate the following approximate parabolic relation

$$\lambda_{\tau'}=\frac{1+\epsilon_{ee}+\epsilon_{\tau\tau}}{2}-\sqrt{\left(\frac{1+\epsilon_{ee}-\epsilon_{\tau\tau}}{2}\right)^2+|\epsilon_{e\tau}|^2}=\alpha\ (>0)\,. \tag{A.5}$$

In the limit of $\alpha\to 0$, Eq. (4.20) which is the parabolic relation between $\epsilon_{\tau\tau}$ and $|\epsilon_{e\tau}|$ for a given ϵ_{ee} can be obtained. From Eqs. (A.3) and (A.4) we have

$$\begin{aligned}\lambda_{e'}&=1+\epsilon_{ee}+\epsilon_{\tau\tau}-\alpha\\&=\frac{(1+\epsilon_{ee})\,\epsilon_{\tau\tau}-|\epsilon_{e\tau}|^2}{\alpha}=\frac{(1+\epsilon_{ee})\,\epsilon_{\tau\tau}-|3\sqrt{2}\epsilon_N|^2}{\alpha}\,.\end{aligned} \tag{A.6}$$

From Eq. (A.1) we obtain

$$1+\epsilon_{ee}=(1-6\epsilon_D)+\frac{1}{2}\epsilon_{\tau\tau}\,. \tag{A.7}$$

Substituting Eq. (A.7) into Eq. (A.6), we get

$$\begin{aligned}&\frac{1}{\alpha}\left\{\left(1-6\epsilon_D+\frac{1}{2}\epsilon_{\tau\tau}\right)\epsilon_{\tau\tau}-|3\sqrt{2}\epsilon_N|^2\right\}=1-6\epsilon_D+\frac{3}{2}\epsilon_{\tau\tau}-\alpha\,,\\&\to\quad(\epsilon_{\tau\tau}-\alpha)^2+2\left(1-6\epsilon_D-\frac{\alpha}{2}\right)(\epsilon_{\tau\tau}-\alpha)-4|3\epsilon_N|^2=0\end{aligned} \tag{A.8}$$

which yields

$$\begin{aligned}\epsilon_{\tau\tau}-\alpha&=-\left(1-6\epsilon_D-\frac{\alpha}{2}\right)+\left\{\left(1-6\epsilon_D-\frac{\alpha}{2}\right)^2+4|3\epsilon_N|^2\right\}^{1/2}\\1+\epsilon_{ee}-\alpha&=\frac{1}{2}\left(1-6\epsilon_D-\frac{\alpha}{2}\right)+\frac{1}{2}\left\{\left(1-6\epsilon_D-\frac{\alpha}{2}\right)^2+4|3\epsilon_N|^2\right\}^{1/2}\,.\end{aligned}$$

It is easy to see that the last two equations satisfy

$$(1+\epsilon_{ee}-\alpha)\,(\epsilon_{\tau\tau}-\alpha)=2|3\epsilon_N|^2=|\epsilon_{e\tau}|^2\,. \tag{A.9}$$

Eq. (A.9) is equivalent to the characteristic equation of the matter potential and regarded as the generalized parabolic relation in the case of nonvanishing α.

By the way, the parabolic relation (4.20) with vanishing α can be rewritten we note in passing that

$$\epsilon_{\tau\tau}=\tan\beta|\epsilon_{e\tau}|. \tag{A.10}$$

Taking Eq.(A.9) and (A.10) into account, the matter angle with generalized parabolic relation should be defined as

$$\begin{aligned}\tan\beta &= \frac{|\epsilon_{e\tau}|}{1+\epsilon_{ee}-\alpha} \\ &= \frac{\left|3\sqrt{2}\epsilon_N\right|}{1/2-3\epsilon_D-\alpha/4+\left\{(1/2-3\epsilon_D-\alpha/4)^2+|3\epsilon_N|^2\right\}^{1/2}}\,.\end{aligned}$$

Here if we introduce a new angle

$$\tan\beta' \equiv \frac{\tan\beta}{\sqrt{2}}\,,$$

then

$$\begin{aligned}\tan\beta' &= \frac{|3\epsilon_N|}{1/2-3\epsilon_D-\alpha/4+\left\{(1/2-3\epsilon_D-\alpha/4)^2+|3\epsilon_N|^2\right\}^{1/2}} \\ &= \frac{-(1/2-3\epsilon_D-\alpha/4)+\left\{(1/2-3\epsilon_D-\alpha/4)^2+|3\epsilon_N|^2\right\}^{1/2}}{|3\epsilon_N|}\,. \qquad \text{(A.11)}\end{aligned}$$

From Eq. (A.11) we have

$$\begin{aligned}\tan 2\beta' &= \frac{2\tan\beta'}{1-\tan^2\beta'} \\ &= \frac{2\,|3\epsilon_N|\left\{\sqrt{\left(\frac{1}{2}-3\epsilon_D-\frac{\alpha}{4}\right)^2+|3\epsilon_N|^2}-\left(\frac{1}{2}-3\epsilon_D-\frac{\alpha}{4}\right)\right\}}{|3\epsilon_N|^2-\left\{\sqrt{\left(\frac{1}{2}-3\epsilon_D-\frac{\alpha}{4}\right)^2+|3\epsilon_N|^2}-\left(\frac{1}{2}-3\epsilon_D-\frac{\alpha}{4}\right)\right\}^2} \\ &= \frac{|3\epsilon_N|}{\frac{1}{2}-3\epsilon_D-\frac{\alpha}{4}}\,. \qquad \text{(A.12)}\end{aligned}$$

Eq. (A.12) implies that the allowed region of the atmospheric neutrino experiment with the generalized parabolic relation (A.9) is the one surrounded by the $\epsilon_N = 0$ axis and the straight line $|\epsilon_N| = |\tan 2\beta'||1/2 - 3\epsilon_D - \alpha/4|$ with the gradient $|\tan 2\beta'|$ and the x-intercept $\epsilon_D = 1/6 - \alpha/12$. In the limit $\alpha \to 0$, Eq. (A.12) reduces to Eq. (4.23).

Bibliography

[1] L. Wolfenstein, "Neutrino Oscillations in Matter," *Phys. Rev.* **D17** (1978) 2369–2374.

[2] M. M. Guzzo, A. Masiero, and S. T. Petcov, "On the MSW effect with massless neutrinos and no mixing in the vacuum," *Phys. Lett.* **B260** (1991) 154–160.

[3] E. Roulet, "MSW effect with flavor changing neutrino interactions," *Phys. Rev.* **D44** (1991) R935–R938.

[4] Y. Grossman, "Nonstandard neutrino interactions and neutrino oscillation experiments," *Phys. Lett.* **B359** (1995) 141–147, `hep-ph/9507344`.

[5] S. L. Glashow, "Partial Symmetries of Weak Interactions," *Nucl. Phys.* **22** (1961) 579–588.

[6] S. Weinberg, "A Model of Leptons," *Phys. Rev. Lett.* **19** (1967) 1264–1266.

[7] S. P. Mikheev and A. Yu. Smirnov, "Resonance Amplification of Oscillations in Matter and Spectroscopy of Solar Neutrinos," *Sov. J. Nucl. Phys.* **42** (1985) 913–917. [Yad. Fiz.42,1441(1985)].

[8] V. Barger, D. Marfatia, and K. Whisnant, "Breaking eight fold degeneracies in neutrino CP violation, mixing, and mass hierarchy," *Phys. Rev.* **D65** (2002) 073023, `hep-ph/0112119`.

[9] J. Burguet-Castell, M. B. Gavela, J. J. Gomez-Cadenas, P. Hernandez, and O. Mena, "Superbeams plus neutrino factory: The Golden path to leptonic CP violation," *Nucl. Phys.* **B646** (2002) 301–320, `hep-ph/0207080`.

[10] H. Minakata and H. Nunokawa, "Exploring neutrino mixing with low-energy superbeams," *JHEP* **10** (2001) 001, `hep-ph/0108085`.

[11] G. L. Fogli and E. Lisi, "Tests of three flavor mixing in long baseline neutrino oscillation experiments," *Phys. Rev.* **D54** (1996) 3667–3670, hep-ph/9604415.

[12] O. Yasuda, "New plots and parameter degeneracies in neutrino oscillations," *New J. Phys.* **6** (2004) 83, hep-ph/0405005.

[13] H. Minakata, H. Sugiyama, O. Yasuda, K. Inoue, and F. Suekane, "Reactor measurement of theta(13) and its complementarity to long baseline experiments," *Phys. Rev.* **D68** (2003) 033017, hep-ph/0211111. [Erratum: Phys. Rev.D70,059901(2004)].

[14] A. Cervera, A. Donini, M. B. Gavela, J. J. Gomez Cadenas, P. Hernandez, O. Mena, and S. Rigolin, "Golden measurements at a neutrino factory," *Nucl. Phys.* **B579** (2000) 17–55, hep-ph/0002108. [Erratum: Nucl. Phys.B593,731(2001)].

[15] J. N. Bahcall and M. H. Pinsonneault, "What do we (not) know theoretically about solar neutrino fluxes?," *Phys. Rev. Lett.* **92** (2004) 121301, astro-ph/0402114.

[16] J. N. Bahcall and C. Pena-Garay, "Solar models and solar neutrino oscillations," *New J. Phys.* **6** (2004) 63, hep-ph/0404061.

[17] B. T. Cleveland, T. Daily, R. Davis, Jr., J. R. Distel, K. Lande, C. K. Lee, P. S. Wildenhain, and J. Ullman, "Measurement of the solar electron neutrino flux with the Homestake chlorine detector," *Astrophys. J.* **496** (1998) 505–526.

[18] **GALLEX** Collaboration, W. Hampel *et al.*, "GALLEX solar neutrino observations: Results for GALLEX IV," *Phys. Lett.* **B447** (1999) 127–133.

[19] **GNO** Collaboration, M. Altmann *et al.*, "GNO solar neutrino observations: Results for GNO I," *Phys. Lett.* **B490** (2000) 16–26, hep-ex/0006034.

[20] **SAGE** Collaboration, J. N. Abdurashitov *et al.*, "Solar neutrino flux measurements by the Soviet-American Gallium Experiment (SAGE) for half the 22 year solar cycle," *J. Exp. Theor. Phys.* **95** (2002) 181–193, astro-ph/0204245. [Zh. Eksp. Teor. Fiz.122,211(2002)].

[21] **Kamiokande** Collaboration, Y. Fukuda *et al.*, "Solar neutrino data covering solar cycle 22," *Phys. Rev. Lett.* **77** (1996) 1683–1686.

[22] **Super-Kamiokande** Collaboration, K. Abe *et al.*, "Solar Neutrino Measurements in Super-Kamiokande-IV," *Phys. Rev.* **D94** (2016), no. 5, 052010, 1606.07538.

[23] **SNO** Collaboration, B. Aharmim *et al.*, "Combined Analysis of all Three Phases of Solar Neutrino Data from the Sudbury Neutrino Observatory," *Phys. Rev.* **C88** (2013) 025501, 1109.0763.

[24] **SNO** Collaboration, B. Aharmim *et al.*, "Electron energy spectra, fluxes, and day-night asymmetries of B-8 solar neutrinos from measurements with NaCl dissolved in the heavy-water detector at the Sudbury Neutrino Observatory," *Phys. Rev.* **C72** (2005) 055502, nucl-ex/0502021.

[25] G. Bellini *et al.*, "Precision measurement of the 7Be solar neutrino interaction rate in Borexino," *Phys. Rev. Lett.* **107** (2011) 141302, 1104.1816.

[26] M. Honda, T. Kajita, K. Kasahara, and S. Midorikawa, "Improvement of low energy atmospheric neutrino flux calculation using the JAM nuclear interaction model," *Phys. Rev.* **D83** (2011) 123001, 1102.2688.

[27] **Super-Kamiokande** Collaboration, E. Richard *et al.*, "Measurements of the atmospheric neutrino flux by Super-Kamiokande: energy spectra, geomagnetic effects, and solar modulation," *Phys. Rev.* **D94** (2016), no. 5, 052001, 1510.08127.

[28] M. Honda, T. Kajita, K. Kasahara, and S. Midorikawa, "A New calculation of the atmospheric neutrino flux in a 3-dimensional scheme," *Phys. Rev.* **D70** (2004) 043008, astro-ph/0404457.

[29] **Kamiokande-II** Collaboration, K. S. Hirata *et al.*, "Experimental Study of the Atmospheric Neutrino Flux," *Phys. Lett.* **B205** (1988) 416. [,447(1988)].

[30] **Kamiokande-II** Collaboration, K. S. Hirata *et al.*, "Observation of a small atmospheric muon-neutrino / electron-neutrino ratio in Kamiokande," *Phys. Lett.* **B280** (1992) 146–152.

[31] **Kamiokande** Collaboration, Y. Fukuda *et al.*, "Atmospheric muon-neutrino / electron-neutrino ratio in the multiGeV energy range," *Phys. Lett.* **B335** (1994) 237–245.

[32] **Super-Kamiokande** Collaboration, Y. Fukuda *et al.*, "Evidence for oscillation of atmospheric neutrinos," *Phys. Rev. Lett.* **81** (1998) 1562–1567, hep-ex/9807003.

[33] **Super-Kamiokande** Collaboration, R. Wendell, "Atmospheric Neutrino Oscillations at Super-Kamiokande," *PoS* **ICRC2015** (2016) 1062.

[34] K. Abe *et al.*, "Letter of Intent: The Hyper-Kamiokande Experiment — Detector Design and Physics Potential —," 1109.3262.

[35] **Hyper-Kamiokande Working Group** Collaboration, K. Abe *et al.*, "A Long Baseline Neutrino Oscillation Experiment Using J-PARC Neutrino Beam and Hyper-Kamiokande," 2014. 1412.4673.

[36] **K2K** Collaboration, M. H. Ahn *et al.*, "Measurement of Neutrino Oscillation by the K2K Experiment," *Phys. Rev.* **D74** (2006) 072003, hep-ex/0606032.

[37] **T2K** Collaboration, K. Abe *et al.*, "Observation of Electron Neutrino Appearance in a Muon Neutrino Beam," *Phys. Rev. Lett.* **112** (2014) 061802, 1311.4750.

[38] **T2K** Collaboration, K. Abe *et al.*, "Precise Measurement of the Neutrino Mixing Parameter θ_{23} from Muon Neutrino Disappearance in an Off-Axis Beam," *Phys. Rev. Lett.* **112** (2014), no. 18, 181801, 1403.1532.

[39] **T2K** Collaboration, K. Abe *et al.*, "Measurement of Muon Antineutrino Oscillations with an Accelerator-Produced Off-Axis Beam," *Phys. Rev. Lett.* **116** (2016), no. 18, 181801, 1512.02495.

[40] **T2K** Collaboration, K. Abe *et al.*, "Measurements of neutrino oscillation in appearance and disappearance channels by the T2K experiment with 6.6×10^{20} protons on target," *Phys. Rev.* **D91** (2015), no. 7, 072010, 1502.01550.

[41] **MINOS** Collaboration, P. Adamson *et al.*, "Measurement of Neutrino and Antineutrino Oscillations Using Beam and Atmospheric Data in MINOS," *Phys. Rev. Lett.* **110** (2013), no. 25, 251801, 1304.6335.

[42] **NOvA** Collaboration, P. Adamson *et al.*, "First measurement of electron neutrino appearance in NOvA," *Phys. Rev. Lett.* **116** (2016), no. 15, 151806, 1601.05022.

[43] **NOvA** Collaboration, P. Adamson *et al.*, "First measurement of muon-neutrino disappearance in NOvA," *Phys. Rev.* **D93** (2016), no. 5, 051104, 1601.05037.

[44] **Double Chooz** Collaboration, Y. Abe *et al.*, "Indication for the disappearance of reactor electron antineutrinos in the Double Chooz experiment," *Phys. Rev. Lett.* **108** (2012) 131801, 1112.6353.

[45] **Double Chooz** Collaboration, Y. Abe *et al.*, "Reactor electron antineutrino disappearance in the Double Chooz experiment," *Phys. Rev.* **D86** (2012) 052008, 1207.6632.

[46] **CHOOZ** Collaboration, M. Apollonio *et al.*, "Search for neutrino oscillations on a long baseline at the CHOOZ nuclear power station," *Eur. Phys. J.* **C27** (2003) 331–374, hep-ex/0301017.

[47] **Daya Bay** Collaboration, F. P. An *et al.*, "Observation of electron-antineutrino disappearance at Daya Bay," *Phys. Rev. Lett.* **108** (2012) 171803, 1203.1669.

[48] **Daya Bay** Collaboration, F. P. An *et al.*, "New measurement of θ_{13} via neutron capture on hydrogen at Daya Bay," *Phys. Rev.* **D93** (2016), no. 7, 072011, 1603.03549.

[49] **RENO** Collaboration, J. K. Ahn *et al.*, "Observation of Reactor Electron Antineutrino Disappearance in the RENO Experiment," *Phys. Rev. Lett.* **108** (2012) 191802, 1204.0626.

[50] **RENO** Collaboration, J. H. Choi *et al.*, "Observation of Energy and Baseline Dependent Reactor Antineutrino Disappearance in the RENO Experiment," *Phys. Rev. Lett.* **116** (2016), no. 21, 211801, 1511.05849.

[51] **KamLAND** Collaboration, K. Eguchi *et al.*, "First results from KamLAND: Evidence for reactor anti-neutrino disappearance," *Phys. Rev. Lett.* **90** (2003) 021802, hep-ex/0212021.

[52] **KamLAND** Collaboration, S. Abe *et al.*, "Precision Measurement of Neutrino Oscillation Parameters with KamLAND," *Phys. Rev. Lett.* **100** (2008) 221803, 0801.4589.

[53] **KamLAND** Collaboration, A. Gando *et al.*, "Constraints on θ_{13} from A Three-Flavor Oscillation Analysis of Reactor Antineutrinos at KamLAND," *Phys. Rev.* **D83** (2011) 052002, 1009.4771.

[54] Y. Koshio, "Solar and atmospheric neutrino oscillations in Super-Kamiokande, talk given at Neutrino Oscillation Workshop 2016. 5-10th of September, 2016, Otranto (Lecce, Italy)." http://www.ba.infn.it/~now/now2016/assets/now2016_koshio.pdf.

[55] **Super-Kamiokande** Collaboration, S. Fukuda *et al.*, "Determination of solar neutrino oscillation parameters using 1496 days of Super-Kamiokande I data," *Phys. Lett.* **B539** (2002) 179–187, hep-ex/0205075.

[56] **T2K** Collaboration, K. Abe *et al.*, "Measurement of Neutrino Oscillation Parameters from Muon Neutrino Disappearance with an Off-axis Beam," *Phys. Rev. Lett.* **111** (2013), no. 21, 211803, 1308.0465.

[57] M. C. Gonzalez-Garcia, M. Maltoni, and T. Schwetz, "Global Analyses of Neutrino Oscillation Experiments," *Nucl. Phys.* **B908** (2016) 199–217, 1512.06856.

[58] M. C. Gonzalez-Garcia and M. Maltoni, "Determination of matter potential from global analysis of neutrino oscillation data," *JHEP* **09** (2013) 152, 1307.3092.

[59] T. Ohlsson, "Status of non-standard neutrino interactions," *Rept. Prog. Phys.* **76** (2013) 044201, 1209.2710.

[60] O. G. Miranda and H. Nunokawa, "Non standard neutrino interactions: current status and future prospects," *New J. Phys.* **17** (2015), no. 9, 095002, 1505.06254.

[61] M. C. Gonzalez-Garcia, M. M. Guzzo, P. I. Krastev, H. Nunokawa, O. L. G. Peres, V. Pleitez, J. W. F. Valle, and R. Zukanovich Funchal, "Atmospheric neutrino observations and flavor changing interactions," *Phys. Rev. Lett.* **82** (1999) 3202–3205, hep-ph/9809531.

[62] P. Lipari and M. Lusignoli, "On exotic solutions of the atmospheric neutrino problem," *Phys. Rev.* **D60** (1999) 013003, hep-ph/9901350.

[63] N. Fornengo, M. C. Gonzalez-Garcia, and J. W. F. Valle, "On the interpretation of the atmospheric neutrino data in terms of flavor changing neutrino interactions," *JHEP* **07** (2000) 006, hep-ph/9906539.

[64] N. Fornengo, M. Maltoni, R. Tomas, and J. W. F. Valle, "Probing neutrino nonstandard interactions with atmospheric neutrino data," *Phys. Rev.* **D65** (2002) 013010, hep-ph/0108043.

[65] M. C. Gonzalez-Garcia and M. Maltoni, "Atmospheric neutrino oscillations and new physics," *Phys. Rev.* **D70** (2004) 033010, hep-ph/0404085.

[66] Z. Berezhiani and A. Rossi, "Limits on the nonstandard interactions of neutrinos from e+ e- colliders," *Phys. Lett.* **B535** (2002) 207–218, hep-ph/0111137.

[67] S. Davidson, C. Pena-Garay, N. Rius, and A. Santamaria, "Present and future bounds on nonstandard neutrino interactions," *JHEP* **03** (2003) 011, hep-ph/0302093.

[68] A. Friedland, C. Lunardini, and C. Pena-Garay, "Solar neutrinos as probes of neutrino matter interactions," *Phys. Lett.* **B594** (2004) 347, hep-ph/0402266.

[69] O. G. Miranda, M. A. Tortola, and J. W. F. Valle, "Are solar neutrino oscillations robust?," *JHEP* **10** (2006) 008, hep-ph/0406280.

[70] A. Palazzo and J. W. F. Valle, "Confusing non-zero θ_{13} with non-standard interactions in the solar neutrino sector," *Phys. Rev.* **D80** (2009) 091301, 0909.1535.

[71] J. Barranco, O. G. Miranda, C. A. Moura, and J. W. F. Valle, "Constraining non-standard interactions in nu(e) e or anti-nu(e) e scattering," *Phys. Rev.* **D73** (2006) 113001, hep-ph/0512195.

[72] J. Barranco, O. G. Miranda, C. A. Moura, and J. W. F. Valle, "Constraining non-standard neutrino-electron interactions," *Phys. Rev.* **D77** (2008) 093014, 0711.0698.

[73] A. Bolanos, O. G. Miranda, A. Palazzo, M. A. Tortola, and J. W. F. Valle, "Probing non-standard neutrino-electron interactions with solar and reactor neutrinos," *Phys. Rev.* **D79** (2009) 113012, 0812.4417.

[74] F. J. Escrihuela, O. G. Miranda, M. A. Tortola, and J. W. F. Valle, "Constraining nonstandard neutrino-quark interactions with solar, reactor and accelerator data," *Phys. Rev.* **D80** (2009) 105009, 0907.2630. [Erratum: Phys. Rev.D80,129908(2009)].

[75] M. C. Gonzalez-Garcia, M. Maltoni, and J. Salvado, "Testing matter effects in propagation of atmospheric and long-baseline neutrinos," *JHEP* **05** (2011) 075, 1103.4365.

[76] **Super-Kamiokande** Collaboration, G. Mitsuka *et al.*, "Study of Non-Standard Neutrino Interactions with Atmospheric Neutrino Data in Super-Kamiokande I and II," *Phys. Rev.* **D84** (2011) 113008, 1109.1889.

[77] T. Ohlsson, H. Zhang, and S. Zhou, "Effects of nonstandard neutrino interactions at PINGU," *Phys. Rev.* **D88** (2013), no. 1, 013001, 1303.6130.

[78] A. Esmaili and A. Yu. Smirnov, "Probing Non-Standard Interaction of Neutrinos with IceCube and DeepCore," *JHEP* **06** (2013) 026, 1304.1042.

[79] A. Chatterjee, P. Mehta, D. Choudhury, and R. Gandhi, "Testing nonstandard neutrino matter interactions in atmospheric neutrino propagation," *Phys. Rev.* **D93** (2016), no. 9, 093017, 1409.8472.

[80] S. Choubey and T. Ohlsson, "Bounds on Non-Standard Neutrino Interactions Using PINGU," *Phys. Lett.* **B739** (2014) 357–364, 1410.0410.

[81] S. Choubey, A. Ghosh, T. Ohlsson, and D. Tiwari, "Neutrino Physics with Non-Standard Interactions at INO," *JHEP* **12** (2015) 126, 1507.02211.

[82] Y. Farzan, "A model for large non-standard interactions of neutrinos leading to the LMA-Dark solution," *Phys. Lett.* **B748** (2015) 311–315, 1505.06906.

[83] Y. Farzan and I. M. Shoemaker, "Lepton Flavor Violating Non-Standard Interactions via Light Mediators," *JHEP* **07** (2016) 033, 1512.09147.

[84] Y. Farzan and J. Heeck, "Neutrinophilic nonstandard interactions," *Phys. Rev.* **D94** (2016), no. 5, 053010, 1607.07616.

[85] M. Maltoni and A. Yu. Smirnov, "Solar neutrinos and neutrino physics," *Eur. Phys. J.* **A52** (2016), no. 4, 87, 1507.05287.

[86] C. Biggio, M. Blennow, and E. Fernandez-Martinez, "General bounds on non-standard neutrino interactions," *JHEP* **08** (2009) 090, 0907.0097.

[87] A. Friedland, C. Lunardini, and M. Maltoni, "Atmospheric neutrinos as probes of neutrino-matter interactions," *Phys. Rev.* **D70** (2004) 111301, hep-ph/0408264.

[88] A. Friedland and C. Lunardini, "A Test of tau neutrino interactions with atmospheric neutrinos and K2K," *Phys. Rev.* **D72** (2005) 053009, hep-ph/0506143.

[89] S. Fukasawa and O. Yasuda, "Constraints on the Nonstandard Interaction in Propagation from Atmospheric Neutrinos," *Adv. High Energy Phys.* **2015** (2015) 820941, 1503.08056.

[90] H. Oki and O. Yasuda, "Sensitivity of the T2KK experiment to the non-standard interaction in propagation," *Phys. Rev.* **D82** (2010) 073009, 1003.5554.

[91] S.-F. Ge and A. Yu. Smirnov, "Non-standard interactions and the CP phase measurements in neutrino oscillations at low energies," *JHEP* **10** (2016) 138, 1607.08513.

[92] R. Foot, R. R. Volkas, and O. Yasuda, "Comparing and contrasting the $\nu_\mu \to \nu_\tau$ and $\nu_\mu \to \nu_s$ solutions to the atmospheric neutrino problem with Super-Kamiokande data," *Phys. Rev.* **D58** (1998) 013006, hep-ph/9801431.

[93] O. Yasuda, "Three flavor neutrino oscillation analysis of the Super-Kamiokande atmospheric neutrino data," *Phys. Rev.* **D58** (1998) 091301, hep-ph/9804400.

[94] O. Yasuda, "Four neutrino oscillation analysis of the Super-Kamiokande atmospheric neutrino data," hep-ph/0006319.

[95] S. Fukasawa and O. Yasuda, "The possibility to observe the non-standard interaction by the Hyperkamiokande atmospheric neutrino experiment," *Nucl. Phys.* **B914** (2017) 99–116, 1608.05897.

[96] **Super-Kamiokande** Collaboration, K. Abe *et al.*, "Limits on sterile neutrino mixing using atmospheric neutrinos in Super-Kamiokande," *Phys. Rev.* **D91** (2015) 052019, 1410.2008.

[97] **Super-Kamiokande** Collaboration, Y. Ashie *et al.*, "A Measurement of atmospheric neutrino oscillation parameters by SUPER-KAMIOKANDE I," *Phys. Rev.* **D71** (2005) 112005, hep-ex/0501064.

[98] J. Burguet-Castell, M. B. Gavela, J. J. Gomez-Cadenas, P. Hernandez, and O. Mena, "On the Measurement of leptonic CP violation," *Nucl. Phys.* **B608** (2001) 301–318, `hep-ph/0103258`.

[99] S. Fukasawa, M. Ghosh, and O. Yasuda, "Complementarity Between Hyperkamiokande and DUNE in Determining Neutrino Oscillation Parameters," `1607.03758`.